Universidade de Santiago de Compostela
FACULTAD DE FÍSICA
Departamento de Física de Partículas

Charge exchange and knockout reactions induced by Sn isotopes at relativistic energies

Jossitt W. Vargas Cruz

Abril de 2014

USC
UNIVERSIDADE
DE SANTIAGO
DE COMPOSTELA

Universidade de Santiago de Compostela
FACULTAD DE FÍSICA
Departamento de Física de Partículas

Charge exchange and knockout reactions induced by Sn isotopes at relativistic energies

Memoria presentada por:
Jossitt W. Vargas Cruz
como disertación para optar al
Grado de Doctor
en Ciencias Físicas
Abril de 2014

USC
UNIVERSIDADE
DE SANTIAGO
DE COMPOSTELA

UNIVERSIDADE DE SANTIAGO DE COMPOSTELA

José Benlliure, Catedrático de del Departamento de Física de Partículas de la Universidad de Santiago de Compostela

CERTIFICA:
que la memoria titulada **Charge Exchange and knockout reactions induced by Sn isotopes at Relativistic Energies** ha sido realizada bajo su dirección por **Jossitt Williams Vargas Cruz** en el **Departamento de Física de Partículas de esta Universidad**, y constituye el **Trabajo de Tesis** que presenta para optar al **Grado de Doctor en Ciencias Físicas**.

Santiago de Compostela, a 14 de Abril de 2014

Fdo. José Benlluire

USC
UNIVERSIDADE
DE SANTIAGO
DE COMPOSTELA

Contents

Contents **i**

1 Peripheral reactions **3**
1.1 Introduction . . . 3
1.2 Experimental challenges and advantages . . . 3
1.2.1 Inverse kinematic and nuclear reactions mechanisms . . . 4
1.3 Theoretical approach to peripheral reactions . . . 5
1.3.1 Microscopical description . . . 5
1.3.2 Macroscopical descriptions . . . 7
1.4 Physics highlights . . . 10
1.4.1 Total reaction cross sections and nuclear size . . . 10
1.4.2 Knock-out reactions and halo structures . . . 11
1.4.3 Quasi-free scattering: single particle states . . . 13
1.5 Charge exchange reactions . . . 13
1.5.1 Elastic and Inelastic Channels . . . 15
1.5.2 Spin-Isospin transitions:Low Energy Transitions . . . 15
1.5.3 High Energy Transitions . . . 18
1.5.4 Nucleon Resonances . . . 19
1.5.5 Pion Interaction . . . 21

2 Experimental technique **24**
2.1 The acelerator facility and the detection setup . . . 25
2.1.1 The GSI acelerator system . . . 25
2.1.2 Beam monitor: SEETRAM calibration . . . 26
2.1.3 Targets . . . 28

2.2 The Fragment Separator FRS . . . 29
2.3 The Detection equipment . . . 31
2.3.1 One Step Experiment: nuclear reactions using direct beams . . . 32
2.3.2 Two Step Experiment: nuclear reactions using secondary beams . . . 33
2.3.3 The time projection chambers (TPCs) . . . 33
2.3.4 Plastic scintillators and Time of Flight calibration (ToF) . . . 34
2.3.5 The Ionization chambers (MUSIC'S) . . . 34
2.4 Identification of the reaction residues . . . 36
2.4.1 Determination of the Magnetic Rigidity . . . 37
2.4.2 Determination of the reduced momentum . . . 38
2.4.3 Determination of Atomic number Z . . . 39
2.4.4 Mass-over-charge ratio determination Determination of mass resolution . . . 40

3 Physical Observables **44**
3.1 Isotopic identification . . . 44
3.2 Measuring Kinematical Quantities . . . 45
3.3 Recoiling energy of projectile residues . . . 48
3.3.1 Energy transformation at beam frame . . . 49
3.3.2 Energy resolution . . . 50
3.3.3 Unfolding of the experimental response . . . 52
3.4 Angular distributions . . . 56
3.5 Cross Sections . . . 57
3.5.1 Determination of the cross sections . . . 58
3.5.2 Background subtraction . . . 59
3.5.3 Dead Time . . . 60
3.5.4 Secondary Reactions . . . 60
3.5.5 Ionic charge states . . . 60
3.6 Reactions using secondary beams . . . 61

4 Isobaric Charge exchange reactions **64**
4.1 Systematic study of charge-exchange reactions . . . 65
4.2 Recoiling energy distributions of projectile residues . . . 66
4.2.1 Comparison with previous experiments . . . 69
4.2.2 Results of reactions using stable beams . . . 72
4.2.3 Results . . . 75
4.3 Sensitivity to the radial distributions . . . 77
4.4 Excitation of baryon resonances in the nuclear medium . . . 79

4.4.1 Evidences for the excitation of different resonances . . 79
4.4.2 Model Calculations 89
4.4.3 In-medium production of the Δ resonance 92
4.4.4 In-medium production of the Roper resonance 93

5 Proton Removal Channel **100**
5.1 Measurements 100
5.2 Nucleon removal cross sections 104
5.2.1 Model calculations 106
5.2.2 Results and discussion 111
5.3 Energy Distribution 115

Conclusions **117**

A Appendix: List of layers in the experiment **120**

B Deconvolution Method applied to the Energy Distributions **124**

Bibliography **126**

Resumen **132**

USC
UNIVERSIDADE
DE SANTIAGO
DE COMPOSTELA

INTRODUCTION

In this work we propose to make use of peripheral heavy-ion collisions induced by stable and non-stable relativistic projectiles to investigate nuclear and nucleonic excitations in nuclei. We propose to induce these excitations by means of isobaric charge-exchange reactions and nucleon knockout.

Charge-exchange reactions are spin-isospin transitions which can provide information on the isovector component of the nuclear force. These excitations may take place in two different energy regimes. At low energies this quasi-elastic charge exchange lead to nuclear excitations (Fermi, Gamow-Teller, spin-dipole, quadruple, giant resonance etc.) and are understood as a virtual charged meson exchange between projectile and target nucleus. At higher energies the process is explained by the excitation of nucleonic resonances and their subsequent decay emitting real charged mesons escaping from the nuclear medium. In the present work we concentrate in the later case. We propose then to investigate baryon excitations in asymmetric nuclear matter. The peripheral character of these reactions, imposed by the escaping condition for the emitted mesons, could be used to investigate the relative abundance of protons and neutrons at the nuclear periphery.

In this work we also investigate nucleon knockout processes. These reactions have been largely used to investigate the single-particle structure and the radial extension of nuclei far from stability. Moreover, we make use of these reactions to investigate nuclear excitations in proton-removal collisions.

The investigation of these processes was done experimentally, running an experiment at the GSI (Germany) facilities. In this experiment we used stable (^{112}Sn , ^{124}Sn) and unstable (^{110}Sn , ^{120}Sn and ^{122}Sn) tin projectiles accelerated at 1000 MeV. The systematic study of the energy dependece of charge exchange reaction used a beam of ^{112}Sn at different energies : 1000,

700 and 400 AMeV. In addition, we used different targets (C, CH_2, Cu and Pb) to systematically investigate these reactions according to the projectile isospin and energy and target nature. The projectile reaction residues were identified in atomic and mass number using a high-resolution zero-degree magnetic spectrometer, the Fragment Separator (FRS). This spectrometer also allowed us to measure with high accuracy the longitudinal momentum of the projectile residues. From these measurements we could defined two observables to characterize isobar charge-exchange and nucleon knockout reactions, the cross sections of these reaction channels and the energy lost by the projectile residues.

The missing energy spectra measured with the FRS for the projectile residues issued in isobar charge-exchange reactions showed two clear components. These components correspond to the quasi-elastic charge-exchange and the baryon excitation. Moreover, an accurate deconvolution technique developed in the framework of this investigation allowed us to identified several baryonic excitations, the Δ and Roper ($N^*(1440)$) resonances and a third one not yet identified. We could also observe a clear dependence of the cross sections of these reaction channels with the neutron excess in the target and projectile nuclei.

The systematic investigation of proton and neutron knockout reactions showed a clear dependence of the cross sections of these reaction channels with the projectile neutron excess. At large neutron excess proton knockout induces larger excitations and vice versa.

The present work is organised as follows. In chapter one we present the start-of-the-art knowledge on charge exchange and nucleon knockout reactions. Chapter two provides a detailed description of the experiment. In chapter three we describe the observables we use for our investigations. Finally in chapters, four and five we present our results concerning the investigation of isobar charge exchange and nucleon knockout reactions.

CHAPTER 1

Framework of peripheral reactions

1.1 Introduction

In this introductory chapter we review the state-of-the-art use of relativistic radioactive beams for investigating the structure of atomic nuclei far from stability in special the experimental techniques and the reactions that provide a complete idea of the nuclear structure. This reactions, in special the peripheral ones, provide us an important tool to investigate the low nuclear-densities regimen, as well as a single particle properties of stable nuclei is studied using direct reactions. We stress our review on charge-exchange reactions and the knock out reaction as an examples of peripheral reactions and its role in the nuclear framework studies.

1.2 Experimental challenges and advantages

The availability of fast radioactivity beams produced by fragmentation generated a high interest in the investigation of nuclei near to the driplines via scattering experiments. The high beam energies experiments provide us results in short interaction times and small scattering angles. Many experimental advantages namely are the possibility of using relatively thick targets (in the order of g/cm^2 or less) and the focus in the kinematical forward direction that makes full-acceptance measurements feasible with moderately sized detectors. A good discussion of the reaction with fast radioactive beams of neutron-rich nuclei is presented in [1]. It is possible to obtain secondary

beams of unstable nucleus using in-flight techniques. An in-flight technique is one of the techniques of isotopical identification. The advantage of the in-flight techniques is the short separation time, which is essentially determined by the flight time through the separator. The cornerstone of in-flight techniques is the the separation of different fragments produced by the fragmentation mechanism. In the in-flight the separation procedure is based in that the reaction products pass a electromagnetic spectrometer. The produced perticles keep their full kinetic energy from the nuclear reaction. The quality of the separated particle beams, such as kinetic energy or phasespace population are determined by the kinematics of the production process. Other important feature of the in-flight technique it is the possibility of study short half-life isotopes, with the unique limitation given by the time of flight of ions that pass the separator around $\sim 1\mu s$.

1.2.1 Inverse kinematic and nuclear reactions mechanisms

The nuclear reaction mechanism determines the kinematic properties of the reaction products such as average energy, energy spread, and angular distribution. But in the projectile fragmentation where the reaction products simply have a velocity close to that of the projectile, the intrinsic nuclear forces determine the reaction mechanism. The fragmentation of projectile consist in principle in a spallation reaction in inverse kinematics. In this case, a heavy relativistic beam hits a light target. The heavy fragments produced from peripheral collisions generally are exotic and they are lighter than the projectile. In this way, it is possible from the stable projectile produce secondary beams that emerge from the production target with a velocity close to that of the projectile.

This experiment analyzed in this dissertation used the inverse kinematics. In this case the reaction products are emitted forward and can then be analyzed with an in-flight magnetic separator. In our case it is the FRagment Separator (FRS), details about this experimental set up will be described in the chapter 2. The kinematic analysis of momentum in the first part separator stage selects all ions with the same mass-to-charge ratio, for bare fragment ions this is equivalent to a separation in A/Z . The A/Z resolution is sufficient for many experiments where the particles are identified event by event on the basis time-of-flight and position measurement at the dispersive plane of the separator combined with an energy loss measurement in an ionization chamber, scitillator or solid state detector to determine the nuclear charge.

The next chapter we will describe the experimental technique and in the chapter 3 we will explain the measure of the physical observables: the cross section and the energy distributions using the inverse kinematic at relativistic energies.

1.3 Theoretical approach to peripheral reactions

The increment of experimental data on fragmentation extend the knowledge on nuclear properties such as nuclear level densities and nuclear dynamics. Many physical observables allow us to known the intrinsic nuclear properties like the cross section and the momentum energy distribution. In order to understand the fragmentation process in special the nucleon removal it is important to divide this physical description at microscopical and macroscopical level. The inelastic nuclear reactions at relativistic energies occur in two steps that take place at different time scales. The first step is a offhand reaction that may modify the composition of the reaction participants and introduces a certain amount of excitation energy. The distinctive time that occur this reaction step is several times 10^{-23}s.

Several models which describe the first step of the fragmentation process namely the intranuclear-cascade model [2] and the abrasion model [3].

The intranuclear-cascade model is based in a microscopic description. The nuclear reaction is treated as a series of individual nucleon-nucleon interactions. More recent models include Boltzman, Uehleng, Uhlenbeck (BUU) [4] or Vlasov, Uehleng, Uhlenbeck (VUU) [5]. In addition, this model was improved by the incorporation Pauli blocking and self-consisted mean field calculations. In the second reaction step the system it thermalizes with the consecutive deexcitation by evaporation of neutrons, protons and light nuclei as well as by fission and emission of gamma rays. During the whole deexcitation phase there is a competition between these different process.

1.3.1 Microscopical description

At microscopical level Intranuclear Cascade models (INC) use Monte Carlo methods the evolution of the INC models was performed by the work of Metropolis [2] and Bertini. The INC codes calculated the nucleon removal as a series of individual nucleon-nucleon interactions in a classical way with Pauli blocking considerations. In relativistic energy of the projectile allows us to use this picture because the wavelength of the incoming particle is of

the order than the average inter-nucleon distance within the nucleus. Typically, there are two kinds of INC models, depending of the treatment of the nuclear medium: the Bertini-like models, where the nucleus is considered as a Fermi sea of nucleons and the nuclear density is step-like with up to 16 divisions including diffuse boundaries; and Cugnon-like models, where all the nucleons present in the projectile and target are followed during all the reaction process.

Intra-Nuclear Cascade codes: INC

Intranuclear cascade codes described the fragmentation problem at microscopical level. The microscopic calculations concerning the first stage of the reactions, the abrasion, can be performed with the so called intra-nuclear cascade (INC) models. At relativistic energies the nucleon-nucleon sequential interactions may be considered as intra-nuclear cascade interactions rather than interactions in the mean-field. This assumption is used in the INC codes briefly introduced here, which can be considered as transport codes of hadrons within the nucleus.

Typically there are two types of INC codes, depending on the treatment of the nuclear medium: the Bertini-like codes, where the nuclear density is considered continuous; and the Cugnon-like codes where the nucleons are treated individually particles. The nucleon-nucleon interactions are defined from free-NN cross sections. The cascade is initiated by the nucleon of the projectile hitting somewhere on the target sphere (only the radial density dependence is considered). Versions of Liège intranuclear cascade (INC) ([6, 7] and references cited therein) add new features: a) modifications in the diffuse nuclear surface. b) the Pauli blocking is improved c) pion dynamic is improved in special the Δ lifetime.

Glauber model approach

The Glauber model and the transport equation are the popular techniques for studying the nuclear scattering at high energies. The Glauber model [8] in its basic form in the quantum mechanical description using eikonal wave fuctions in order to describe the scattering at high energies. Moreover, in some cases the results can be interpreted in terms of the mechanic of nucleon-like rigid balls in a semiclassical approach.

But it is important to note that the term *Glauber* can be used in a broad context namely used in the probability concepts based on the nucleon's mean free path and forward scattering or when quantum mechanical method based on eikonal wavefunctions are used.

The theoretical study of the nucleon removal reaction is possible using the eikonal theory. In this model, several reaction mechanisms are considered to participate in the two-nucleon removal : the inelastic removal of both nucleons, the elastic removal with one of them; the inelastic removal of the second, and the elastic removal of both nucleons. For more details on the reaction model [9, 10].

1.3.2 Macroscopical descriptions

The macroscopical description, the Abrasion model [3, 11, 12, 13] describes the fragmentation between the target and projectile. If the velocity of the particle beam is higher than the Fermi velocity of the potential well, nucleon-nucleon collision are restricted by the overlapping volume between projectile and target. In the geometrical point of view, it is possible to design the interaction zone where nucleons of projectile and target with the name of *participator*. In addition the non overlapping zones are named *spectator* where part of nucleons of projectile and target keep on moving almost undisturbed with their initial velocities. Using approximate numerical methods it is possible to calculate the overlap zone.In this way, the mass number of the projectile prefragments is determinated by th impact parameter as well its production cross section. The geometrical model suggested in[14] had been justified using Glauber-type calculations [8]. It is possible to distinguish two stage in the fragmentation using a macroscopical model: the abrasion and ablation. In the first stage, the abrasion was described above like a shearing off of volume in the participants in the reaction process, on other hand, the ablation is the energy loss due to excitation resulting from the collisions into evaporated particles.

In the first stage assumption is supported by the so called adiabatic approximation [15, 16]. At high energy of beam particles make that nuclear reactions occurs fast compared to the time scale time of the internal motion of nucleons inside the nucleus. Using beam energies above a few tens of MeV/nucleon it is possible to consider the internal degrees of freedom as *frozen* during the collision, in this way the non-interact part of nucleus is only a spectator. In this approximation, the momentum of recoiling fragment after one-nucleon removal provides a direct measure of the wave function of removed nucleon. In this energy regime, the chance to remove certain nucleon in a peripheral collision is given by the probability to find it at the instant to reaction in the overlap zone. The total number of nucleons removed is proportional to the volume of overlap zone.

Figure 1.1 represents different events occurred in a the one-nucleon removal. This reaction channel could be divided into three interaction types:

thee direct removal or knock out of one nucleon at the end of cascade produced in one target-projectile, the second one the multiple scattering. In this process several nucleon-nucleon interactions occur during the cascade phase and the last one, nucleon are evaporated after the cascade phase.

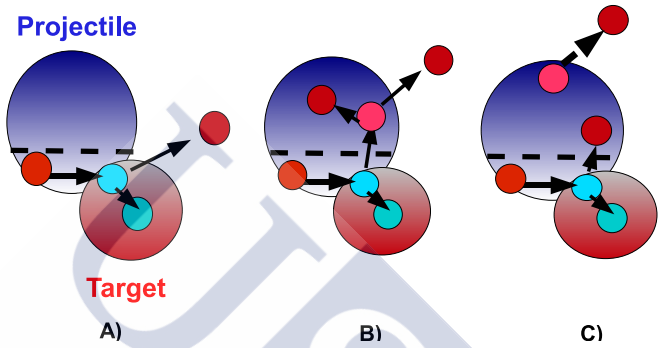

Figure 1.1: *Schematic representation of the different process that contribute to the one-nucleon removal channel. The dashed line indicates the overlap zone, where the participants interact in the reaction and the non-everlapping zone is named spectator .A) knock out B.) Multiple scattering C.) Core excitation with the subsequent nucleon evaporation*

The second stage of the fragmentation process the prefragments may be considered as an ensemble restricted by a few macroscopic variables. This problem is generally treated by numerical statistical-model codes. The evaporation stage is also the final process of the reaction types like multifragmetation.

According to statistical model the characteristic time for the emission of particles varies between $\sim 10^{-16}$s at an excitation energy of 10 MeV and $\sim 10^{-21}$s at 200 MeV. In the geometrical concept of abrasion model, the excitation energy of the prefragment is given by the excess of the surface of the deformed prefragment with respect to a sphere of equal volume. In the framework of statistical-abrasion model it is possible to calculate the excitation energy using the approximation that the nucleons are bound in the potential well of the nucleus. During the abrasion, the orbits of the nucleons not removed are preserved i.e. it is a diabatic approximation [13] . This is based in the short time interval of the abrasion about $\sim 2 - 5 \times 10^{-23}$. By abrasion, a certain number of single particle levels is vacated, and the excitation energy is given by the sum of energies of these holes with respect

to the Fermi surface.

It is clear that in peripheral collisions remove one or several nucleons are removed in the offhand interaction with evaporated residues in the deexitation phase. In this deexitation process the observation of higher heavy products has been attributed to a complex break-up process, the multifragmentation which is expected to occur in more central collisions. in this way, different works [17, 18, 19] stress that might also be explained by sequential fission of the fragment products.

The abrasion-ablation model could show some systematic deviations from the experimental data attributed to an understimated excitation energy of the prefragments but this subject will be discussed in the chapter 5 .

Codes that described peripheral collisions using heavy ions

Models are very useful tools providing valuable information concerning the reaction mechanism or key parameters involved in nuclear reactions.

There exist many codes describing heavy-ion reactions reactions, theoretical models as Glauber or the Eikonal approximation, semi-empirical models as EPAX or the Silberberg-Tsao, the abrasion-ablation models or the intra-nuclear cascades further coupled to evaporation codes. Models were implemented in order to provide information of the reaction mechanism.

Abrasion codes: ABRABLA

ABRABLA [20] is an abrasion code developed to described the fragmentation at relativistic energies. The number of removed nucleons is determined by the volume of the overlapping zone depend of the impact parameter. During the abrasion a certain number of particle levels is vacated (holes) thus the excitation energy of prefragments is calculated by the sum of the energies of all holes with respect Fermi surface.

ABRABLA describes the fragmentation process at relativistic energies. The number of removed nucleons is determined by the volume of the overlapping zone and depends only on the impact parameter. From the number of removed nucleons and their nature (neutrons or protons), the code must determine the initial conditions for the subsequent evaporation stage, that is mass number, neutron excess, excitation energy and angular momentum. The N/Z ratio of the prefragment is calculated according to the hypergeometrical model , where there is no correlation at all between the nucleons during the abrasion, that is, each nucleon has a statistical chance to be neutron or proton.

All of these features are implemented in the code ABRABLA, and a discussion about the results obtained with this code and its comparison with the Sn fragmentation products will be presented in the chapter 5.

-

1.4 Physics highlights

1.4.1 Total reaction cross sections and nuclear size

An important tool is the reaction with antiprotonic atoms [21]. This kind of reaction provide information about the strong-interaction potential and the nucleon density in the region where annihilation takes places. Other methods are sensitive to the charge distribution and usually probe the whole nucleus giving only small contribution of the nuclear periphery , in contrast, the antiprotons are sensitive to the matter density at the nuclear periphery. This effect is noteworthy significant in the nuclear periphery of isotopes with more neutrons. [22]

It is important to note that the complete description of the nuclear densities is a key in the equation of state of nuclear matter Exits some ways of constrain theoretical models using different physical observables as the neutron skin thickness of neutron-rich isotopes. In neutron-rich nucleus the neutron skin is sensitive to the symmetry energy of equation of state [23, 24].

Using charge exchange reaction (explained in the next secion) it is possible to study nucleons in the nuclear periphery. The advantage of the isobaric charge exchange reactions studied in this work is that this technique provides information of the proton and neutron radial distributions in the same experiment by measuring the cross section for the $\Delta-$resonance excitation. The use of Glauber multi-scattering theory [8] the cross section for the isobar (pn) and (np) process will provide a probe sensitive to the neutron and proton radial distributions in nuclei. Several techniques are being used to determine proton and neutron radii. Proton radii can be accurately determined from electron scattering or isotopes shifts in laser spectroscopy [25]. The situation in determining the neutron radii is much worse. Several techniques are based on hadronic probes [26], antiprotonic atoms [27] and antiproton annihilation [28]. Parity-violation electron scattering and collective excitations in the nuclei [29] are also used. However, for most of these techniques, the determination of the neutron radius is model dependent.

In the reference [30] using the isobar model it is possible to calculate the relative probability of each nucleon-nucleon collision to produce an isobar charge-exchange reaction. For an isobaric n-p channel, a nucleon of the

target must collide with a neutron of the projectile surface with Δ resonance excitation. This probability is described in the following way:

$$P_{AA}^{Z+1} \propto \left(\frac{N}{A}\right)_P \left[\left(\frac{Z}{A}\right)_T \sigma_{np}^{ine}(E) \left(\frac{1}{2}\right)_{n-p} + \left(\frac{N}{A}\right)_T \sigma_{nn}^{ine}(E) \left(\frac{5}{12}\right)_{n-n}\right] \quad (1.1)$$

For the p-n case, a nucleon in the target must collide with the proton in the projectile surface. In the similar way that the equation 1.1, the probability of this p-n process is given by:

$$P_{AA}^{N+1} \propto \left(\frac{Z}{A}\right)_P \left[\left(\frac{N}{A}\right)_T \sigma_{pn}^{ine}(E) \left(\frac{1}{2}\right)_{p-n} + \left(\frac{Z}{A}\right)_T \sigma_{pp}^{ine}(E) \left(\frac{5}{12}\right)_{p-p}\right] \quad (1.2)$$

the subindex T and P denotes target and projectile, $\sigma^{ine}(E)$ denotes the inelastic cross section in each nucleon-nucleon reaction as parameterized in [31]

1.4.2 Knock-out reactions and halo structures

Direct reactions are a tool to investigate the nuclear structure. Normally only same nucleons participate in the reaction at this interaction time. Consequently, while a peripheral collision interacts with few nucleons the momentum transfer is not very high. The possible direct reactions could include, for example, a process related to elastic, inelastic, transfer and knockout reactions. In the present dissertation we only explore the removal reactions important at the relativistic energy regime. This reactions are the result of the interaction between the relativistic beam and the target and produce the breakup of projectile into one (or a few) nucleons (neutron or protons). Experiments shows us that it is possible to select a specific reaction channel for example when the produced ejectile have a A-n mass, where n it is a number of removed nucleons , in this case we can observe a nucleon removal example. At this point it is important to remark that in the some papers refer this reaction with different names for instance: nucleon removal, nucleon breakup and nucleon knockout. In this work we use the last term since many publication adopt this one as reference (see for example NSCl publications and references therein [1, 32])

Three different reaction mechanisms are considered to contribute to nucleon removal channel:

1. Knock out of a nucleon removal from the projectile (inelastic breakup). The nucleon-target reaction will result in a relatively large momentum

transfer to the nucleon. As a consequence, the nucleon will be scattered to large angles or even be absorbed by the target and will thus not appear as a projectile-like fragment in the forward direction, with the velocity close to the beam velocity.

2. Nuclear inelastic scattering into the resonant or non resonant continuum.

3. Depending on the target used, differend reaction mechanism are important. For light targets like Be or C, the reaction is dominated by the nuclear interaction, while for heavy targets such as lead the electromagnetic interaction will dominate the process. Electromagnetic dissociation or Coulomb breakup due to the rapidly varying electromagnetic field of a high-Z target experienced by the fast moving projectile.

Important discoveries using knock out reaction like halo nucleus were found. The first results from scattering experiments using light secondary beams of neutrons-rich He and Li isotopes produced by fragmentation of ^{11}B and ^{20}Ne projectiles [33]. By measured total cross section deduced the radii of isotopes. A strong increased of the radii with the neutron excess is observed much much stronger that the expected from the the $A^{\frac{1}{3}}$ dependence tendency known for stable nuclei. For ^{11}B and ^{11}Li shown the huge increase of the radii for some isotopes compared to its neighbors. This effect is explained by a low-density tail of the valence-neutron(s) wave function, called nuclear halo [34].

Not only the valence or halo neutron can be removed in the reaction, but also more deeply bound neutrons might be removed from inner shell i.e. from a core state.

Two proton removal

The direct reaction could generate the two-proton removal of very neutron-rich as a single step direct reaction. Bazin [35] suggested the possibility. That the competing two-step process is the first proton-knockout.

The theoretical study of this reaction is possible using the eikonal theory. In this model, several reaction mechanisms are considered to participate in the two-nucleon removal : the inelastic removal of both nucleons, the elastic removal the one of them and the inelastic removal of the second and the elastic removal of both nucleons. For more details on the reaction model [9, 10].

1.4.3 Quasi-free scattering: single particle states

In the nucleus in atomic nuclei show a shell structure, in this way, direct reactions provide physical obsevables. Our understanding of nuclear structure far from stability relies on experiments with radioactive beams and nuclear reactions in inverse kinematics.

The shell occupancies in ground states wave functions can be revealed by analyzing cross section of direct reactions such as transfer or knock out reactions this at intermediate energies has been shown to be a particular tool to investigate unstable nuclei available with low intensities. But in the case of Quasi-Free Scattering is produced by a high energy beams. This projectile knock a nucleon out of a nucleus without any further significant interaction between the participants of the reaction. The analysis of momentum of the removed particle provide us information about the respective wave function of the removed nucleon.

Others important reactions that allow us to to study the single-particle properties of the nuclear structure are the transfer mechanism. One-nucleon stripping (${}^{A}X(d,p)^{A+1}X$) and pick up reaction (${}^{A}X(p,d)^{A-1}X$) are examples of this process. From the transferred nucleon angular momentum of transferred nucleon from the transferred nucleon it is possible to determine the angular momentum of transferred nucleon, while the final state of the residual nucleus is identified using a magnetic spectrometer. The optimum beam energy to study transfer reactions is defined by the matching condition with the momentum of the valence nucleons, typically around 10-20 MeV/nucleon.

From the partial cross sections the spectroscopic factors are deduced, which provide a measure of overlap of initial-and final-state wave functions in terms of an expansion in the single-particle states observed in the experiment .

1.5 Charge exchange reactions

The fragmentation process can describe reaction products with lighter mass and lower charge than the beam. But in the case of charge exchange reaction the physical mechanism that produce the reaction is totally different. An isobaric charge-exchange reaction is the process for when a projectile with Z protons and N neutrons changes its charge but without altering its atomic mass (A). A typical charge-exchange reaction can be illustrated across reactions (n,p) or (p,n). In the first case, the reaction (n,p), a neutron the projectile interact with the target exchanging its charge turned in a proton.

This process can be represented by following form:

$$A(Z,N) + n \rightarrow B(Z-1, N+1) + p \tag{1.3}$$

where $B(Z-1, N+1)$ is the nucleus producted in the reaction but remains the same atomic mass $A(Z,N)$ of the projectile in the analogous way, for the relation (p,n) it is a possible to find the reaction:

$$A(Z,N) + p \rightarrow B(Z+1, N-1) + n \tag{1.4}$$

In this case, the nucleus producted in the charge exchange reaction, $B(Z+1, N-1)$, has an additional proton, but a neutron less. The charge exchange reaction guards a great similarity with the β decay. Apart from the dynamics of the dispersion, the principal difference between the charge-exchange reactions and the β decay, it is that in the charge exchange reactions the (p,n) and (n,p) channels are not restricted by considerations of the value Q of the reaction to the final conditions (that are lower in energy for the decay β). The reactions (p,n) are related to the decay β^-.

This experimental fact allows us to use the reaction (p,n) to explore information beyond of the limitations imposed by the energetic value Q. Nevertheless, for the case of the decay β^+ difficulties for the shortage of direct beams with neutrons exist.

To produce the charge exchange reactions the experiment used different projectiles like electromagnetic, leptonic and hadronic probes.

The use of light ions such as $(^3He, t)$, $(^6Li, ^6He)$ was the first probes with ions. The use of light and heavy ions have the complication that the projectile and the nucleus in the target can excite in the inelastic channel and this process makes the analysis complicated. With pions and heavy ions it is possible to study the double charge exchange reaction. In such reactions a couple of nucleons changes its charge at the same time. These useful reactions are sensitive to two-body correlations in the nuclei and this information is closely related to obtained using two-nucleon transfer reaction and also is related to double $\beta-$decay.

The charge exchange reaction is an useful tool in the analysis of the nuclear structure. The (n,p) and (p,n) channels are often used to obtain the Gamow-Teller matrix elements which can not be extracted from the $\beta-$decay experiments (see for example [36, 37]). At intermedium and hight energies above of a pion threshold it is possible to excite a $\Delta-$resonance in the inelastic channel. In the isobaric charge exchange reactions the real pion produced in the inelastic energy region must to escape in order to preserve the isobar feature of this reaction. In a meson-exchange picture of the nuclear forces the pion generated at the spin-isospin dependent interaction terms. The pion

plays an important role: the pion has a small mass which can be exchanged over large distances. This fact is important in charge exchange reactions, where the exchange of pions between the projectile and target excites the nuclear spin-isospin degrees of freedom. With the isobaric charge-exchange reactions it is possible to distinguish the number of neutrons and protons in the nuclear periphery, since the production of this reaction at relativistic energies takes place by means of two channels: the quasi-elastic channel and the inelastic channel, the last one with the formation of the resonance Δ. The charge exchange reactions at relativistic energies have been used to determine the isovector spin response of nuclei in the inelastic region. An important energy shift ($\sim$ 70 MeV) is observed by comparison between the $\Delta-$resonance excitation in proton and the same excitation in a nucleus (see [38, 39] and references therein). In this chapter we describe the basic theory and experiments realized previously to study isobaric charge-exchange.

1.5.1 Elastic and Inelastic Channels

At relativistic energy that is involved in this work, the charge exchange reaction not only occurs across the quasi-elastic channel but also across the inelastic channel with the Δ resonance excitation. The quasi-elastic channel corresponds to Gamow-Teller transitions, spin-dipole, spin-quadrupole and other excitations below the production of a pion threshold . The inelastic channel has been observed when the reaction has enough energy to create the Δ, about the average energy of 300 MeV.

The probability of the inelastic channel and the production of Δ isobars and its respective decays is described by the isobaric model [40] and [30]. This channel corresponds to nucleon-nucleon collisions in the nuclear periphery which remains the nucleus cold i.e. without energy excitation. The Δ decay and the pion must escape of the nucleus in order to preserve the atomic mass.

1.5.2 Spin-Isospin transitions:Low Energy Transitions

The charge exchange reactions at low energies have their origin in virtual pion exchange, where the pion changes the charge of the reaction. The diagram 1.2 represents the charge exchange reaction process in the quasielastic energetic region in the reaction $^{112}Sn(Pb,X)^{112}Sb$.

The elemental isovectorial transitions with $\Delta = 1$ generated in the charge exchange reactions at the same time depend on other physical factors like a spin flip ΔS and the angular momentum ΔL. The low energies transitions are summarized in the following:

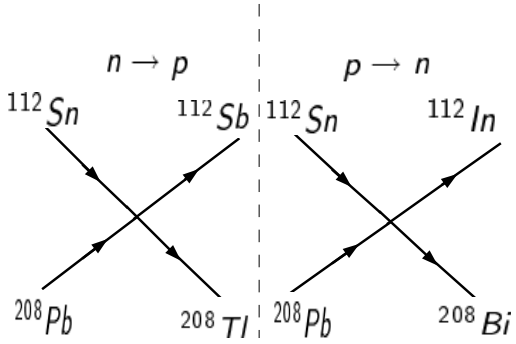

Figure 1.2: *Schematic diagram for the charge exchange reaction in the quasielastic peak for the $n-p$ and $p-n$. This process is mediated by a virtual pion exchange.*

1. Isoscalar Transitions ($\Delta T = 0$): are vibrations in which the neutrons and proton move in phase.

2. Isovectorial Transitions ($\Delta T = 1$):neutrons and proton move in opposite phase.

   - Fermi Transitions: $\Delta T = 1$,$\Delta S = 0$,$\Delta L = 0$
   - Gamow Teller Resonance (GTR): $\Delta T = 1$,$\Delta S = 1$,$\Delta L = 0$, $\sigma\tau$
   - Spin Dipole Resonance (SDR) : $\Delta T = 0, 1$,$\Delta S = 1$,$\Delta L = 1$, $\sigma\tau$
   - Giant Dipole Resonance (GDR) : $\Delta T = 0, 1$,$\Delta S = 0$,$\Delta L = 1$, τ

The probability of each isovector transitions depend on beam energy. Figure 1.3 shows the energy dependence of the spin-isospin transition represented by the $\sigma\tau$ operator and the isospin transition τ. At high energies the τ transitions are significant (above $\sim 800MeV$), at low energies, the $\sigma\tau$ is the dominant contribution.

Furthermore, each isovector transition appears at different energies and angular positions. Figure 1.3 shows the energy distribution of each isovector transition e.g IAS (Isobaric Analog State) or Fermi Transition, GTR and SDR.

Depending on the angular momentum involved in the reaction, each isovector transition has a maximum position in the cross section at different angles (see the figures 1.4 and 1.5). For example in $^{90}Zr(p,n)^{90}Nb$ [42] transitions like IAS and GTR which has a peak in the angular distribution at 0° correspond to $\Delta L = 0$ and the SDR transitions correspond to a peak around $\sim 5°$ with $\Delta L = 1$ and hight momentum transitions $\Delta L > 1$.

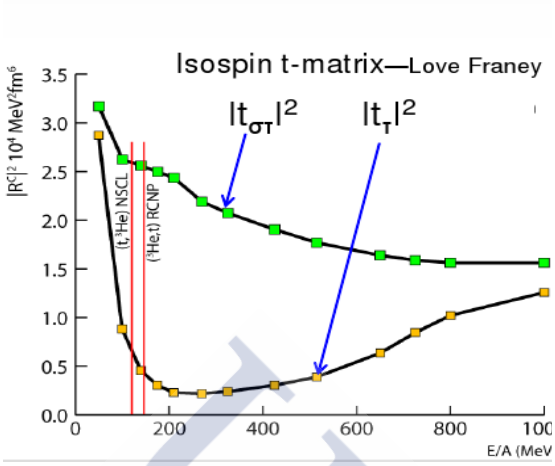

Figure 1.3: *Energy Dependence of each isovector transition calculated in [41]*

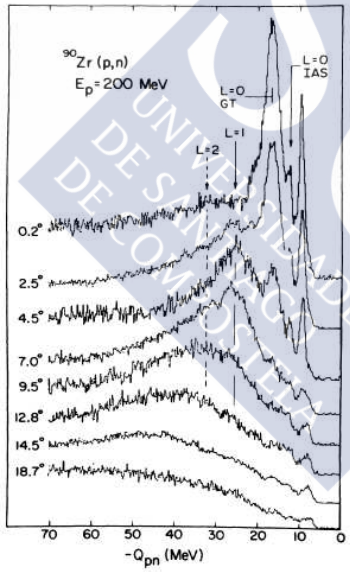

Figure 1.4: *Neutron spectra at E_p=200MeV for $^{90}Zr(p,n)^{90}Nb$ reaction at different scattering angles (from [42]). In this plot it is clear that the angular dependence and the different excitation energy of each isovectorial transition in the quasielastic region.*

Gamow-Teller transitions

The Gamow Teller (GT) resonance is a nuclear collective spin-isospin oscillation in which the nucleons coherently change there spin and isospin direc-

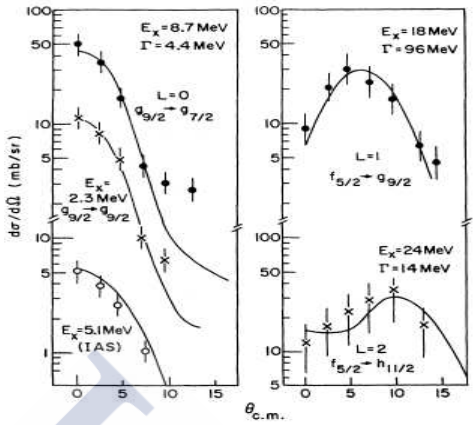

Figure 1.5: *Angular distributions from the* $^{90}Zr(p,n)^{90}Nb$ *reaction for different excitation energy regions. From [42].*

tions without changing their orbital motion. In 80s decade , the spin-isospin correlation was understood after the (p,n) charge-exchange experiment was carried. These experiments demonstrated the existence of collective spin-isospin modes in the nuclei (see [42, 43, 44]). The collective mode was predicted in 1963 by Ikeda, Fuijii and Fujita [45] who predicted the existence of the GT. The β decay has limited access to nuclear states in a small energy window. Therefore, using hadronic probes such as proton, neutrons or light and heavy ions in charge exchange reactions, it is possible to have a complete map out response function in the $\sigma\tau^{\pm}$ channels. The (p,n) reaction is connected to the β decay only if the GT cross section is measured at low momentum transfer $q \sim 0$. This condition is fulfilled only for zero degree scattering and high beam energies. This means that the transfer angular momentum (L) is equal to zero, then the orbital motion of the nucleons is unchanged. The GT resonance is characterized by broad peak with the width of about 4 MeV in all heavy-mass nuclei.

1.5.3 High Energy Transitions

Baryon Resonances

According to the constituent quark model [46], the nucleon is a ground state of the quark triplet , and at relativistic energies it is possible to excite this basic state in baryon resonances, in the figure 1.6 it is a schematic

representation of baryon resonances. This resonants state could be isoscalar transitions with $\Delta = 0$ associate with mesons σ,η or isovectorial transitions with $\Delta = 1$ through π and ρ mesons exchange.

1.5.4 Nucleon Resonances

Nucleon resonances are excited states of nucleon particles with extraordinarily short lifetimes ($\sim 10^{-24}$s). In the quark model picture, the resonances correspond to spin, isospin or spin-isospin states of a nucleon quark system.

The nucleon resonance are represented by symbol as $N(M)$, where M is the particle's approximate mass. When discussing nucleon resonances, sometimes the N is omitted and the order is reversed, giving L_{IJ} where L is the orbital angular momentum of the Nucleon-meson pair produced when it decays, and I and J are the particle's isospin and total angular momentum respectively. For example, a proton can be symbolized as $N(939)S11$ or $S11(939)$.

Δ Resonance

The delta resonance (Δ) is the lower nucleon energetic resonace at 1232 MeV. In a quark picture of baryons it can be viewed as the internal spin-isospin flip excitation of the nucleon. The Δ resonance has an isospin multiplet which has the symbols $\Delta(1232)^{++}$ $\Delta(1232)^{+}$, $\Delta(1232)^{-}$, and $\Delta(1232)^{0}$ and electric charges +2, +1, +0 and −1 elementary charge respectively.

The table 1.1 shows the estimates values of the Δ resonance properties are summarized in the take from Particle Data Group [47].

Breit-Wigner Mass (MeV)	Breit-Wigner full width (MeV)
1231 to 1233 ($\approx$ 1232)	116 to 120 ($\approx$ 118)

Table 1.1: *Breit-Wigner mass and width of the Δ resonant [47].*

The $\frac{3}{2}$ spin means that all the three quarks inside a particle have their spin axis pointing in the same direction, unlike the nearly identical proton and neutron in which the intrinsic spin of one of the three constituent quarks is always opposite the spin of the other two. This spin alignment is complemented by an isospin quantum number of $\frac{3}{2}$ which differentiates the Δ^{+} and Δ^{0} and ordinary nucleons, which have spin and isospin of $\frac{3}{2}$. All varieties of Δ quickly decay via the strong force into a nucleon (proton or neutron) and a pion of appropriate charge.

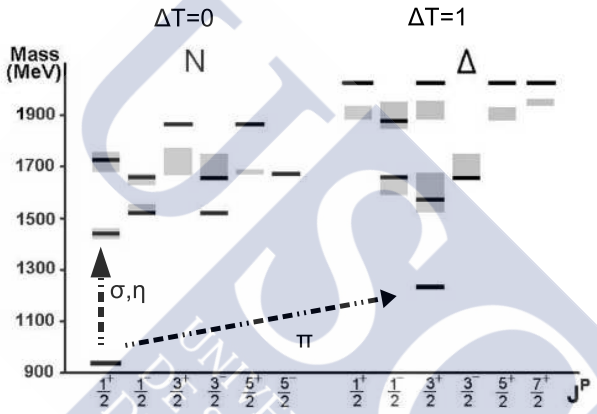

Figure 1.6: *Baryon resonances and its experimental masses from PDG for 4* and 3* resonances. The black lines correspond to calculated values using constituent qaurk model [46] and the green boxes corespond to the experimental masses. Transition with $\Delta T = 0$ require scalar meson (σ, η) and $\Delta T = 1$ require such as π or ρ mesons*

Δ mass shift

The investigation of the Δ-resonance excitation in (p,n) and $(^3He, t)$ charge-exchange reactions has revealed how this process is affected by nuclear in-medium effects. The main observation is a downward energy shift of the Δ-resonance peak position by around 70MeV when using heavy targets($A > 10$) as compared to the mean energy of the Δ resonance produced in free nucleon nucleon collisions.

Further experiments investigating the Δ-resonance excitation in charge-exchange reactions using heavy ion collisions also have shown a clear dependence of the magnitude of the downward energy shift in the Δ resonance with the mass of the target nucleus. In these experiments, performed at the Laboratoire National Saturne in France, the longitudinal-momentum of projectile residues produced in isobar charge-exchange reactions was measured with the spectrometer SPESIV with a typical resolution $\Delta p/p = \pm 7 \times 10^{-4}$.

More recently,it was demonstrated that the magnetic spectrometer FRagment Separator(FRS) [48] at GSI(Darmstadt) can also be used for this purpose. In this case,a ^{208}Pb beam at $1AGeV$ was used to induce isobaric charge-exchange reactions in proton, deuterium, and titanium targets, leading to the production of ^{208}Bi. The recoiling nuclei were isotopically identified with the FRS. The corresponding longitudinal-momentum distributions showed two components that were associated to quasi-elastic and inelastic charge-exchange reaction channels. The quasi-elastic channel peak corresponds to Gamow Teller transitions. The inelastic channel in isobarcharge exchange reactions is understood to be due to the excitation of a Δ resonance in a nucleon nucleon collision, where the subsequently emitted pion escapes from the nuclear medium. Because of the large pion absorption cross-section, these processes correspond most likely to extremely peripheral collisions. Under such conditions, one can expect that the properties of the excited Δ resonance could provide not only information on the in-medium modifications of the hadron masses, but also on the nucleon$-$nucleon cross section at low densities. Moreover, at GSI one can produce beams of nuclei far from stability . Measuring the properties of the excited Δ resonance in isobaric charge-exchange reactions induced via projectiles with a different neutron excess,one could expect to deduce in formation on the isovector component of the nuclear force.

1.5.5 Pion Interaction

Because of the nucleon's spin and isospin structure, the strong interaction has several couplings that allow many different types of nuclear excitations to

be investigated. In a meson-exchange picture of nuclear forces it is the m- and p-meson exchange which generates the spin-isospin- dependent interaction terms. Here the pion plays a special role for the following reasons: (i) Since the pion has a small mass it can be exchanged over large distances. This feature is especially important for the inelastic scattering of nucleons from nuclei and for charge- exchange reactions, where the exchange of neutral or charged pions between the projectile and the target excites the nuclear spin-isospin degrees of freedom at transfers. (ii) Because of its pseudosca-small-momentum lar nature the pion couples longitudinally, to the spin of the nucleon, and thus can give complementary information about nuclear-spin properties to that from the electromagnetic interaction. In particular, the pionic coupling can be used to study the virtual-pion field inside the nucleus. A brief approach to the pion interaction and other models apply to the Δ-resonace dynamic description will be show in the appendix ??.

Roper Resonance

The roper resonance is a nucleon monopole excitation ($L = 0$) excitation. This resonance which appears at about 1440 MeV has never been seen directly in the experimental measure. Its energy and Breit-Wigner fit has large width compared to neighboring resonances, this width is a function with the mass value [49].

In 1963, in a partial-wave analysis performed at Lawrence Livermore National Laboratory, L. D. Roper found a P11 resonance at the [50] . The result was surprizing as there were no hints for such a state and the P11 scattering length is rather large and negative.

Considerable uncertainties are apparent, specially in the full Breit-Wigner width and the branching ratios to the strong-decay channels. Indeed, different values are obtained with different models. The table 1.2 shows the estimates values of the Roper resonance properties are summarized in the take from Particle Data Group [47]

Breit-Wigner Mass (MeV)	Breit-Wigner full width (MeV)
1420 to 1470 ($\approx$ 1440)	200 to 450($\approx$ 300)

Table 1.2: *Breit-Wigner mass and width of the N(1440) (Roper) resonant [47].*

Double Charge exchange reactions

Using pions and heavy ions probes it is possible investigate double-charge exchange reactions. In this reaction a pair of nucleons change their charge states at the same time [51] This reaction is sensitive to two-body correlations in nuclei, that is an important information in nuclear structure study. Moreover, the physical information of the double charge-exchange reaction is closely related with other type of reactions like transfer reactions and double $\beta-$decay

CHAPTER 2

Experimental technique

In this chapter we will present de experimental approach followed to investigate charge exchange and knockout reactions induced by several tin isotopes on different targets. The experiments are based on the use of the inverse kinematics technique.

In the inverse kinematics the reaction products are emitted forward and can then be analyzed with an in-flight magnetic separator. In our case it is the FRagment Separator (FRS). The beam is monitored on the SEcondary Electron TRAnsmssion Monitor SEETRAM and it is focused onto the different targets in each case. The optical features of the Fragment Separator (FRS) and the high quality of detection guarantes the unambigous separation and identification according to mass and charge.

With the inverse kinematics it is possible to obtain secondary beams with exotic nuclei using fragmentations reactions. In the two step configuration, a primary beam inpinging on production target and using magnetic features of the spectrometer separate the secondary beam which later produces reactions in a reaction target at the middle focal plane of FRS.

Using the FRS it is possible to measure with high accuracy the charge and mass quantities of each fragment. In addition, it is possible measure the cross section, the recoiling energy of fragment and the angular distribution of reaction residues.

In the present work, the charge exchange reaction and knockout reactions are produced in the reaction of the different isotopes of Sn at diferent energies (GeV/u) inpigin on difterent targets (2.1 and 2.2) and is studied by measuring their isotopic production cross section and energy distributions.

The experiment was divided in two parts: First, the production of charge exchange reaction yields using stables beams (^{124}Sn and ^{112}Sn) at 1GeV. Secondly, we studied reactions with unstable beams (^{122}Sn, ^{120}Sn and ^{110}Sn), for this reason we used a secondary beam details of this technique which will be described later on. To determine the cross section it is necessary to identify and separate each of products well.

2.1 The acelerator facility and the detection setup

In this section we will provide a general description the experimental facility used in this work, begining with a brief description of the beam acceleration and its monitoring.

The experiment was perfomed in Darmstad, Germany at the facilities of the GSI, since in these facilities it was possible to accelerate heavy-ions at relativistic energies with high intensities (over 10^{7} ions/s). The identification of heavy ions at relativistic energies requires a high resolution detection system.

2.1.1 The GSI acelerator system

The GSI accelerator system was used to produce beams of relativistic energies and hight quality. The acceleration system at the GSI (see Fig 2.1 and ref. [52]) consist in three stages: the ion source, the linear acelerator UNILAC and the heavy ion synchrotron (SIS). In the first stage, the MEVVA ion source produce $^{112,124}Sn$ ions were extracted and preaccelerated.

Then the ions were conducted to the linear accelerator UNILAC. This accelerator has electrodes and magnetic lends.

Using the The second part of UNILAC consists of an accelerating system type Alvarez with fifteen single resonators, it is possible to tune the ionic speed.

The third stage of the acceleration system is the synchrotron accelerating ring [53]. This ring consists of 12 cells each one containg two dipoles, a focus quadrupole and a set of sextupoles in order to correct the chromatic aberrations. This set of cells form the SIS ring with a perimeter of 216 m. The complete set of acceleration system provides very intense beams, necessary for studying the charge exchange and knockout reactions.

For this experiment the beam intensity were about of 10^{8} particles/spill for ^{124}Sn and 7×10^{7} particles/spill for ^{112}Sn Figure 2.1 represent schematic view of the GSI (Darmstad) experimental halls. In this representation it is

possible to observe the three acceleration stages, the ion sources, the UNILAC and SIS and the experimental halls, in particular the FRagment Separator (FRS.)

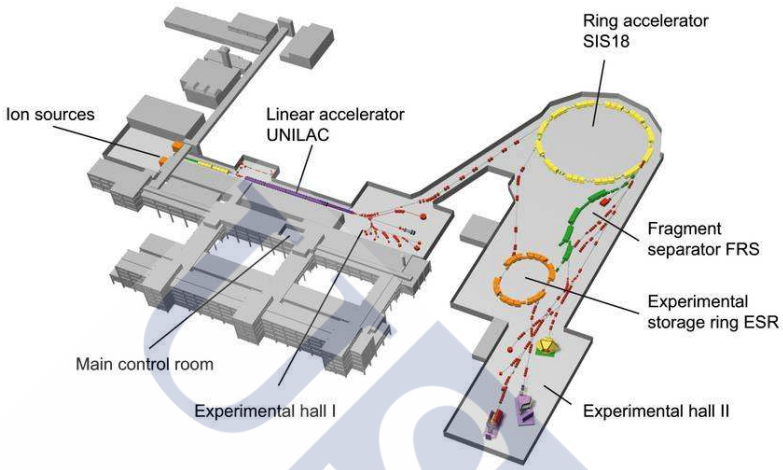

Figure 2.1: *Schematic view of the GSI (Darmstad) experimental halls. In this representation it is possible to observe the three acceleration stages, the ion sources, the UNILAC and SIS and the experimental halls, in particular the FRagment Separator (FRS.)*

2.1.2 Beam monitor: SEETRAM calibration

To measure a cross section it is necessary to monitor the number of particles impinging on target. The monitor used in this work was the SEcondary Electron TRAnsmssion Monitor (SEETRAM) [54]. This monitor consists of three aluminium foils with 10 μm thickness that was arranged in the perpendicular direction of beam propagation. Two of these foils are connected to the a potential difference of + 80 V and the central foild is isolated from the detector and is connected to the ground. When the beam particles pass the central foil, it generates secondary electrons in the surface. These electrons are colected by the influence of the applied voltage. The generated current is transformed in applied voltage. The relation between the input and output signals depends on the sensitivity of the monitor. The analogous output signal is digitized and then recorded in a scaler in its units (SEETRAM units). Figure 2.2 represent a beam profile as a function of time for this experiment measured with the beam monitor SEETRAM. The typical

spill is observed. The background is observed also due to the dark current it must be sustracted in order to obtain the real number of beam projectiles.

This contribution must be sustracted in order to determine the more precise number of projectile.

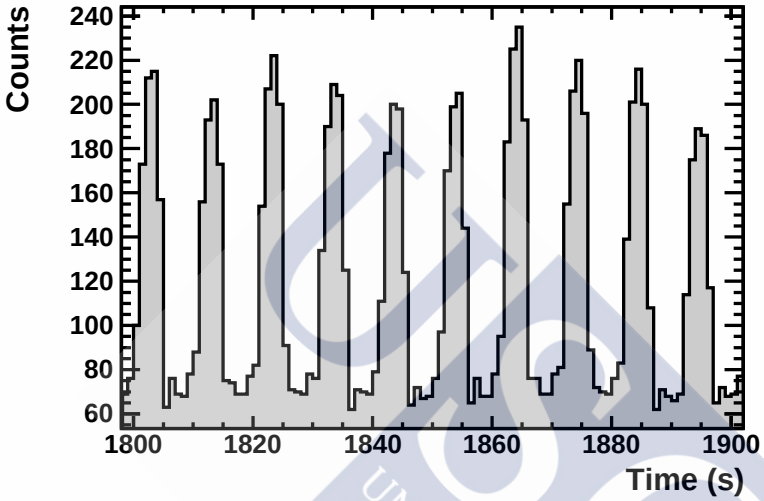

Figure 2.2: *Beam profile as a function of time for this experiment measured with the beam monitor SEETRAM. The typical spill is observed. The background is observed also due to the dark current it must be sustracted in order to obtain the real number of beam projectiles*

To determine the number of impinging beam particles it is necessary to calibrate the seetram units to the number of particles [55]. The calibration was done by comparing the signals of the SEETRAM with the signals of a plastic scitillator. The calibration curve apear in the figure 2.3, where the curve is linear fit in the range of low intensities. The slope calibration factor of this linear fit is of $f = 855.4 \pm 21.4$ particles/SEETRAM. The number of particles N_{beam} is obtained using the following expression:

$$N_{beam} = (N_{Seetram} - N_{background}) \cdot f \cdot 10^{10} \cdot Se \tag{2.1}$$

$N_{Seetram}$ is the number of counts in the SEETRAM units,$N_{background}$ is the background ,f is a SEETRAM calibration factor, Se is the SEETRAM sensitivity that can be changed between $10^{-4} - 10^{-10}$.

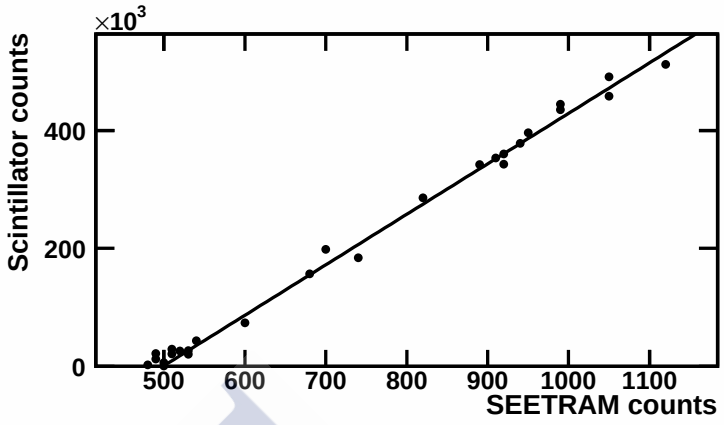

Figure 2.3: *Number of counts obtained by the plastic scintillator as a function of the SEETRAM units in the non saturation zone at low beam intensities. At hight energies this behavior is not linear and in this regime the plastic is in the saturation region.*

2.1.3 Targets

In order to understand the target dependence of the charge exchange and knockout reactions with the target mass, several targets were used in the experiment. Target thickness at S0 are shown in the table 2.1.

Material	Thickness(mg/cm^2)
CH_2(Polyurethane)	95 ± 2
C	167 ± 3
Cu	373 ± 8
Pb	954 ± 19
Pb	255 ± 5

Table 2.1: *Targets and thicknesses used at S0 in the one-step measures.*

On the other hand to obtain the secondary beams, we used a berillium production target located at S0. The thickness of this production target was of $4g/cm^2$. These reaction targets are shown in the table 2.2

For this fact, it was neccesary to do a previous study using simulations with MOCADI code [56]. MOCADI is a Monte Carlo simulation program to calculate transport of primary beams as well as projectile fragment beams through optical systems and layers of matter. Using MOCADI code it is possible to simulate the angular and energy straggling in order to select

Material	Thickness(mg/cm^2)
CH_2(Polyurethane)	1240 ± 25
C	1472 ± 29

Table 2.2: *Targets and thicknesses used at S2. In this case a unstable beam produced at S0 in a Berillyum target of $4g/cm^2$ impinging on these target at S2.*

the value of target thickness to calculate a good compromise between the reaction production of the charge exchange and knockout reactions, with the secondary reactions and principally to perform the resolution in the energy spectrum of the energy because the thickness is related to the straggling .

For more details see the section 3.2. In the case of the direct beams experiment, each target was located at the entry of the spectrometer.

2.2 The Fragment Separator FRS

The FRS is a zero-degree magnetic spectrometer with two symmetrical sections: intermedite plane focal plane is dispersive, being achromatic the complete device. The figure 2.4 shows the focal planes of the spectrometer. Every part consists of two dipoles with its respective quadrupoles and sextupoles. The function of the quadrupoles is to guarantee and to support the optical qualities of the focal planes. The sextupoles are used for corrections of hight optical order. The FRS can operate in diferent modes: achromatic and energy loss energy loss . In this work we use the FRS in its achromatic mode that consist of assuring the position point to point from the entry to the image exit of the spectrometer. The separator has a distance of $72m$ with a maximum magnetic field ($B \sim 1.6T$) and using the curvature readius (around $\rho \sim 11.26$ m) assure a maximum magnetic regidity of $B\rho = 18\ Tm$. The FRS angular acceptance is approximately of 15 mrad and the momentum acceptance is about 3%

The achromaticity is obtained because the dispersion at the final focal plane of FRS $D_{24} = 7.40cm/\%$ compensates the dispersion at middle focal plane of FRS $D_{02} = -7.20cm/\%$ then the magnification is $M_{24} = D_{24}/D_{02} = 1.028$. These values was obtained by measuring the trajectory of ^{124}Sn at 1GeV for different values of magnetic fields in the dipoles of the spectrometer (see Fig 2.5).

The intrinsic resolution of the depends on two parameters: the dispersion and the acceptance. The *acceptance* is the maximum amount in momentum space transmitted through the spectrometer. The acceptance is determinate

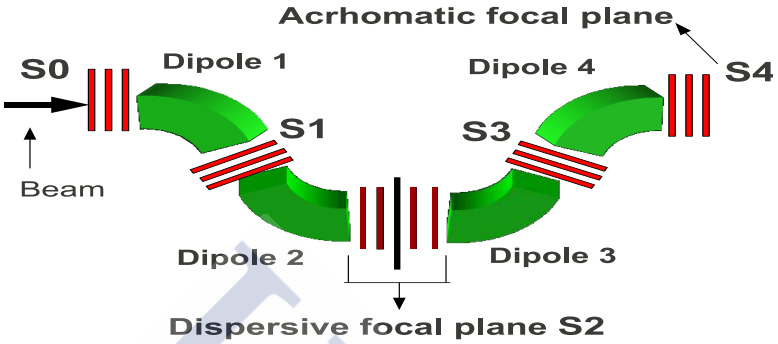

Figure 2.4: *FRS Scheme: Dipoles and quadrupoles are shown. The first part is the entry of the spectrometer named S0 followed by different focal planes S1, S2 , S3 and S4. The intermediate plane S2 receives the name dispersive focal plane and the plane S4 is the final focal image plane or achromatic focal plane.*

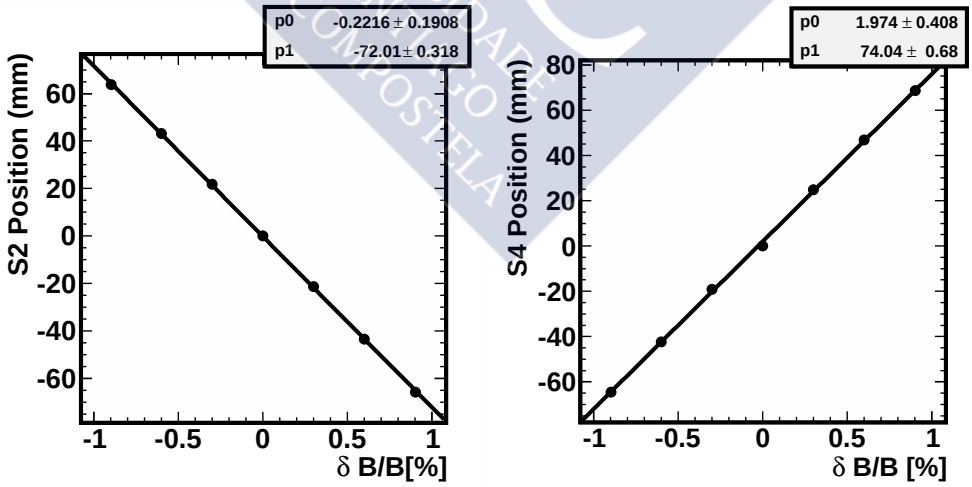

Figure 2.5: *Position onf the ^{124}Sn beam as a function of the variation of the magnetic field ($\delta B/B$) in the dipoles system for the calibration in S2 (left panel) and the final focal plane S4 (right panel)*

by geometrical constraints and the characteristics of the magnetic fields of the different elements of the spectrometer.

The spectrometer resolution depends of its design and the maximum momentum acceptance could be written in the following equation:

$$\left(\frac{\Delta p}{p_c}\right)_{max} = \frac{x_2}{(x|\delta p)_{02}} \tag{2.2}$$

The equation (2.2) shows that the momentum acceptance can be increased x_2 is the transversal position in the focal plane 2 and by reducing the quantity $(x|\delta p)_{02}$ (in Brown notation [57]) named *dispersion*.

The dispersion is the separation in a position when the momentum fragment changes a 1% with respect to the beam, i.e. the dispersion is the transversal distance between the central-trajectory and the trajectory of a particle with momentum difference $\delta p = 1\%$ behind a bending magnet. The dispersion value is expressed in $cm/\%$. A lower dispersion reduces the magnetic rigity resolution necessary for isotopically identification. For this reason, an experiment in spectrometer is a compromise between acceptance and dispersion. Other important factor related to the dispersion is the *Magnification*. It is the variation of a coordinate of the particle, from one image plane to the next one. The magnification depends on the dipoles and quadrupoles system in a spectrometer.

The resolution can be enhanced either by increasing the dispersion or reducing the magnification, which depends on complexity of spectrometer.

2.3 The Detection equipment

In order to make a complete systematic study of very peripheral reactions it is possible to analyze with the FRS the charge exchange and knockout reactions. The focus in this work it is study peripheral reactions in especial the charge exchange reactions and knockout reactions using direct and indirect beams. In the case of the direct beams correspond to stable incident particles and the secondary beams are unstable nuclei projectiles. In the case of the secondary beams were created using a production target located at the entrance of the spectrometer, the selection of this beam was performed using the second part of the spectrometer as will explained in the section 2.3.2.

It is important to analyze the energy and isospin dependence on the target in the quasielastic and inelastic regions.

In this stage we used two direct beams and we named this set-up configuration *one step* experiment.

Moreover it is possible to understand the isospin dependence of the projectile in the charge exchange reactions by using secondary beams in the two step configuration it will be described in the section 2.3.2.

2.3.1 One Step Experiment: nuclear reactions using direct beams

When investigating stable tin isotopes (^{112}Sn ^{124}Sn) it is possible to use beams with hight intensities and different enegies. This features made it possible to reduce the thickness of target mass because in our experiment it is very important to reduce the straggling. This experimental optimization will be discuss in the sections 3.2, 2.1.3 . Beams of ^{124}Sn and ^{112}Sn at 1000 MeV/u, 700 MeV/u and 400 MeV/u beams impinged on different targets and the residues produced were analyzed by using the in-flight technique [58]. The figure B.1 shows the one step configuration. Three plastic scintillators [59]

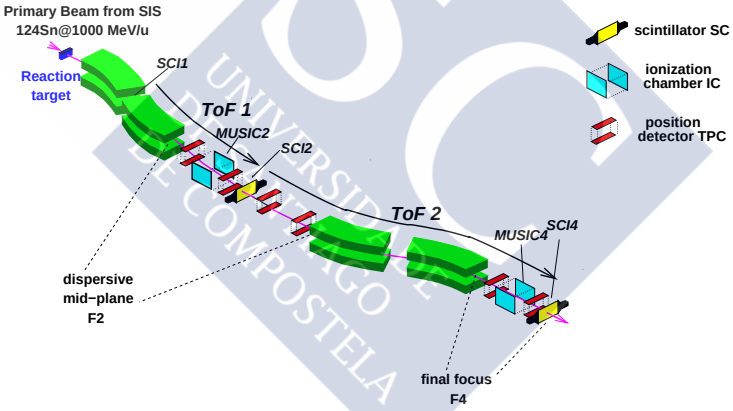

Figure 2.6: *Experimental one step setup: In this configuration it is possible to generate charge exchange reaction in the target at S0 and identify this reactions products in the S2 or S4 focal planes.*

were placed at the S1, the intermediate and the final focal planes. The plastic scintillators provide the information about the time of flight (ToF). In order to track the reaction products to determine the horizontal (x) and vertical (y) position of each fragment, time projections chambers (TPC) were placed at the dispersive focal plane (S2) and the final focal plane (S4) .

The charge of fragments was determinated by measuring the energy loss in two MUltiple-Sampling Ionization Chambers (MUSICs) [60] placed in the dispersive and the final focal plane,respectively.

2.3.2 Two Step Experiment: nuclear reactions using secondary beams

In this part of the experiment it was possible to investigate reactions using unstable beams. A stable beam inpinged at production target located at *S0* and the secondary beam was produced by fragmentation. This secondary beam was identified and separated using the first section of the FRS. We choose the thickness of the reaction target at S2 as a compromise between the production and straggling effects. The intensity of secondary beams is lower than direct beam. For this reason, in order to improve the production we used thicker target. Figure 2.7 shows the two step setup used to study reaction using secondary beams.

The products of this reaction flying in the forward direction were identified using the second section of the FRS.

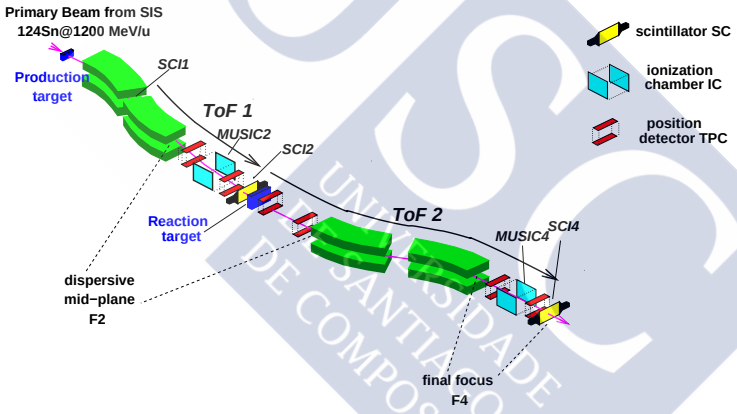

Figure 2.7: *Experimental two step setup: In this experimental configuration is possible study charge exchange reactions using unstable beams. The secondary beam produced at S0 impinging on the reaction target at S2 and in this place the secondary reaction produce the charge exchange reaction products. This reaction products are identified at S4*

2.3.3 The time projection chambers (TPCs)

A Time Projection Chambers (TPCs) are ionization **gas** detectors used with a subdivided anode to measure the horizontal and vertical positions of the particles that traversing these devices [61, 62]. The advantage of this dectector is the low amount of matter in the active volume that reduce the angular and energy straggling in order to preserve the achromatic mode of

the spectrometer. The position resolution obtained by the TPC detectors is about $\sim 200\mu m$.

For this experiment 5 TPC's was placed along the FRS: four of them located in the the intermediate focal plane and two in the final focal plane, as is show in the the figures B.1 and 2.7. This detector is shown 2.8 and it was filled with P10 gas inside of a uniform electrical field applied in the vertical direction. A charged particle that passes throught this detector creates ionization producing electron-ion pairs along the particle track in the gas. The electrons drift toward the anodes by the application of a uniform electrical field.

The drift time provide a measure of the cordinate y and the x axis is obtained by using the delay lines

TPC calibration requests the use of scitillators mask. The mask consist in a grid of scitillators that was placed in front of the TPC. The Direct beam of ^{124}Sn inpigned into the scitillator mask and the beam was defocoused to covered the mask surface. Finally, the coincidence between the scitillator and TPCs form a pattern. This pattern in figure 2.9 shows the calibration which has been matching the grid in channels with their position values $X = 12mm$ and $Y = 12mm$.

2.3.4 Plastic scintillators and Time of Flight calibration (ToF)

To guarantee the high resolution of the FRS it is necessary to fulfill the sufficiently thin detector that preserve the optical quality of the spectrometer, in order not to deteriorate the resolution in the different focal planes.

To reach this requirement an option is to use is necessary to use a set of plastic scintillators, that for this experiment made of (BC420). The thickness of the plastics ones located in S1 and S2 (to see figures B.1 and 2.7) they was 3 mm and the last plastic in S4 was 5 mm. Every plastic covered the whole focal plane and was connected by two parts of pipe photomultipliers HAMAMATSU R2083, which allow a good time resolution if it did not exceed the limit of high intensities ($\leq 10^5 Hz$).

2.3.5 The Ionization chambers (MUSIC'S)

To identify the charge of some nuclei produced we used two MUlti-Sampling Ionization Chambers MUSIC [60]. These chambers are gaseous detectors and their active volume is of 400 mm along the beam direction. The electrical field inside the chamber is generated across the hight voltage

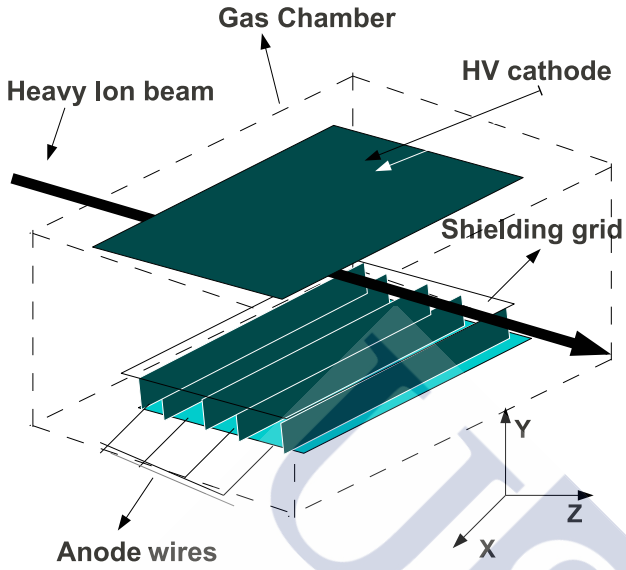

h!

Figure 2.8: *Schematic figure of Time projection Chamber TPC. This tracking detector had two delay lines, each one covering a pair of anodes*

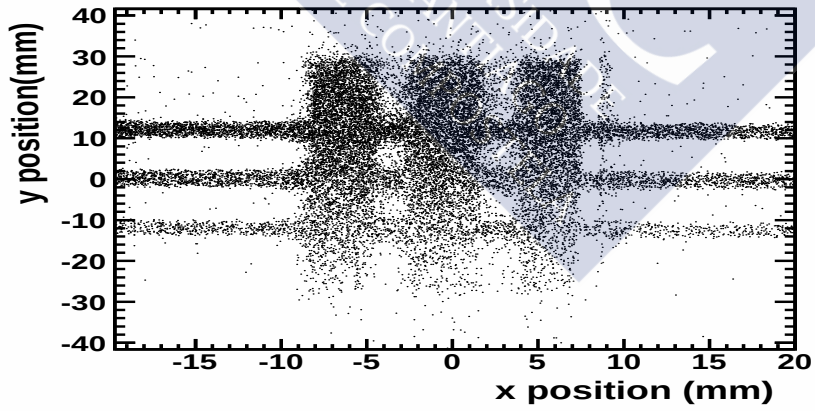

Figure 2.9: *This pattern was obtained using the mask scitillators in coincidence with the TPCs for calibrate the position. The lines correspond tho the position and widths of scitillator fingers.*

applied to the electrodes. Figure 2.3.5 shows a schematic represetation of a MUltiple-Sample Ionization Chamber (MUSIC) were placed at S2 and S4.

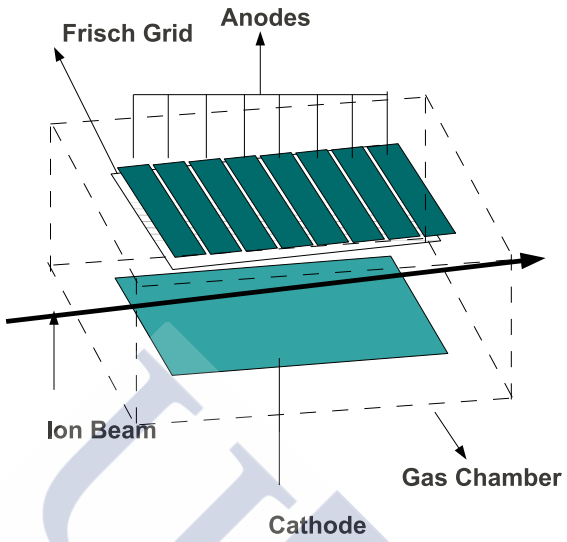

Figure 2.10: *Schematic represetation of a MUltiple-Sample Ionization Chamber (MUSIC). Identical MUSICs with 8 independent anodes were placed at S2 and S4*

When an ion crooses the active area it loses enrgy proportional to square of its charge and inversely proportional to its velocity in agreement to Bethe-Bloch's eaquation. Then produced electrons in the interaction of the ion with the atom gas are collected by the anodes and induce a signal that is amplified and then digitalized by an ADC (Analog-to-Digital Converter). The digitized signal read out by the system of acquisition.

2.4 Identification of the reaction residues

The FRS and its detection devices allows us an unambiguous identify the reaction products due to its high resolution but also to determine with high accuracy its recoiling momentum. The basic principle that use all magnetic spectrometres is the the action of the Lorentz force from a magnetic field on a moving charge particle.

This relation is written in the following equation:

$$F = q\mathbf{v} \times \mathbf{B} = qvB \tag{2.3}$$

where F is the Lorentz force, q charge and $\mathbf{v}$ is the charge and velocity of particle, B is the magnetic field. From the equation 2.3 it is possible calculate the trajectory of a particle in a circular trajectory of radius ρ :

$$\gamma m_0 \frac{v^2}{\rho} = qvB \tag{2.4}$$

where m_0 is the rest mass of the particle, γ is Lorentz's factor, ρ is the radius of curvature of the particle with charge q inside of the magnetic field B. The previous equation can be rewritten in the following way:

$$B\rho = \frac{Au}{Qe}\gamma\beta c \tag{2.5}$$

In this equation $B\rho$ is named magnetic rigidity , u is the atomic mass unit , e is the elementary charge, c is the speed of the light and $\beta = v/c$. Measuring the magnetic rigidity and the velocity it is possible determine A/Z. In addition the measurement of the atomic charge Q will provide the complete identification in mass (A) and atomic number (Z) of the projectile residues, provided they are fully ionized ($Z. - Q$) and thus it is possible to identify the reaction yield.

2.4.1 Determination of the Magnetic Rigidity

Ion optics formalism [63] provides us a relation to determine the magnetic rigidity of a particle traversing a magnetic spectrometer. In general, the position of a charged particle traversing a dipole magnet along the dispersive coordinate can be described according to the following equation:

$$x_f = (x|x_i)_s x_i + (x|x_i')_s x_i' + (x|y_i)_s y_i + (x|y_i')_s y_i' + (x|(\delta B\rho)_i)_s (\delta B\rho)_i \tag{2.6}$$

where the subscript s names the values of the variables of the phase space in the different focal planes of the FRS [1]. The quantities in brackets of the subscript s indicates the coefficients that define the ionic optics of fragment separator for example $(x|x_i)$ is the magnification and $(x|(\delta B\rho)_i)_s$ is the so called dispersion. The other quatities in brackets in the equation 2.6 are variations of the x position with respect to x', y and y' quantities.

In the focal planes which are also called *image planes*, the correlation between the longitudinal position x and the transversal position y and its

[1] $s = 0$ indicates the entry of the FRS, $s = 2$ indicates the intermediate focal plane or dispersive plane and $s = 4$ indicates the final focal plane

angles x' and y' is 0, hereby the equation 2.6 can be written and simplified in the following way:

$$x_f = (x|x_i)_s x_i + (x|y_i)_s y_i + (x|(\delta B\rho)_i)_s (\delta B\rho)_i \tag{2.7}$$

The magnetic rigidity $(B\rho)s$ can be written in terms of its relative variation with respect to the magnetic regidity value $(\delta B\rho)_c$ followed by a particle in a central path along the spectrometer. This relative variation $(\delta B\rho)$ is expressed in the following equation:

$$(\delta B\rho)_s = \frac{(B\rho)_s - (B\rho)_c}{(B\rho)_c} \tag{2.8}$$

In the case of the FRS, it has a symmetry in respect to the focal plane, so horizontal and transverse componets are independent, thus the term of the equation 2.8 $(x|y_i)_s = 0$. So , we can obtain a relation between the magnetic rigidity , the position of the focal plane and the optics of the magnetic system . For example in the case of the intermediate plane or S2 the magnetic rigidity can be written as:

$$(\delta B\rho)_2 = (B\rho)_c \left(1 - \frac{x_2}{D_{02}}\right) \tag{2.9}$$

Here x_2 is the position in the intermediate focal plane and D_{02} is the value of the dispersion from the S0 up to this focal plane in S2. For the focal final plane it is possible to find the following relation for the magnetic rigidity:

$$(\delta B\rho)_4 = (B\rho)_c \left(1 - \frac{x_4 - M_{24}x_2}{D_{24}}\right) \tag{2.10}$$

where x_2 and x_4 are the positions in the focal planes S2 and S4 respectively, D_{24} is the dispersion between both planes: the intermediate and the final focal plane with M_{24} is the magnification. We can determine any nucleus rigidity if we know all parameters of the ionic optics given in the equation 2.10 principally the magnification and the dispersion as well as the magnetic ridity of a particle with central path across the FRS.

The value of the central magnetic rigity $(B\rho)_c$ was measured by a beam reference throught out of FRS , besides with this value and the direct measure of the magnetic field obtained with the Hall probes that have a relative resolution around $\sim 10^{-4}$ in magnetic rigidity. The resolution achieved for the atomic mass is $\Delta A/A = 4.08 \times 10^{-3}$ (FWHM).

2.4.2 Determination of the reduced momentum

In the equation 2.5, the term $\gamma\beta$ is called the *reduced momentum* and it is obtained from the measurement of the time-of-flight (ToF) of the nucleus

traversing the FRS. For this experiment the ToF was determined from the time measurement provided by the plastic scintillators located at the image planes of the FRS as it appears in the figures B.1 and 2.7.

Each plastic scintillator provide two signals of time: a signal for the left side (L) and other one for the right side (R). These signals are filtered and sent to Time to Amplitude Conversor (TAC). The ToF quantity was measured a from the average of the left and right signals as shown the following equation:

$$ToF^{*} = \frac{\alpha_L ToF_L + \alpha_R ToF_R}{2} \tag{2.11}$$

Here α_L and α_R are the TAC calibration factors obtained from a pulse generator of adjustble frequency . The START signal for the time measurement is given by the scintillators at S4 whereas the STOP signal is given by the scitillator at S2 delayed a quantity T_0, this fact is to assure the arrival of the START signal before the STOP one. Then the real value of ToF is obtained in the following way:

$$ToF^{Si} = ToF^{Si}_{STOP} - ToF^{Si}_{START} = T_0 - ToF^{*} \tag{2.12}$$

where superscript Si indicates the ToF measurement in each focal plane e.g. for $i = 2$ note the ToF measure at S2. The delay parameter T_0 was obtained from measurements with the primary beam at different velocities.

This calibration was perfomed using targets with different thickness in order to change the beam velocity in each setting, there- fore to change the time-of-flight. The corresponding velocities of the beam were then calculated calculated using the AMADEUS code [64]. The relationship between the inverse velocity and ToF^{*} is given in the following expression:

$$\frac{1}{v} = \frac{T_0}{l_{Si}} - \frac{ToF^{*}}{l_{Si}} \tag{2.13}$$

Where l_{Si} is the beam path between two measured time points (i.e S1-S2 or S2-S4). T_0 and l_{Si} were determinated using a linear fit like appeared in the figure 2.11 whose coefficients provided the values $T_0 = 89.33ns$ and $l_{S2} = 37.92m$. The typical ToF resolution achieved in the experimental set up was around 170 ps FWHM .

2.4.3 Determination of Atomic number Z

In the section 2.3.5 we explained that the energy loss of the reaction product inside of the MUSIC is proporsional to square of its atomic number

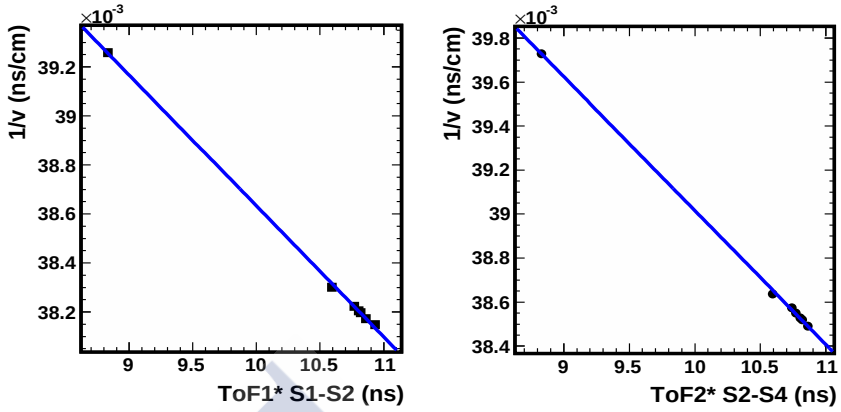

Figure 2.11: *Inverse of velocity as a function of Time of Flight (ToF*) used for calibration. The left pannel correspknds to S1-S2 ToF and the right panel to the S2-S4.*

(Z^2). We can determine the atomic number of the reaction product using the average of the energy loss in each anode by the following way:

$$Z = \alpha + \beta \sqrt{\sum_{j=1}^{N} \frac{\Delta E_j}{N}} \tag{2.14}$$

here N is the number of anodes (in our case N=8), ΔE_j is the amplitud of the signal from each anode. The calibration parameters α and β were obtained using a ^{124}Sn beam at 1GeV (see Fig. 2.12). The resolution achieved for the atomic mass is $\Delta Z/Z = 3.35 \times 10^{-3}$ (FWHM).

Figure 2.12 shows the energy-loss peaks for a magnetic setting centered in ^{124}Sn. The average energy loss ΔE and its correspond Z values are shown.

2.4.4 Mass-over-charge ratio determination Determination of mass resolution

Many factors can affect the correct identification of each isotope and it is important to correct this effects in order to improve the identification. One of this effects is the mass-over-charge dependence on the horizontal angle θ due to the path length of the residues which is not the same because each isotope does not have the trajectory inside of FRS. Using the calculation of the angle defined in the equation 3.10 we can correct the mass over charge ratio dependence on angle. (see the figure 2.13).

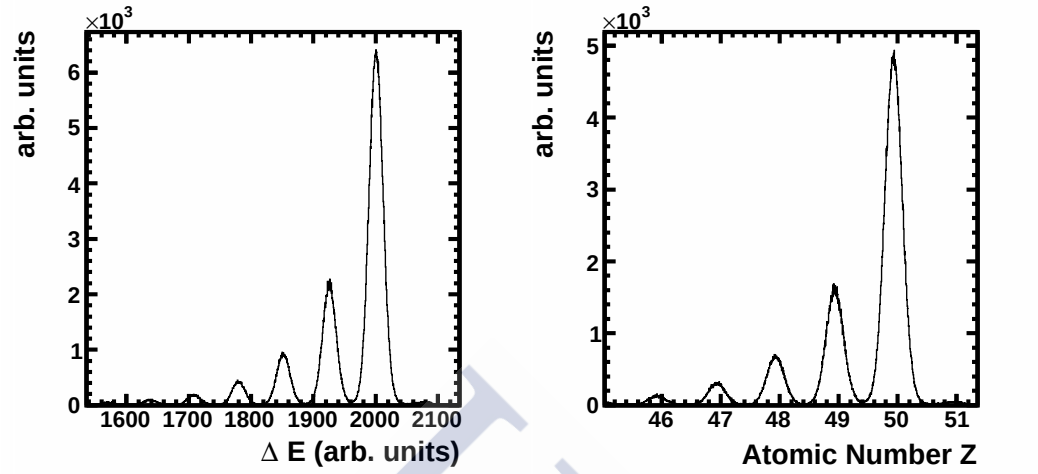

Figure 2.12: *Charge identification of the peaks signals from the MUSICs Left panel: Average energy loss in the MUSICs detectors for a setting centered on* ^{124}Sn*. Right panel reperesent the spectrum of MUSIC for a magnetic setting centered in* ^{124}Sn*.*

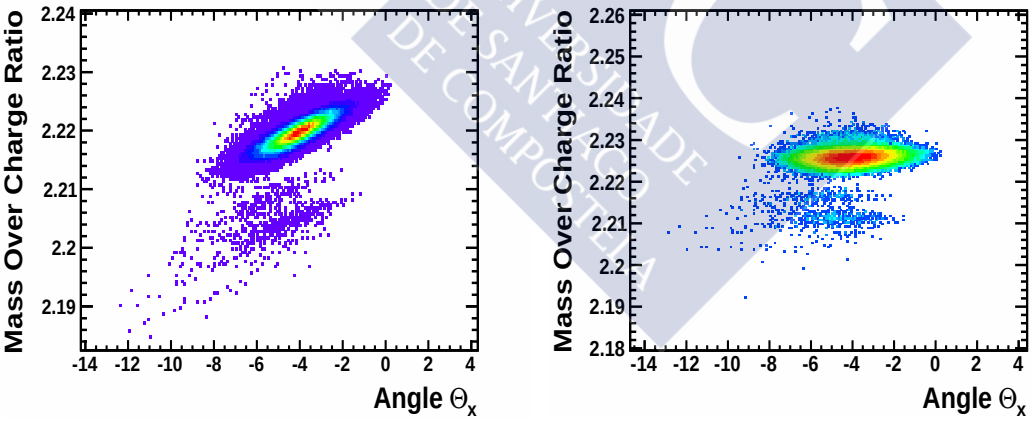

Figure 2.13: *Mass-over-charge (AoQ) correction with respect to angle* θ*. The left represent the AoQ ratio as a function of the angle* θ_x *of the trajectories at the final focal plane for some isotopes transmitted in a setting centered on* ^{112}Sn

Using the equation 2.5 it is possible to determine the mass-over-charge ratio (A/Z) of each transmitted nuclei by combining two independent measure-

ments: the magnetic rigidity ($B\rho$), determined from the position measurements of the TPC detectors, and the velocity, obtained from the measured time-of-flight (ToF).

Figure 2.14 shows the resolution achieved for the mass-over-charge ratio for the Indium isotopes 3.06×10^{-3} (FWHM). With this resolution in A/Z and atomic number (Z) achieved in these measurements are very good, allowing us to unambiguously separate all fragments produced and transmitted along the magnetic spectrometer as appear in the identification matrix (see for example 2.15).

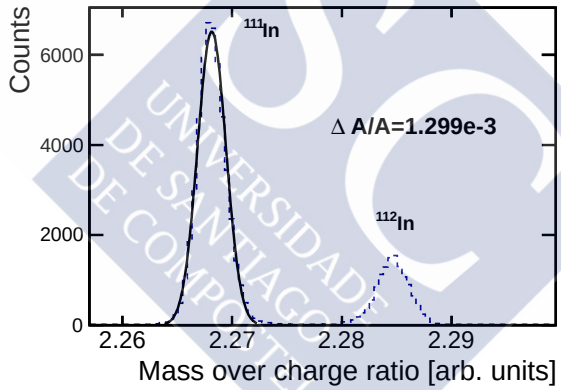

Figure 2.14: *Distribution of mass-over-charge ratio of the Indium fragments in a setting centered in ^{112}In setting centered in ^{112}In.*

The calculated A/Q, together with the atomic number (Z) obtained from the energy loss detectors (MUSIC chambers), can be used to produce an identification cluster plot like the one shown in Figure 2.15, where each nucleus is represented by a spot.

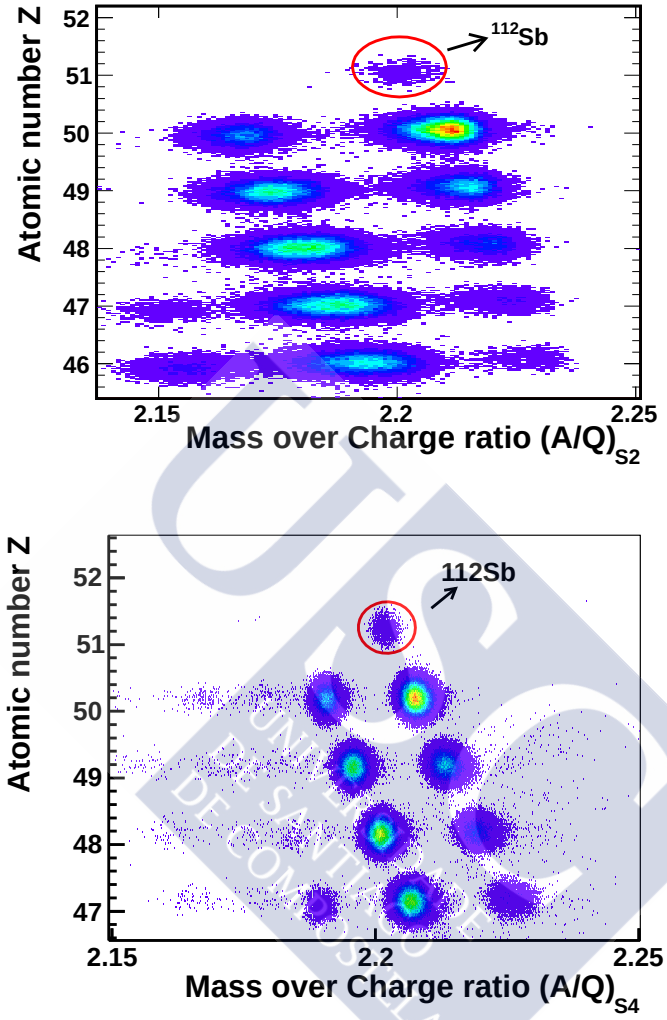

Figure 2.15: *Identification plots (atomic number Z as a function of mass-over-charge ratio): the upper figure is a identification plot at dispersive focal plane (S2) of the reaction products in the reaction at 1GeV of* $^{112}Sn(C,X)^{112}Sb$. *The following plot is the identification plot at the final focal plane S4 of the reaction product in the reaction at 1GeV of* $^{112}Sn(C,X)^{112}Sb$.

CHAPTER 3

Physical Observables

In this chapter we propose to investigate isobar charge exchange and proton knock out reactions, based on the unambiguous identification in mass and charge of the projectile and residues produced in the reaction but also in the accurate determination of its recoiling momentum.

The aim of this chapter is to describe the measurement procedure of the of physical observables: the longitudinal momentum, angular distributions and the cross section.

The calculation of the longitudinal momentum and angular distributions require a high accuracy measure of the position using the TPC detectors and the magnetic Hall probes of high precision. Many factors affect the resolution of the logitudinal momentum and angular distributions and for this reason this topic will be discuss in the section 3.2. The sections 3.3 and 3.4 describe the procedure in order to obtain the energy and angular distributions . Section 3.5 will be dedicated to the evaluation of cross-sections in the one step and two step cases. The cross section allows us investigate the neutron and proton content in the projectile, and by using the energy distribution it will be possible to analyze the interaction probability of charge exchange reactions or knock out reactions.

3.1 Isotopic identification

In the previous chapter we explained in detail the isotopic identification process of the residues produced in a nuclear reaction. As was explained

in the previous chapter our experimental approach is based in the complete identification of the projectile reaction residues. This isotopic identification is the base to obtain the physical observables: cross sections of the projectiles residues and their energy recoil distributions.

According to equation 2.5, the mass-over-charge ratio (A/Q) of a particle that traversing the FRS can be determined from their magnetic rigidity and the velocity. The magnetic rigidity can be determined from the positions of the fragments at the intermediate and final focal planes, respectively. The velocity in both stages was obtained from the time of flight ToF measurements.

Using the A/Q and the atomic number (Z) values obtained from the MUSIC chambers, it is possible to produce an identification plot (atomic number Z as a function of mass-over-charge ratio) like the one shown in Figure 2.15. The resolution in A/Q and atomic number achieved in these measurements are excellent and allow us to unambiguously separate all fragments produced and transmitted along the FRS. Nevertheless, the identification in the final focal plane of the spectrometer (S4) is better than the one obtained at dispersive focal plane because the velocity resolution is increased by the increament of the flight path length of each particles.

Using the two parts of the FRS spectrometer it is possible to identify the particles in the intermediate and final focal planes. With the two stages configuration of this spectrometer allow us to carry out reaction using stable or unstable beams, in the first case the reaction was produced in entrance of the FRS (at S0) (see section 2.3.1) and in the second case the reaction using a secondary beam was achieved using the focal plane (at S2) (section 2.3.2).

3.2 Longitudinal-momentum of the recoiling projectile -like residues

The momentum (energy) recoil distributions is an essential physical observable that characterize the reaction process. The accurate determination of the longitudinal momentum of the nuclei traversing a zero-degree magnetic spectrometer such as the FRS depends on the measurement of the corresponding magnetic rigidities.

If one considers incident particles with the same magnetic rigidity, the same expression (2.2) will provide us the accuracy in the magnetic rigidity determination according to the dispersion of the magnetic spectrometer and the accuracy in the measurement of the positions of the trajectories at the intermediate and final image planes.

The accuracy in the measurement of the positions can be affected by the resolution of the tracking detectors, the initial emittance of the beam, the energy, angular, and reaction location straggling of the transmitted particles in the different layers of matter traversed by the reaction residues.

Figure 3.1 represents the estimated contributions to the final resolution in the measurement of the magnetic rigidity due to the resolution of the tracking detectors, the beam emittance, and the electromagnetic interactions of the nuclei with an aluminum target as a function of its thickness. In these calculations, we have taken as reference the nominal values of the dispersion and magnification of the Fragment Separator ($(x|\delta p)_{24} = 7.40\ cm/\%$ and $(x|x)_{24} = -7.20\ cm/\%$

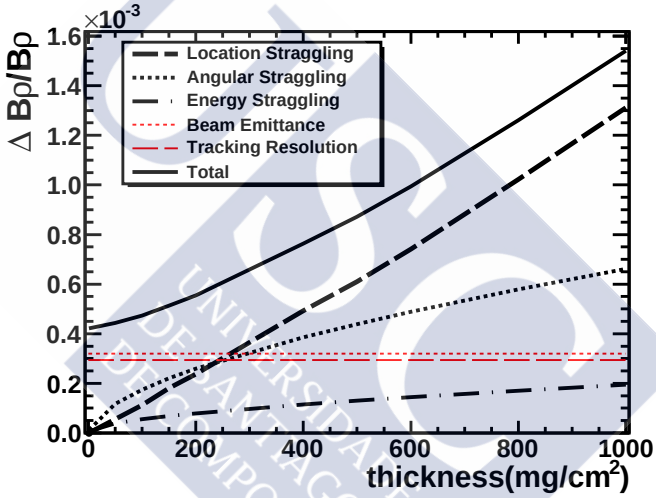

Figure 3.1: *Different contributions to the resolution in magnetic rigidity measurements with a magnetic spectrometer as a function of the target thickness. The thin horizontal lines represent the energy spread of the beam (dotted line) and the effect due the position resolution of the tracking detector (dashed line). The thick lines represent the effect due to the electromagnetic interactions of the projectile and residual nuclei with the target: energy straggling (dashed-dotted) line, angular straggling (dotted line), the reaction location straggling (dashed line). The thick solid line represents the final resolution considering all the contributions.*

In the figure 3.1 , the thin horizontal lines represent the contribution to the resolution due to the beam energy dispersion $\Delta E/E = \pm 5 \times 10^{-4}$ (dotted line) and the tracking detector resolution considering $\Delta x_2 = \Delta x_4 = 0.2$ mm (dashed line). The thick lines evolving with the target thickness represent the contribution to the magnetic rigidity resolution due to the electromagnetic interactions of the incoming nuclei with the target material, the energy

straggling (dashed-dotted line), the angular straggling (dotted line) and the reaction location straggling (dashed line). The solid line represents the final resolution considering all the above mentioned effects.

As can be seen in the figure, the position resolution of the tracking detectors and the beam emittance limit the magnetic rigidity resolution for aluminum targets thinner than 250 mg/cm^2. For thicker targets, the resolution is limited by the electromagnetic interactions of the transmitted nuclei with the target material.

Unfortunately, the target thickness is very often determined by statistical considerations. In the particular case of measurements with secondary beams of nuclei far from stability having low intensities the feasibility of the measurements requires the use of thick targets. In those cases, the possibility of unfolding contribution of those effects degrading the magnetic rigidity resolution could be an option for accurate measurements. Moreover, the measurement of the momentum dispersion of non-interacting beam nuclei provide an optimal definition of the experimental response function required by the unfolding procedure. Indeed, beam nuclei experience electromagnetic interactions in the target and the layers of matters that are placed along the spectrometer.

In the our case, we choose the targets (see 2.1.3) in order to minimize the straggling effects and in this way improve the energy distributions.

In the case of reactions at S0 allow us to select thiner targets than S2 reactions because the high intensity of a direct beams assured a high production of nuclear residues. On other hand, in the case of the S2 reactions the secondary beam have a relative low intensity, for this reason we increse the thickness of reaction target at S2 in order to increse the production reaction products but this procedure implies that the resolution of the momentum distribution decreases as consecuence of the straggling effects.

Longitudinal and Parallel Momentum distributions

The longitudinal momentum of a particle is one of the physical observables and this quantity preserve the physical information about the interaction at microscopical level.

The longitudinal momentum can be obtained from the equation 2.4 and this expression that can be rewritten in the following way:

.

$$p = \gamma m_0 v = qB\rho \tag{3.1}$$

The relation between the parallel ($p_{\parallel}$) and the transversal ($p_{\perp}$) momentum can be expressed by the following equation:

$$tan\theta = \frac{p_\perp}{p_\parallel} \tag{3.2}$$

where θ is the polar angle of the projectile residues that can he obtained with the TPC tracking.

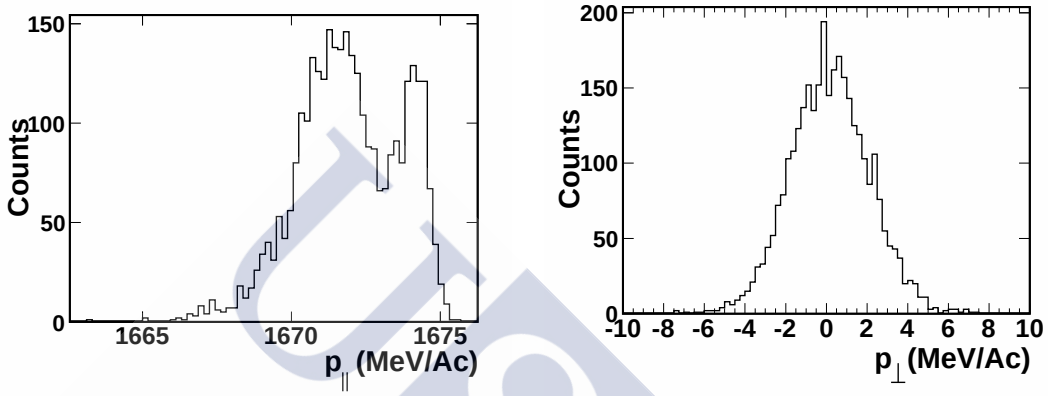

Figure 3.2: *Momentum Distributions in the Laboratory frame in the reaction of* $^{112}Sn(C,X)^{112}Sb$ *at 1GeV. Left panel: longitudinal momentum* $p_\parallel$ *. On the right panel: longitudinal momentum* $p_\perp$

In the figure 3.2 we compare the two components of the momentum in the reaction of $^{112}Sn(C,X)^{112}Sb$ at 1GeV. We can observe that the $p_\parallel$ is much larger than $p_\perp$ and for this reason, in our case, the transversal component is considered negligible.

3.3 Recoiling energy of projectile residues

From the magnetic rigidity or longitudinal momentum it is possible to determine the recoiling energy the projectile reaction residues. The relativistic kinetic energy at the intermediate image plane S2 can be obtained from the magnetic magnetic rigidity according to the following equation:

$$E_{S2} = A \cdot u \left[\sqrt{1 + \left(\frac{B\rho_{S2} \cdot Z \cdot c}{A \cdot u} \right)^2} - 1 \right] \tag{3.3}$$

Here u =(931.45 MeV/c^2)is the mass unit , A is the atomic number of the nucleus, $B\rho$ and Z are its magnetic rigidity and atomic number charge respec-

tively. The transformation of this observable into the frame of the moving projectile will provide the energy lost induced by the nuclear reaction.

3.3.1 Energy transformation at beam frame

In order to determine the energy of the projectile residues in the frame defined by the mean velocity of the incoming projectile nuclei in the middle of the target, it is necessary to correct the slowing down of the nuclei trough the layers of matter till the S2 or S4 focal planes.

Figure 3.3 illustrates the energy lost by the incoming projectiles in the different layers of matter located along of the beam-line until the middle of the target (E_0). The list of layers of matter placed along the FRS is presented in the appendix A.

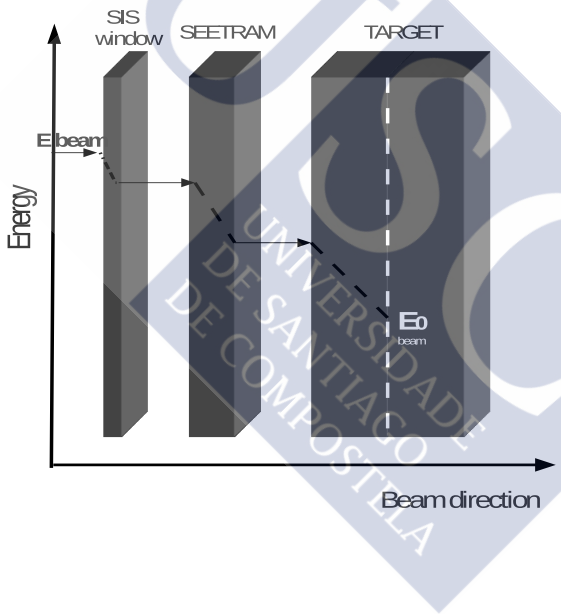

Figure 3.3: *Schematic diagram that represents the considerations done by us in order to determine the average velocity of the beam in the middle of the target. This approximation is important because this is the reference velocity used to calculate the Lorentz boost*

In order to obtain the energy or momentum distribution in the beam velocity frame, it is necessary to make a Lorentz transformation. The following equation give us the transformation between the references frames:

$$\begin{pmatrix} E_{bf} \\ p_{\parallel bf} \end{pmatrix} = \begin{pmatrix} \gamma_{vb} & -\gamma_{vb}\beta_{vb} \\ -\gamma_{vb}\beta_{vb} & \gamma_{vb} \end{pmatrix} \begin{pmatrix} E_{lab} \\ p_{\parallel lab} \end{pmatrix} \tag{3.4}$$

where $\gamma_{vb} = 1/\sqrt{1-\beta_{vb}}$, $\beta_{vb} = V_{vb}/c$; V_{vb} represent the beam velocity in the middle of the target, E_{lab} and $p_{\|lab}$ are the total energy and longitudinal momentum of the fragment in the laboratory frame respectively. From the equation 3.4 it is possible to obtain the longitudinal momentum $p_{\|bf}$ in the beam reference frame by the following way:

$$p_{\|bf} = \gamma_{vb}\left(p_{\|lab} - \beta_{vb}\frac{E_{lab}}{c}\right) \tag{3.5}$$

$$p_{\perp lab} = p_{\perp bf}$$

The transversal momentum $p_\perp$ is the same in both reference frames.

Also it is possible to obtain the energy in the beam particle frame (E_{bf}):

$$E_{bf} = \gamma_{bf}(E_{lab} - \beta_{bf}p_{\|lab}) \tag{3.6}$$

Figure 3.4 shows the energy distribution of ^{124}Sb projectile residues produced in the reaction $^{124}Sn(C,X)^{124}Sb$ in the beam-moving frame. In this reference frame the particles close to zero value are those with kinetic energy as the of the beam and correspond then to elastic reaction channels. Particles with negative energy indicate the kinetic energy loss induced by inelastic reaction channels. The two peaks observed in the figure correspond to elastic and inelastic isobar charge-exchange reactions that will be explained in the next chapter.

.

3.3.2 Energy resolution

The final energy resolution that could be achieved depends on several factors such as the resolving power of the spectrometer, the optical quality of the primary beam, the amount of matter along the FRS and the resolution of the position detectors. All these factors produce an extra broadening in the energy distributions that is not related to the reaction mechanism. The intrinsic energy resolution was evaluated by using the following equation:

$$\frac{\Delta E}{E} = \left(1 + \frac{Mc^2}{Mc^2 + E}\right)\frac{\Delta(B\rho)}{B\rho} \tag{3.7}$$

The equation 3.7 take into account the contribution of the resolution of the resolving power of the spectrometer. There additional effects will contribute quadratically to the final resolution according to the following equation:

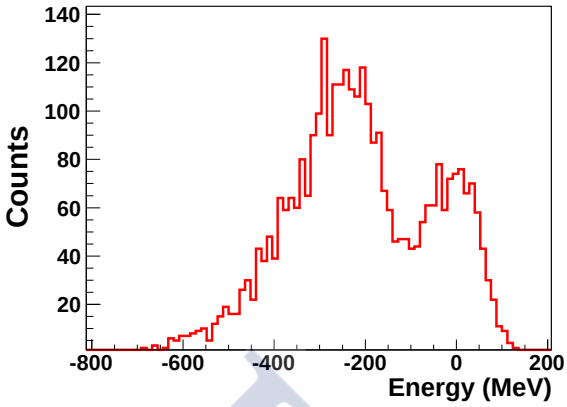

Figure 3.4: *Energy distribution for ^{124}Sb in the beam particle frame obtained by the np reaction channel of the ^{124}Sn on carbon target at 1GeV*

$$\left(\frac{\Delta E}{E}\right)_{exp} = \sqrt{\left(\frac{\Delta E}{E}\right)^2 + \left(\frac{\Delta E}{E}\right)^2_{str}} \tag{3.8}$$

The term $\left(\frac{\Delta E}{E}\right)_{str}$ is the straggling effects and beam emittance that affect the energy measure, this value is calculated using AMADEUS code [64]. These effects already was discussed in the section 3.2.

Table 3.1 summarize the energy resolution achieved for each target in the one step configuration. However, the resolutions achieved in the two step configuration are presented in the table 3.2 with higher values than one step configuration.

Target	Thickness (mg/cm^2)	$\Delta E/E(MeV)$
Carbon	197	10.0
Cooper	373	10.3
Lead	255	10.0

Table 3.1: *Energy Resolution in the beam particle frame using the one step configuration*

The energy value of the resolution calculated with the 3.7 and considering the beam-line matter appear in the tables 3.1 and 3.2. With the resolution achieved in 3.1 it possible to disentangle the elastic and quasielastic peaks.

Target	Thickness (mg/cm^2)	$\Delta E/E(MeV)$
Carbon	1400	28.5
Carbon	910	19.0

Table 3.2: *Energy Resolution in the beam particle frame using the two step configuration*

3.3.3 Unfolding of the experimental response

Using unfolding techniques one can try to extract the physical information of the experimental distribution. In this work, we used the Richardson-Lucy deconvolution method. An extended description of the method will be discuss in the appendix B [65] .

We assume that the measured energy of the beam ions distribution represents the response function of our experimental setup. Indeed, for the implementation of the deconvolution beam energy distribution contains the effect of the energy and location straggling, resolution of the detection system and the beam emittance. In Fig 3.5 we show the response function and the experimental distribution obtained for the reaction $^{124}Sn(C,X)^{124}Sb$ at 1GeV that we use as inputs of deconvolution method.

The Richardson-Lucy deconvolution is an iterative technique and as with other deconvolution techniques, the output of this method is iteration-dependent. This issue must be addressed carefully, particularly in those cases where the width of the distribution of a given observable is of interest, as in the case energy distributions that we will discuss in the chapter 4.

Figure 3.6 represents the unfolding dependence with the number of interations (N). In this test performed with this method revealed that the width of peaks in the true distribution become narrower in successive iterations.

In order to minimize the uncertanties associated with the oscillations or degradation of the solution in an iterative deconvolution, a method of regularization is necessary to define the optimal number of iterations [66].

In order to optimize the computing time, a relatively simple regularization method based on the χ^2 is proposed in this work. This χ^2 is applied to the unfolded and the original spectrum for each N iteration. Regularization methods and stopping criteria based on the standard χ^2 are well-known in other applications such as image reconstruction techniques [67, 68]. In some of these methods, the feasibility of the solution is measured with the χ^2 , and the process is stopped when this reaches a certain limit, preventing the solution to degrade. In the present case, we look for a minimum of the χ^2 in order to halt the deconvolution process.

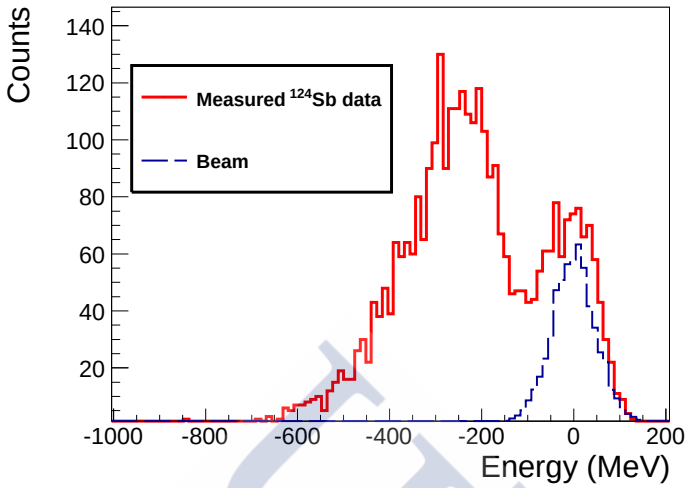

Figure 3.5: *Comparison between the beam energy distribution (^{124}Sn dashed line) and the ^{124}Sb (solid line) produced in the reaction $^{124}Sn(C,X)^{124}Sb$ at 1GeV in the beam particle frame. The beam energy distribution is the response function. The response function contains the contributions of the target thickness, energy-loss straggling, the beam emittance and the intrinsic resolution of FRS*

Correlations of calculated parameters

In general, the χ^2 value should be an indicator of the goodness of the result. In order to test this, we represent in Fig. 3.7 the correlation between the value of the χ^2 from the deconvolution method and the deviation of the result of each parameter in the case of three Breit- Wigner peaks (mean values and widths) respect to their corresponding true values. The panels show that the resulting values concentrate in the vicinity of the true distribution and χ^2 around 1. A collection of measured distributions Y is produced by varying the statistics and the binning of the histogram. Statistical fluctuations are taken into account changed the statistical counts by events. On the other hand, variations on the histogram binning change the number of points available to calculate the true distribution. The Richardson-Lucy deconvolution and the chi^2-based regularization method are applied to this collection of distributions. Interestingly, there seems to be no particular correlation between the value of χ^2 and the accuracy of the results at this stage.

Based on the results shown in Fig.3.7 , a mean and width value of each parameter would be a good approximation to the results of the deconvolution process. However, a further stage can be applied in order to improve the quality of the results: it is not unusual for deconvolution methods to yield

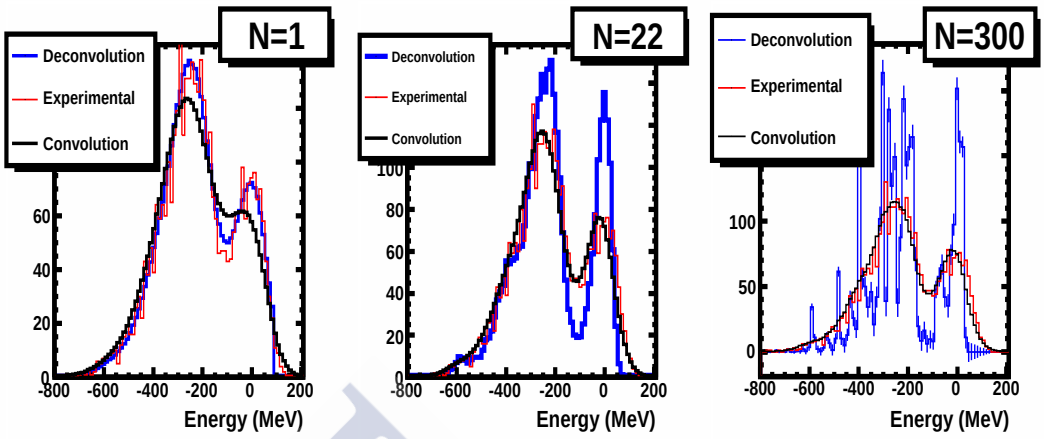

Figure 3.6: *Unfolding dependence with the number of interations (N): we can see the evolution of de deconvolution spectrum when the iteration number is increased. The convolution (black line) and its comparison withthe experimental data give us the χ^2 value used in the regularization method. The χ^2 value correspond to N=1 is 1.78, for N=22 we found a minimal value of $\chi^2 = 1.02$ and after this χ^2 is increased, for example for N=300 this $\chi^2 = 1.27$*

mathematical artifacts within the set of solutions. In order to separate these anomalies, we perform a robust average of the parameters describing the peaks found in the distribution. This procedure, based on the algorithm proposed by Rousseeuw and Van Driessen [69], searches within the set of solutions the subset that minimizes the sum of the standard deviations of the parameters. The minimum size of the subset is fixed at number of points +number of parameters+1/2. In this case we consider the systematic error in the unfolfing method is about $\frac{\Delta T}{T}_{Unf} \sim 8\%$ in the mean value estimation and 18% for width value estimation using the method described in the reference [65].

Then the final result will be given by the following equation:

$$\left(\frac{\Delta T}{T}\right)_f = \sqrt{\left(\frac{\Delta T}{T}\right)^2_{Unf} + \left(\frac{\Delta T}{T}\right)^2_{fit}} \tag{3.9}$$

This error value depends on the goodness of $\frac{\Delta T}{T}_{fit}$ because in the case of the mean value determination. Then this error depend must be analyzed thoroughly in each case.

In addition to the deconvolution process, it is necessary to substract the contribution of the reaction in the beam-layer materials. In fact this reactions

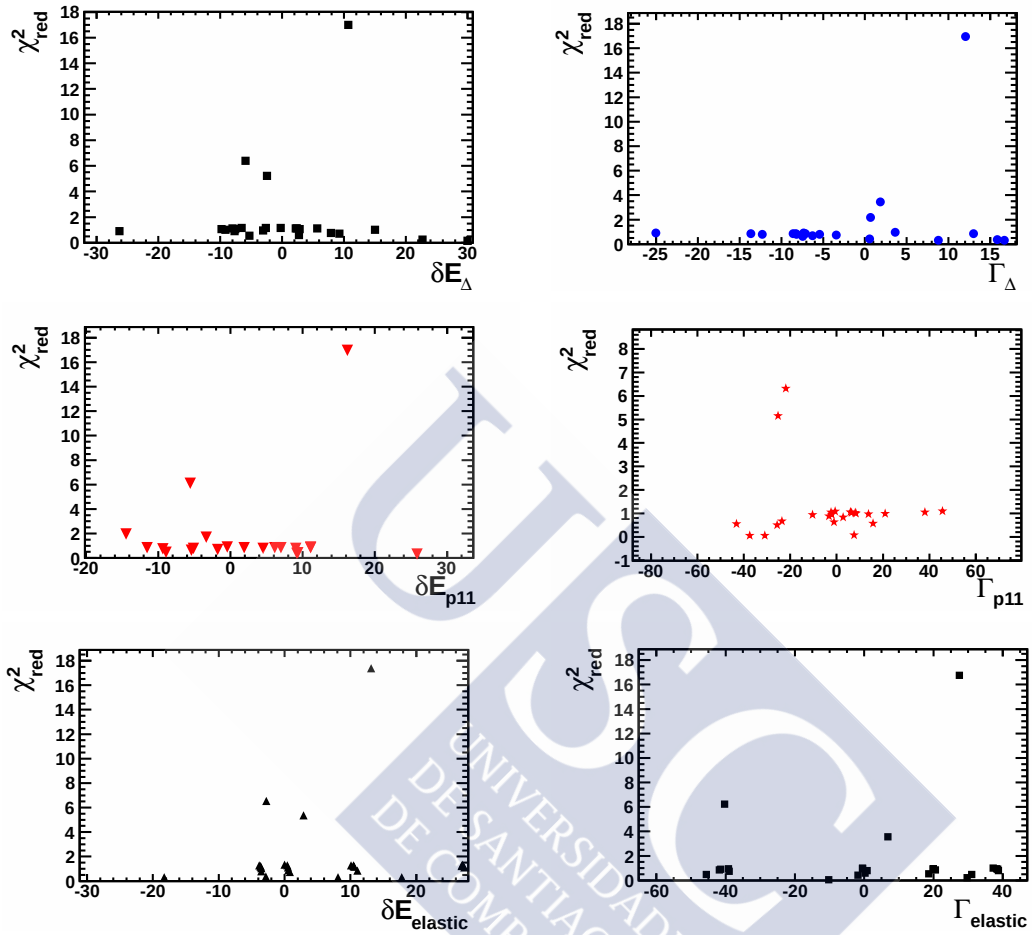

Figure 3.7: *Correlation between the value of the χ^2_{red} resulting from the deconvolution and regularization methods and the deviations in the mean (δE_i) and width values (Γ_i). At top part correspond to the mean and width values of the Δ resonance, the following plots correspond to the Roper resonant δE_{P11} and Γ_{P11} mean and width values respectively and $\delta E_{elastic}$ and $\Gamma_{elastic}$. Each point corresponds to the correlation for a particular binning and number of counts in the histogram.*

increase the number of counts and modify the energy distributions . In the section 3.5.2 this effect was already corrected in the case of the section measure.

Figure 3.8 represents the energy distribution (solid line) and its deconvolution (dashed line). The final energy distribution obtained by the unfolding method represents the physical information without response function contributions. The final energy distribution shows the two energy contributions:

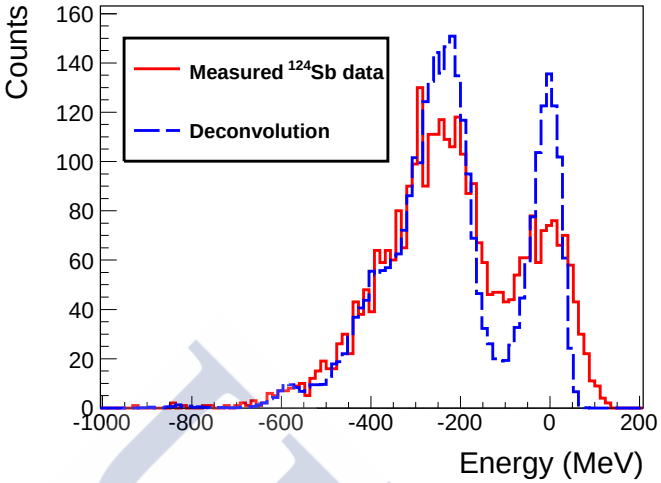

Figure 3.8: *Figure represents the energy distribution (solid line) and its deconvolution (dashed line). The final energy distribution obtained by the unfolding method represents the physical information without response function contributions.*

the quasielastic and the inelastic channel. This components will be analyzed in the following sections. The fit procedure will be explained in the next chapter in the section 4.4.

3.4 Angular distributions of charge-exchange reaction residues

Using the position obtained with the TPC's it is possible to obtain the angle between these tracking detectors. The following relation shows the way to calculate the forward angle in the laboratory frame θ_{lab}

$$\theta_{lab} = tan\left(\frac{X_{3pos} - X_{2pos}}{Dist_{32}}\right) \tag{3.10}$$

where X_{3pos} and X_{2pos} are the position in each respective TPC, $Dist_{32}$ is the distance between the TPC's. Using the position resolution it is possible to obtain the angular resolution in the laboratory frame, this value is around $0.708 mrad$.

To obtain the angle in the center mass frame (CM) we need to express

it in the following way:

$$\theta_{CM} = atan\left(\frac{sin(\theta_{Lab})}{\gamma(cos(\theta_{Lab}) - \frac{V_{beam}}{V_p})}\right) \tag{3.11}$$

where V_{beam} and V_p are the velocities of beam and particle respectively and $\gamma = \sqrt{\frac{1}{1-\beta^2}}$. The figure 3.9 shows the angular distribution in the reaction $^{112}Sn(C,X)^{112}Sb$ at 1GeV. In this plots it is clear that the charge-exchange reaction produce a peak that appears at 0°.

Angular resolution

The resolution in the position measure affect the calculation of the forward angle . First we consider the angular resolution obtained by the propagation of uncertainty of position measure give in the next equation:

$$\frac{\Delta\theta}{\theta} \sim \frac{\Delta x}{Dist_{ij}} - \frac{X_{jpos} - X_{ipos}}{\Delta Dist_{ji}^2} \tag{3.12}$$

where Δx and $\Delta Dist_{ji}$ are the position uncertanties of the TPC measure and the distance between de TPC's respectively.

But the total angular measure is affected by the angular straggling. Due to the electromagnetic interaction of the nuclei with the material layers the direction of the fragment changes. This contribution is around $\frac{\Delta\theta}{\theta}_{st}$ $\sim 0.60mrad$.

This effect changes the original angle and alters the angular distribution as well. Then the final angular resolution $\frac{\Delta\theta}{\theta}_{lab}$ is given by the position resolution calculation $\frac{\Delta\theta}{\theta}$ and the angular straggling contribution $\frac{\Delta\theta}{\theta}_{st}$ by the following way:

$$\left(\frac{\Delta\theta}{\theta}\right)_{lab} = \sqrt{\left(\frac{\Delta\theta}{\theta}\right)^2 + \left(\frac{\Delta\theta}{\theta}\right)_{st}^2} \tag{3.13}$$

Using the equations in 3.13 it is possible to obtain the resolution in the CM frame, this value is about $\sim 0.7°$

3.5 Cross Sections

In this experiment the physical observables that we measured in order to determine a good description of the isobaric charge-exchange reaction are the cross sections and the energy distributions of the recoiling nuclei product of

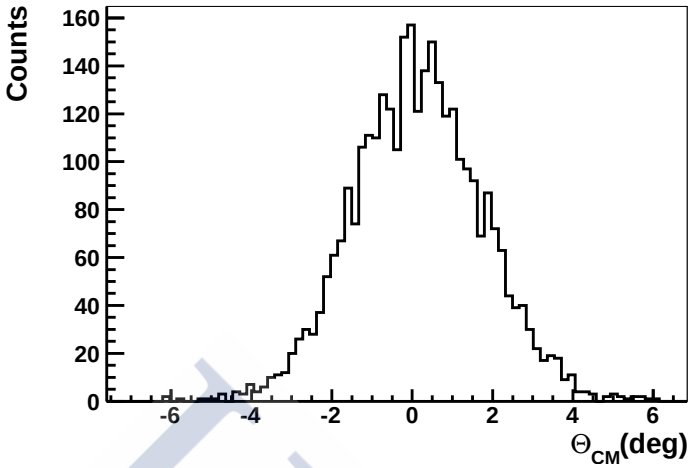

Figure 3.9: *Angular Distributions of* $^{112}Sn(C,X)^{112}Sb$ *at 1GeV in the CM frame*

this reaction. The cross section gives us information about of the content of neutrons and protons in the nuclear periphery. The energy distribution gives us direct information of the quasielastic and inelastic channels that allows us to characterize the Δ resonance in the nuclear medium across physical parameters as the mean value of the energy and the width of the distribution. This chapter deals with experimental technique and the calculation of the cross section. The reactions produced at $S0$ in the one-step configuration (see 2.3.1) are corrected with the factors that will be described in the next section. A particular case of the cross sections measures using the two step configuration will be studied in the section 3.6.

3.5.1 Determination of the cross sections

The cross section is determined by the production of every nucleus normalized to the number of projectile and the number of atoms per cm^2 of each target.

$$\sigma = \frac{y \cdot C_f}{N_t N_b} \tag{3.14}$$

In this equation N_b is the number of projectiles determinate using the equation 2.1, N_t is the number of atoms per unit of area, y is the number of counts of the nucleus corrected with its subtraction of *empty target*. The *empty target* is a measurement without any target in order to check the production of charge exchange products in the different layers of the beamline. The factor C_f considers all corrections that are applied to cross section

give us the real measure of this quantity. This factor is defined in the following way:

$$C_f = f_{dead} \cdot f_{ch.st} \cdot f_{sec} \tag{3.15}$$

The correction factors given in the equation 3.15 in the term C_f were the dead time of the acquisition system f_{dead}, f_{sec} which corrects the secondary reactions in the different material layers in the beam line and $f_{ch.st}$ takes into a count the production of ionic-charge states.

3.5.2 Background subtraction

In order to determinate the background contribution of the beam-line layers we measured charge-exchange reactions without target . The actual cross section is written in the following way:

$$\sigma_t = (\frac{M_t}{d_t N_A})(p_t - p_{empty}) \tag{3.16}$$

where M_t is the molar mass of the target material (g/mol), d_t is the target thickness (g/cm^2), and N_A is the Avogadro number (mol $^{-1}$) and p is the iteration probability expressed by following equation:

$$p = \frac{y}{Np} \tag{3.17}$$

y is the number of counts of events in a reaction channel and N_p the number of projectiles.

This correction factor is less than of 2 % in the Sb residues. In the case of indium particle residue is less than of 20 %, in the case the beam charge charge state affect the contribution of indium production and for this reason the background is higher than in the case of antimony residues

For the similar form, it is possible to extract the proton contribution of the plastic CH_2. In this case the carbon (C) is treated like the background. The principal way to subtract the C is using the following equation

$$\sigma_{proton} = \frac{1}{2}\left[(\frac{M_{CH_2}}{d_{CH_2} N_A})(p_{CH_2} - p_{empty}) - (\frac{M_C}{d_C N_A})(p_C - p_{empty})\right] \tag{3.18}$$

where σ_{proton} is the proton cross section.

3.5.3 Dead Time

One of the limitations while using very intense beams is the dead time of the data acquisition system. For this reason not all the events remain registered by means of system *trigger*. Thus we underestimate the counts of reaction nuclei. Therefore, the factor of dead time f_{dead} measures the quantity of real processed events that produce a trigger (N_{free}) and the events that are processed or "*accepted*" by the acquisition (N_{acc}). Hereby the factor f_{dead} is expressed in the following way:

$$f_{dead} = \frac{N_{free}}{N_{acc}} \tag{3.19}$$

This value was kept below the 30 % in order to obtain trustworthy measures of the number of events.

3.5.4 Secondary Reactions

The factor f_{sec} corrects the secondary reactions that occur in the different layers of material in the beam line. The reaction yields produced in the isobaric charge-exchange reaction can suffer secondary reactions after it leaves the target. Due to this fact the count realized in the corresponding focal plane is lower due to the loss of particles. In order to calculate this correction factor it is necessary to determine the total probability of interaction (σ_{tot}) in each material layer . The code Karol [70] was used in order to obtain each σ_{tot} in each material layer. Hereby the factor of correction for secondary reactions is:

$$f_{sec} = \prod_{i=1}^{n} P_i \tag{3.20}$$

The factor P_i is the probability of survival in the matter layer i. The average value of this correction was approximately of the 10 %. It is also possible to consider an additional factor related to the secondary reactions inside the target (f_t). But the nature of the isobaric charge-exchange reaction in this case should be neglected, so for this reaction the value of this factor is $f_t \sim 1$.

3.5.5 Ionic charge states

A nucleus produced in a reaction can change its charge due to the electromanetic interaction with different atoms in the layers of matter across the beam-line [71]. This effect can alterate the measure of the A/Q ratio and therefore affect the number of counts necessary for the determination of cross section.

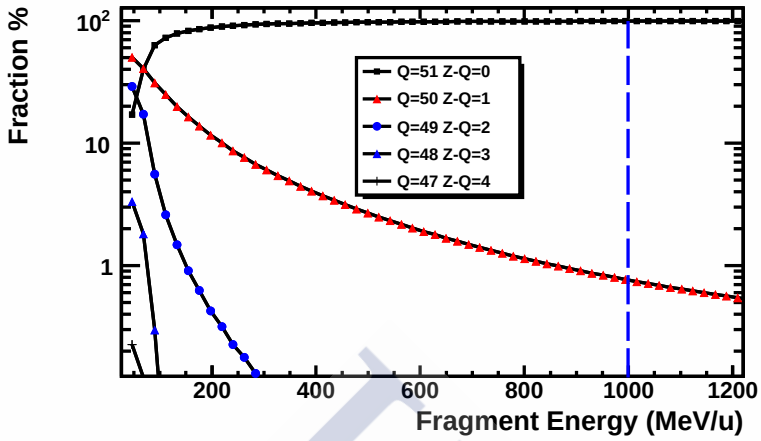

Figure 3.10: *^{112}Sb equilibrium charge distribution in the middle focal plane: Fraction of charge-states configurations as a function of fragment Energy. At 1GeV (vertical dashed lined) the charge state $Z - Q = 1$ have a probability around $\sim 1\%$ and the contribution of the other charge states are negligible at this energy.*

In order to determine how the equilibrium charge-state is altered in the first and second stages of FRS due to the layers placed in the focal planes we used GLOBAL code. GLOBAL is a program to calculate ionic charge-state distributions of projectiles traversing solid and gaseous targets. The program was developed for the interaction of projectiles having a nuclear charge larger than 28 with any target. Details of the underlying physics as well as of a comparison between experiment and predictions by GLOBAL can be found in [72]. The contribution of Ionic charge state correction in our experiment is allways less than $\sim 1\%$ (see Fig 3.10).

3.6 Reactions using secondary beams

In the two step configuration the FRS was used as two independent magnetic spectrometers. In the first stage we separated and identified the secondary beam of exotic projectiles. The second stage give us the identification of the residual nuclei produced in the interaction of the secondary beam with the reaction target at $S2$. In the two-step configuration the primary beam coming from the heavy ion synchrotron, impinged on the production target placed at $S0$ plane in order to produce the secondary beam of exotic nuclei. The fragments produced by this mechanism were focused into the FRS. A reaction target was placed at the dispersive focal plane to induce interaction

of those nuclei whose interaction cross sections we wanted to determine.

To measure the cross section with unstable beams we used the experimental set up described in the figure 2.7. The number of projectiles that impinging directly on the reaction target located in the intermediate focal plane is determined by the number of counts of a fragment in the identification matrix. To measure the fragments in the intermediate focal plane it is necessary to take into account the different types of *triggers* and *downscaling* factors of these triggers in each focal planes.

We used two different triggers in the two step stage to determine the cross section of the fragments produced in the reaction target at S2. This trigger system was required to calculate the number of projectiles that income to the secondary reaction target at S2. One of the triggers was given by the scintillator placed at S4 (trigger==3). This trigger corresponds to those ions that arrived to the final focal plane of the FRS. All the detectors were registered by the data acquisition system (DAQ) when receive trigger==3 signal. The other trigger was given by the scintillator placed at S2 (trigger==1) which corresponded to particles that arrived to the dispersive focal plane at S2. If the DAQ was triggered by trigger==1, only the signals of the detectors of the first part of the experimental set-up were registered. This trigger was necessary for the determination of the number of incident projectiles for the determination of the fragmentation cross sections. Unfortunately, the DAQ acquisition is an important constraint in this experiment, because we had dead time contribution in the determination of the number of projectiles and the final yields production. We can distinguish two types of dead time: first at S2 (affect the estimation of projectile) and another dead time at S4 (affect the estimation of reaction products). We can determine these dead time from the direct comparison with its respective plastic scaler signal. Then in order to determine the cross section in the two step stage it is necessary to use this equation:

$$\sigma = \frac{y \cdot C_f Dt_{S4}}{N_t N_b Dt_{S2}} \tag{3.21}$$

where N_b is the number of projectiles determinate using the equation 2.1, N_t is the number of atoms per unit of area, y is the number of counts of fragments produced in a nuclear reaction. Dt_{S2} and Dt_{S4} are the dead time of acquisition at S2 and S4 respectively. The factor correction C_f used in the equation 3.21 for the reactions with secondary beams correct the particles that are produced in the reaction in S2 and that are identified in S4:

$$C_f = f_{ch.st} \cdot f_{sec} \tag{3.22}$$

The correction factors considered in this term of C_f are f_{sec} that correct

the secondary reactions in the different material layers in the beam-line and $f_{ch.st}$ correct the production of the charge states.

CHAPTER 4

Isobaric Charge exchange reactions

As explained in chapter 1, charge exchange reactions manifest in two energy regimes: A low energies regime with nuclear excitations such as Gamow –Teller, Spin Dipole etc and high energy regime with mucleonic excitations. Charge exchange reactions constitute a useful tool in nuclear structure research. The (n,p) and (p,n) channels are often used to obtain the Gamow-Teller matrix elements which can not be extracted from $\beta-$decay experiments (see for example [36, 37]). At intermediate and high energies, above a pion production threshold, it is possible to excite nucleon-resonances.

In the particular case of charge-exchange reactions, the real pion produced in the inelastic channel must escape in order to preserve the isobar feature of this reaction.

This work offers a novel technique in order to understand the charge exchange with heavy ions and different targets and energies. With this systematic approach it is possible to study the isospin dependence of the charge exchange reaction and the energy dependence , for special in the inelastic channel.

We measured the isobaric proton and neutron charge exchange reactions induced by different Sn isotopes with the subsequent production of Sb and In residues. The high resolution of the FRS made it possible to disentangle the quasi-elastic and resonant processes leading to the formation of those channels. Moreover, the spectrometer resolution was improved using an unfolding technique. with the response function of the experimental setup..

In this chapter we will describe the results for two physical observables we propose for investigating these reactions; the recoiling energy spectrum

of the reaction residues and cross section of two charge exchange reaction channels (np and pn). The recoiling energy distributions of the reaction residues produced in isobaric charge-exchange reactions are described by the contributions of the quasi elastic and inelastic channels. In addition, using deconvolution techniques, it is possible to distinguish several nucleonic excitations in form of resonances and characterize them in terms of their widths and mean values. Technical details of the unfolding method will be explained in the appendix B. Once we obtained a complete description of every channel, it is possible to use the procedure explained in the previous chapter and to determine the cross section of each channel.

4.1 Systematic study of isobaric charge exchange reactions at relativistic energies

Using the FRS it is possible to measure the n-p and p-n isobar charge-exchange channels in the same experiment. The isobar charge-exchange reaction of Sn projectiles produces two final residues of antimony and indium having the same number of nucleons as the projectile nuclei.

The systematic study of the charge exchange reactions using projectiles with different neutron excess required the use of the one and two step configuration of the FRS that was explained in sections 2.3.1 and 2.3.2. In the one step configuration ^{112}Sn and ^{124}Sn stable beams were used to produce the charge exchange reaction while two step configuration was used to study charge exchange reactions with unstable tin isotopes.

In the one-step reaction scheme a stable beam impinges a reaction target placed at the entrance of the FRS. In this case it is possible to identify of the projectile reaction residues in the middle or the final focal plane of the spectrometer. In the two-step reaction scheme, the unstable isotope is produced at the production target located at the entrance of the FRS, and identified and separated using the first section of the FRS. Then, isobar charge-exchange reactions are induced in a second target placed at the intermediate image plane. The reaction fragments are identified with the second section of the spectrometer. In addition to the systematic analysis using different projectiles, we studied the dependence of the isobar charge-exchange reactions with the nature of the target and the beam energy. These measures were performed using the one step set up of FRS. The objective of the analysis of the with stable projectiles measurements with different targets to study the dependence of charge exchange reaction with the target mass [73, 74, 75]. On other hand, the energy dependence research was performed

in order to understand the dependence of the nucleonic resonances excitation with the beam energy.

The table 4.1 summarizes the experimental charge exchange reactions measured in this work.

Target Place	Beam	E_b(MeV)	Thickness(mg/cm^2)	Fragment
S0	^{112}Sn	1000	C(100)	^{112}Sb,^{112}In
			PE(95)	
			Cu(373)	
			Pb(255)	
S0	^{124}Sn	1000	C(197)	^{124}Sb,^{124}In
			PE(95)	
			Cu(373)	
			Pb(954)	
S0	^{112}Sn	700	C(100)	^{112}Sb,^{112}In
		400	PE(95)	
S2	^{110}Sn	1000	C(910)	^{110}Sb
	^{120}Sn		C(1400)	^{120}In,^{120}Sb
	^{122}Sn			^{122}Sb

Table 4.1: *List of fragments obtained by the reaction of Sn beams at different energies E_b. It is important to note that the complete data set is a mix of the one and two steps set-up*

Figure 4.1 illustrates the clear identification plot obtained for the two isobar change-exchange projectile residues (p,n) and (n,p) produced in the reaction $^{112}Sn + C$ obtained using the FRS.

This identification allowed us to determine, with high precision, the production cross-sections of all the single charge exchange residues created in peripheral reactions of Sn projectile with different targets following the procedure described in section 3.5 .

4.2 Recoiling energy distributions of projectile residues

In order to investigate the isobar charge exchange reaction mechanism we propose to use as observable the recoiling energy of the projectile residues in the reference frame defined by the velocity of the projectiles in the middle of the target. Since those spectra represent the kinetic energy lost by the projectiles in the reaction they are called missing energy spectra. Figure

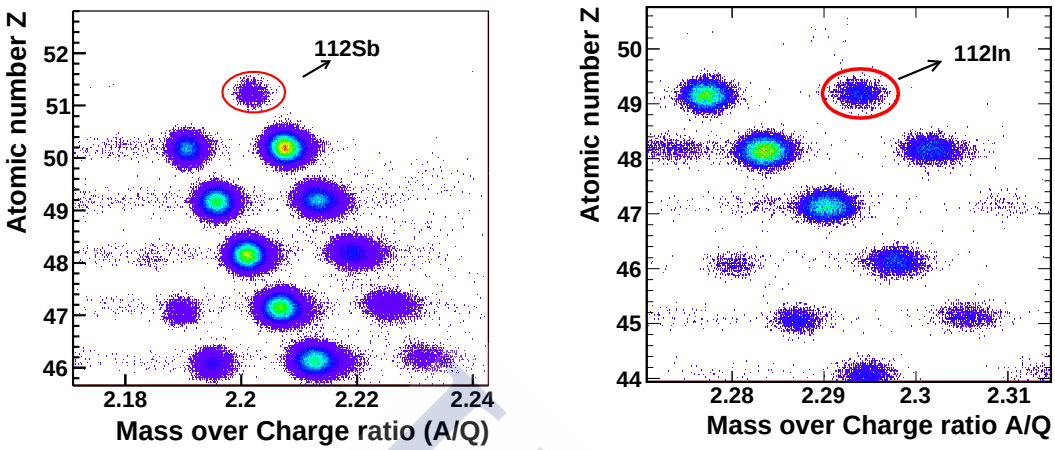

Figure 4.1: *Atomic number (Z) as a function mass-over-charge ratio A/Q of fragments produced in the reaction $^{112}Sn + C$ at 1GeV. Left panel: n-p channel production (^{112}Sb). Right panel : p-n channel production (^{112}In)*

4.2 shows the missing energy spectra for ^{124}Sb. In this figure we can to observe two bumps, one around to $0MeV$ energy value corresponding to quasi elastic charge exchange processes and a second one around ∼-250 MeV corresponding to charge-exchange processes where the projectile lose quite some kinetic energy.

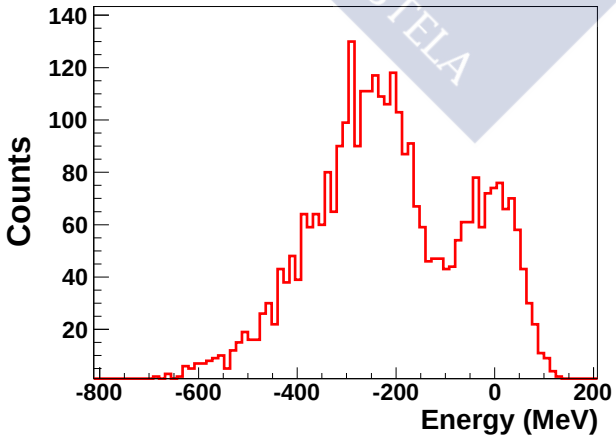

Figure 4.2: *Missing energy spectrum for ^{124}Sb in the reaction $^{124}Sn(C,X)^{124}Sb$ at 1GeV in the beam-particle frame.*

The quasielastic peak corresponds to nuclear isovectorial transitions at low energy as was explained in the chapter 1. The physical process that contribute to the quasielastic region are Fermi, Gamow—Teller, spin dipole and giant dipole transitions principally [37]. Figure 4.4 is a schematic representation of $n-p$ and $p-n$ channel through of the virtual pion exchange in the quaselastic region. At low energy regime, the charge exchange reaction are governed by the $\Delta T = 1$ transitions with the subsequent collective modes excitations.

It is important to remark that in this experiment the information of proton target was obtained from the sustraction of the polyethylene target PE and carbon target. This sustraction includes the scaling of each energy distributions using the procedure explained in the section 3.5.2. Figure 4.3 illustrate this procedure where the the proton information is obtained from the sustraction of the two unfolded distributions.

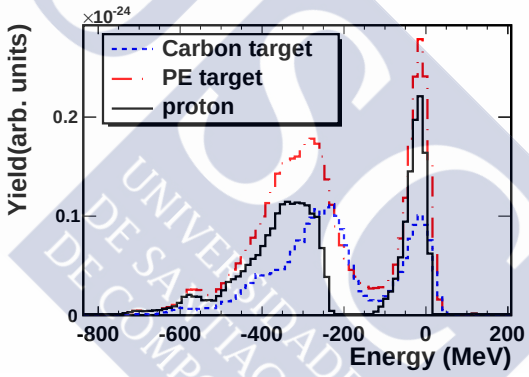

Figure 4.3: *Sustraction process of the two unfolded distributions in order to obtain the proton target information in the production of* ^{124}Sb *at 1GeV*

The second contribution in the missing energy spectra corresponding to large values of missed energy, represents nucleon excitations. Figure 4.5 represents the resonance excitation with the real pion production in the target and the projectile.

We observe the inelastic region due to the fact that the real pion produced in the nucleon resonance decay must leave the nucleus in order to preserve the isobaric condition of this reaction. The pion carries mass and kinetic energy which momentum and energy conservation translates as a projectile recoil leading to negative values in the missing energy spectra.

Due to our energy resolution around ($\frac{\Delta E}{E} \sim 12MeV$) it is impossible to disentangle each isovectorial transitions components in the quasielastic region. Moreover, other possible observable that could give us information it

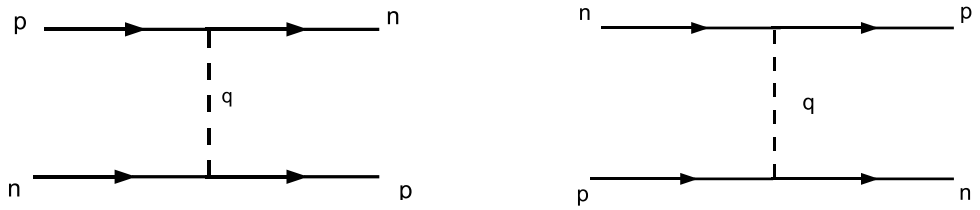

Figure 4.4: *Schematic representation of $n-p$ and $p-n$ channel through of the virtual pion exchange in the quaselastic region.*

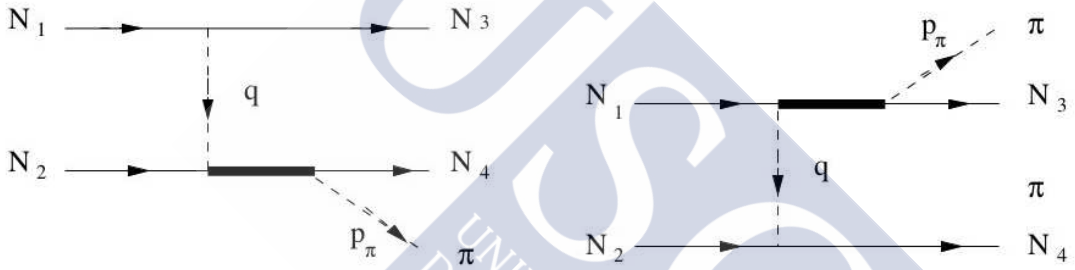

Figure 4.5: *Schematic representation of the real pion exchange in the inelastic region. The top part of each the diagram represents the projectile, while the* ***bottom*** *one is the target. Left panel: nucleon resonance excitation in the target(solid line) with the subsequent pion and nucleon emission . Right panel: nucleon resonance excitation in pion the excitation in the projectile*

is the angular distributions.

In order to explore this region of the missing energy spectrum necessary use other experiments with resolutions of 25-50 MeV, see for example the reference [37] and references therein. However, it is possible to improve the experimental resolution to observe different baryonic excitations, as we will discuss in the next section.

4.2.1 Comparison with previous experiments

The inelastic channel in isobar charge-exchange reactions can be used to investigate the in-medium behavior of the Δ resonance.

For these reason, a complete program to measure the Δ excitation in nucleus-nucleus collisions [73] in order to understand the charge exchange reactions of different light and medium mass projectiles was carried out at the accelerator SATURNE in Saclay. In this program reactions using ^{6}Li, ^{12}C, ^{16}O, ^{20}Ne, and ^{40}Ar projectiles at energies around 1 GeV per nucleon ([74, 75]).

As in our case, the observable used to investigate these reactions was the missing energy spectra of the projectile residues. These missing energy spectra were obtained from the longitudinal momentum of the projectile residues measured with the spectrometer SPES IV with a typical resolution $\Delta p/p = \pm 7 \times 10^{-4}$. More recently, the FRagment Separator (FRS) at GSI (Darmstadt) was used to investigate charge exchange reaction using heavy ions [76]. In this case, a Pb beam at 1 A GeV was used to induce isobaric charge-exchange reactions in proton, deuterium, and titanium targets, leading to the production of ^{208}Bi. The recoiling nuclei were isotopically identified with the FRS. The corresponding longitudinal-momentum distributions showed two components that were associated to quasi-elastic and inelastic charge-exchange reaction channels.

Figure 4.6 shows a qualitative comparison between missing energy spectra of the charge-exchange reaction results obtained in Saturne [73, 74, 75] and this work. One the one hand the Saturne experiment used ^{20}Ne beams at 900 MeV/n. On other hand, we present ^{112}Sb at 1 GeV results.

It is clear the good agreement with the Saturne experiments and the presence of the quasielastic and inelastic channels. In both experiments it is possible to disentangle the quasielastic and inelastic peaks. It is important to note the absence of the quasielastic peak in the pn channel prodiction on the proton targets. This effect is explained by the charge conservation involves in this reaction.

By direct comparison, it is possible to observe that in the previous Saturne measurements and the results obtained in this work the $\Delta-$ resonance production in each channel. At this energies, the Δ peak occupies a significant part of the spectra in each case.

In the both experimental results, the pn channel shows a higher contribution of the quasielastic channel with respect to the inelastic channel. The opposite effect is seen in the np channel.

The isospin systematic using different targets study shows us a clear dependence with this quantity. This heavy-ion-induced reaction show a shift in the Δ peak with respect to the $\Delta-$resonance mean value obtained in the proton target. This effect will be presented in the section 4.4.

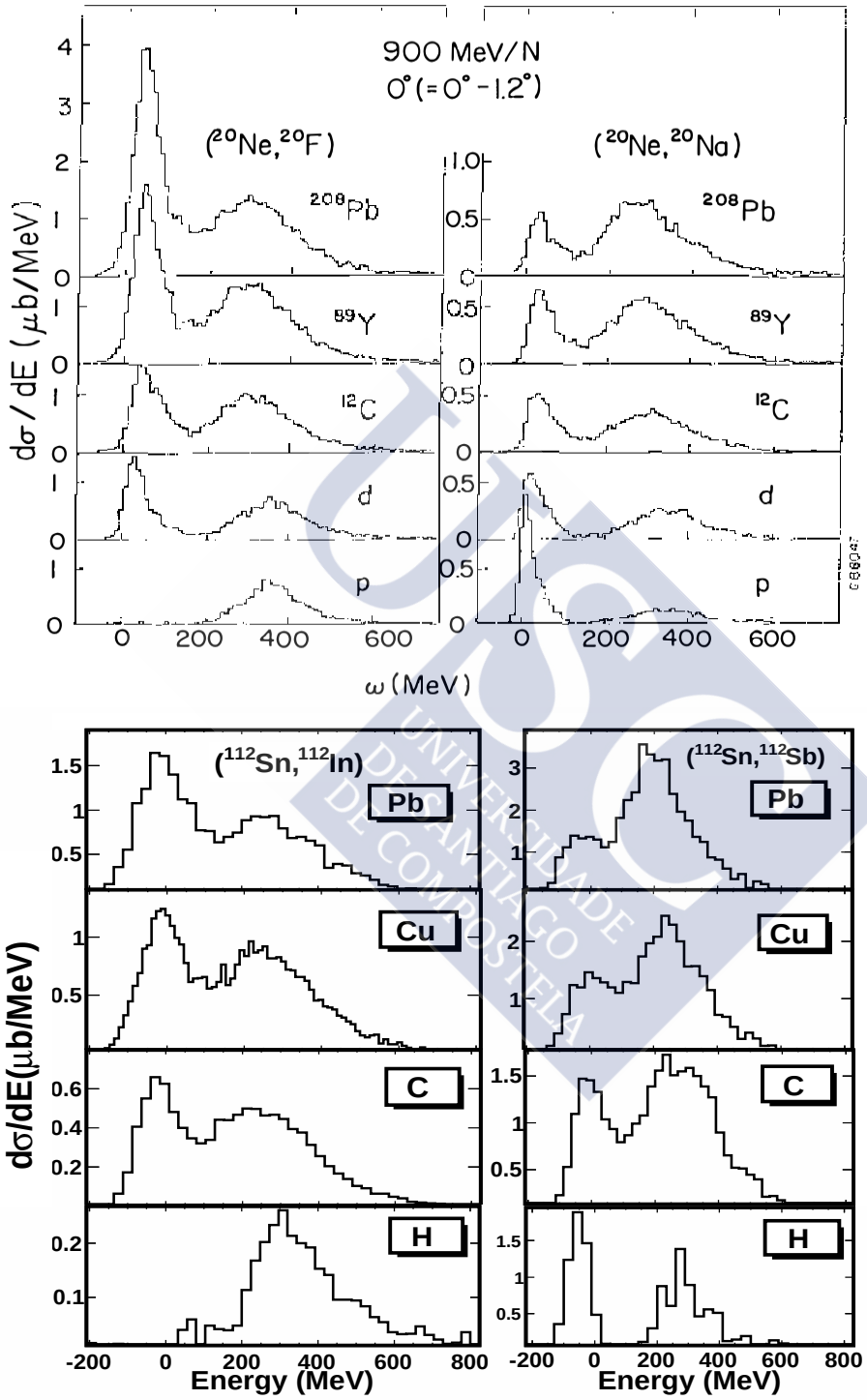

Figure 4.6: *Comparison between missing energy distributions from e Saturne [73] and this work results. Left panel: Zero-degree spectra for charge exchange reactions with a ^{20}Ne beam at 900 MeV per nucleon. Right panel: Energy recoil distribution at projectile frame was obtained in this work without unfolding procedure.*

4.2.2 Results of reactions using stable beams

In this experiment we used beams of two stable isotopes of tin, ^{112}Sn and ^{124}Sn. For this measurements the reaction target was placed at the entrance of the fragment separator. In these measurements we were not limited by the intensity of the beams, therefore we could use rather thin targets improving the resolution of the measurement as discussed in section 3.2. Table 4.1 shows the complete list of targets and beam energies used in our measurements.

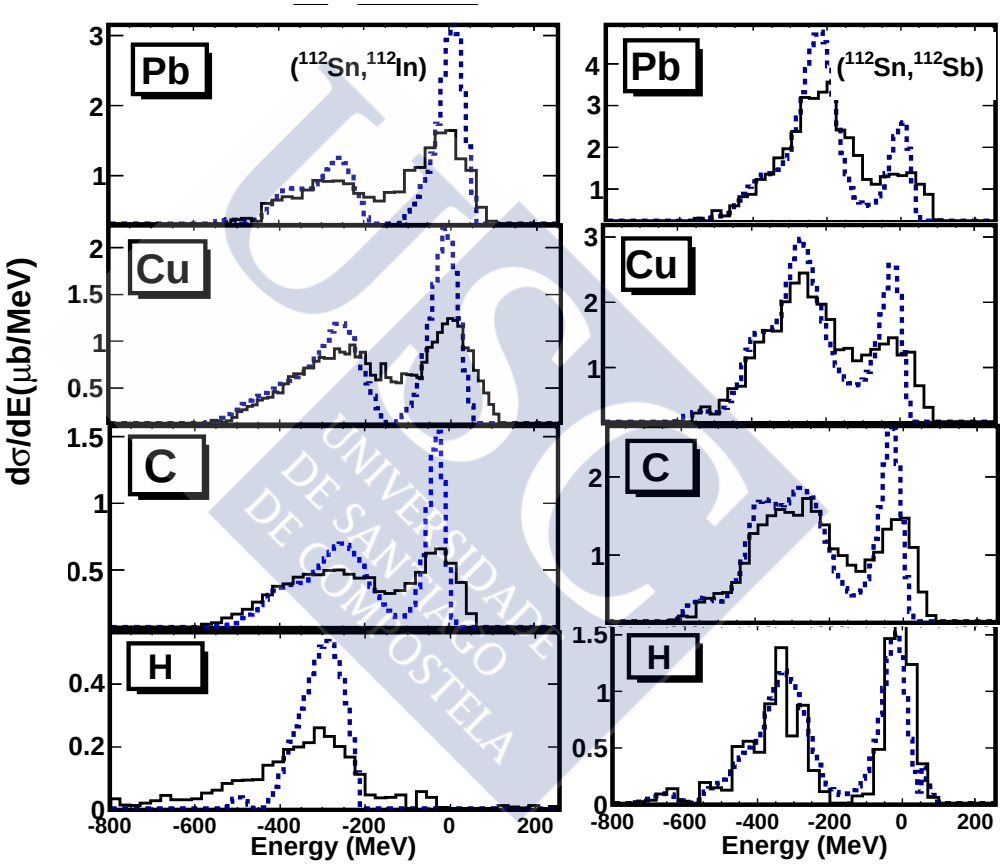

Figure 4.7: *Energy recoil distributions in the beam particle frame. Distributions (solid line) obtained using the reaction the n-p and p-n channels of ^{112}Sn on different targets are unfolded (dotted line) to obtain the physical information.*

Figs. 4.7 and 4.8 display the missing energy spectra obtained with these two beams on different targets. As can be seen, with the ^{112}Sn beam we could measure the two isobaric charge-exchange channels leading to the production of ^{112}In (p,n) and ^{112}Sb (n,p). However, with the ^{124}Sn beam we only measured the (n,p) channel producing ^{124}Sb. In these figures the black his-

tograms represent the missing energy spectra as obtained from the measured longitudinal momentum distributions following the procedure described in section 3.3. The dashed line corresponds to the unfolding of the spectra by the response function of the experimental setup defined from measurements with the primary beam using the procedure described in section 3.3.3.

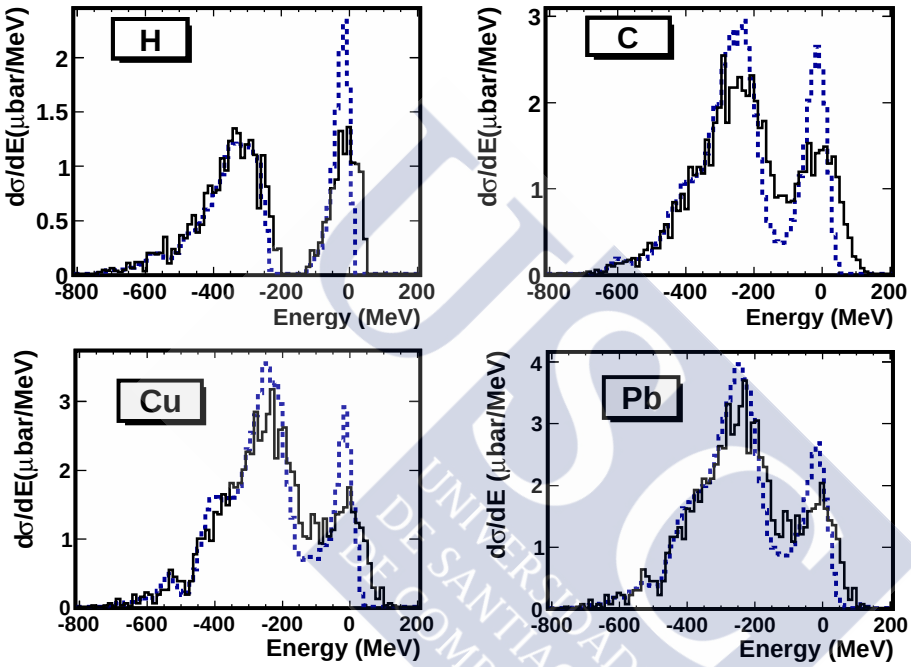

Figure 4.8: *Energy recoil distributions of ^{124}Sb in the beam particle frame. The distributions (solid line) was obtained using the reaction the n-p of ^{124}Sn impinging on different targets. The unfolded (dotted line) represent the physical information.*

For all the targets and beams we clearly identify the quasi-elastic and inelastic contributions to the charge-exchange reaction. In the particular case of the production of ^{112}In in reactions induced by ^{112}Sn on hydrogen we do not observe the quasi-elastic channel. This result can be understood by charge conservation. The figures also illustrate the improvement in resolution brought by the unfolding of the response function of the experimental setup.

The experimental setup also allowed us to determine the cross sections of the isobar charge-exchange channels using the method described in the section 3.5. Indeed, Figs. 4.7 and 4.8 are normalized to the corresponding cross sections that are listed in table 4.2 with the corresponding uncertainties. Moreover , in Fig. 4.9 we depict the evolution of the cross sections of the two

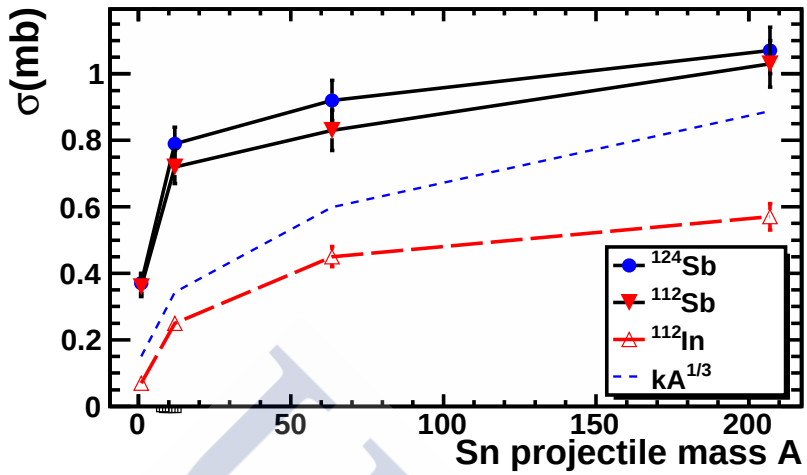

Figure 4.9: *Behavior of the total cross section with different targets with mass number A. In this figure it is possible to observe a clear dependence of the effective section so much for the channel np (^{112}Sb) and the channel pn (^{112}In) as well as a clear separation between the probability of production of Sb on In.*

isobar charge-exchange channels with the mass number of the target nuclei for the two stable projectiles (^{112}Sn and ^{124}Sn) at 1000A MeV. The figure shows a clear increase of the charge-exchange reaction cross section with the mass number of the target nuclei for the two isobar charge-exchange channels and for the two projectiles. However, one observes that the cross sections are larger for the (n,p) channel and for the ^{124}Sn projectiles for all the targets.

The larger cross sections for the (n,p) channel (around a factor two larger than the (p,n) channel) could be understood as due to the larger density of neutrons at the surface of both projectiles. The same reason would explain the larger cross sections measured with ^{124}Sn than with ^{112}Sn. The peripheral character of these reactions would correspond to an increase of the cross sections with the radius of the target nuclei and then with $\propto A^{\frac{1}{3}}$. Such an evolution is represented in Fig. 4.9 by the dashed line. However, the measurements show a smother evolution of the cross sections than expected with this simple model. Therefore, a detailed description of this reaction mechanism is required for a complete understanding of these cross sections.

.

Figure 4.10 shows the cross section for each channel. In the case of the quasi-elastic channel it is possible to observe that cross section dependence with the target mass (A) is almost constant but in the case of the inelastic channel is clear that the cross section is increased with the increment

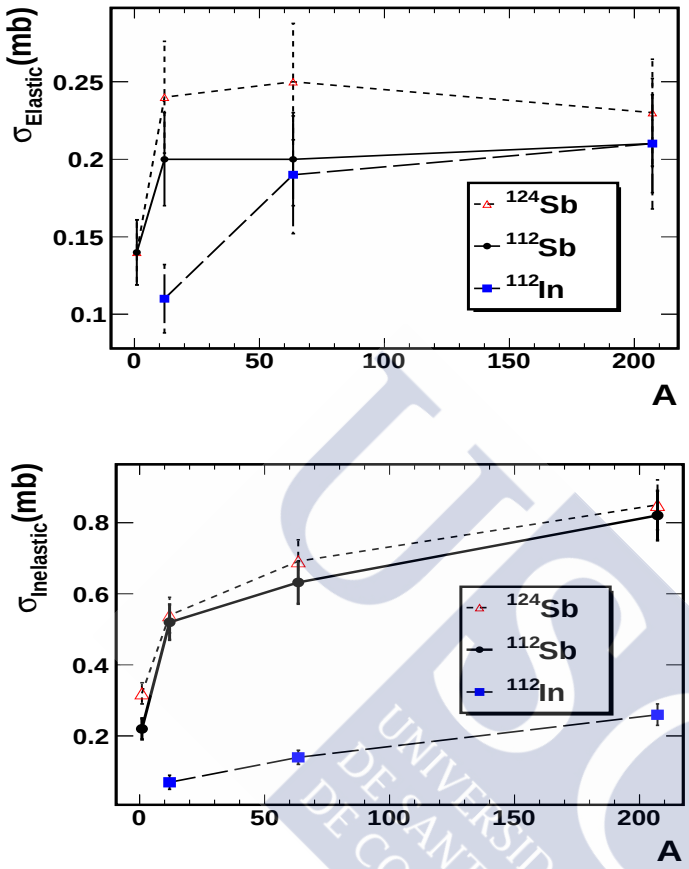

Figure 4.10: *Cross section of the elastic and inelastic peaks as a function of the target mass A in the reaction of different Sn beams at 1GeV.*

of target mass. This fact is a signature that the baryon resonance production increments the total cross section of charge exchange reaction with the increment of target mass.

4.2.3 Results

Charge-exchange reactions induced by secondary beams of ^{122}Sn, ^{120}Sn and ^{110}Sn produced by fragmenting ^{124}Sn and ^{112}Sn projectiles were also investigated in this work. The secondary beams were produced in a 4 g/cm^2 beryllium target placed at the entrance of the FRS. The first half of the spectrometer was used to separate and identify the secondary beams. Charge-exchange reactions of these secondary projectiles was induced in C targets (1.4 and 0.92 g/cm^2) located at the intermediate image plane of the spec-

trometer. The final reaction residues were then identified with the second section of the spectrometer.

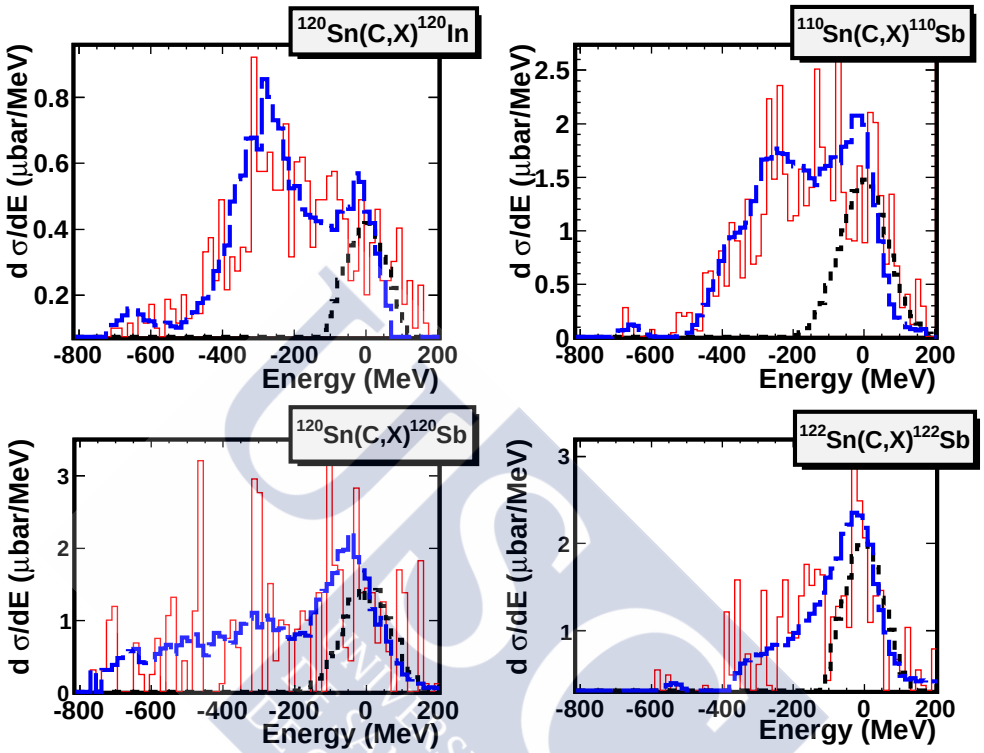

Figure 4.11: *Energy recoil distributions (Solid line) in the beam particle reference using Sn secondary beams at 1GeV (dotted line) on Carbon target. The dashed line corresponds to the unfolding distributions in the two step experimental set up. It is possible check that in this case the result is affected by the statistic fluctuations and the thickness of target.*

In this case the longitudinal momentum of the projectile residues was determined taking into account their positions at the intermediate and final image planes and the dispersion in the second section of the spectrometer according to the equation 2.10.

The measurements with secondary beams suffer from the much lower intensities. To compensate this drawback thicker reaction targets are required resulting in a poorer momentum resolution as discussed in section 3.2 . A clear example is shown in Fig. 4.11 where we display the missing energy spectra (histograms) of several charge-exchange projectile residues produced at the intermediate image plane of the spectrometer by secondary projectiles.

These spectra were obtained from measurements of the corresponding longitudinal momenta at the final image plane of the spectrometer as previously explained.

Fig. 4.11 evidences the poor resolution of these measurements since the double structure corresponding to the elastic and inelastic charge-exchange channels can not be identified. By unfolding the response function of the experimental setup one improves the resolution (solid lines) but not at the level of the measurements performed with primary projectiles and thin targets.

These measurements demonstrate that the target thickness and the statistics are important factors in order to obtain optimal spectrum measurements. Future experiments using secondary beams will require take into account these experimental factors.

Using the method described in the section 3.6 it is also possible to determine the charge-exchange cross sections with unstable beams impinging on carbon target with a thickness of 1.4 g/cm^2 of thickness placed at the intermediate focal plane S2 of the spectrometer. The results are summarized in table 4.2.

Secondary Beam	Reaction Product	Cross section (mb)	Uncertainty
^{120}Sn	^{120}Sb	0.79 ± 0.17	6.76
^{122}Sn	^{122}Sb	0.76 ± 0.19	5.71
^{110}Sn	^{110}Sb	0.75 ± 0.17	5.27
^{120}Sn	^{120}In	0.29 ± 0.07	7.93

Table 4.2: *Measured charge exchange reaction cross sections using unstable beams at* $1GeV/u$

The results are compatible with the cross section obtained when a stable beam was impinging a target at S0. Again, the difference between the cross section value of Sb (np channel) is higher than In (pn) cross section value which indicated the strong dependence of the cross section with the content of proton and neutrons in the nucleus of target.

4.3 Sensitivity to the radial distributions of proton and neutrons

As previously discussed, the isobaric character of the charge-exchange reactions investigated in this work represents an important selection in impact parameter. The strong absorption characterizing the nuclear interaction

at relativistic energies and the propagation of pions in the nuclear medium guarantee the peripheral nature of this reactions. Moreover, the possibility of measuring both charge-exchange channels in the same experiment may give access to the relative content of protons and neutrons at the nucleus surface.

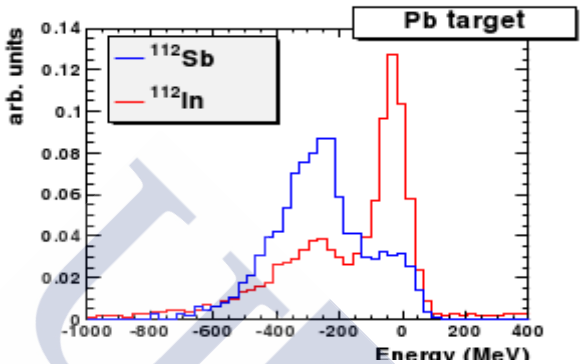

Figure 4.12: *Comparison between the np (^{112}Sb) and pn(^{112}In) energy distributions.*

The interaction probability in the case of n-p channel decrease with the mass number (A) and in the p-n process it occurs the in inverse behavior. In this case the probability grows with the mass number (A). This process is explained in the diagram 1.2 where the p-n process is sensible to the neutron content, i.e. in the case of lead target it is a neutron reach nuclei and the probability of interaction grows with respect to the n-p process. In this case this reaction is sensitive to the proton number in the nuclei. The future analysis of the theoretical result of the inelastic region in the Sn interactions will give us a possibility of determinate the r.m.s proton and radii of nuclei as suggests the reference [30].

In the inelastic channel it is more sensible to the target mass dependence. It is clear that the inelastic cross section it is more sensible to the proton an netron number in the projectile and the target. With the difference between the projectile nucleon in the projectile we observe by direct comparison the change cross section in the ^{112}Sn and ^{124}Sn. For example in the figure 4.12, when we compare the projectile reactions with p-n and n-p channels we notice the n-p quasielastic peak is lower that p-n channel. The reason is that the Pb target is a reach neutron nucleus and it has fewer proton interaction with the projectile. This fact is a signature that the charge exchange reactions are sensibles to the nucleons quantity in the periphery where the nuclear density is low.

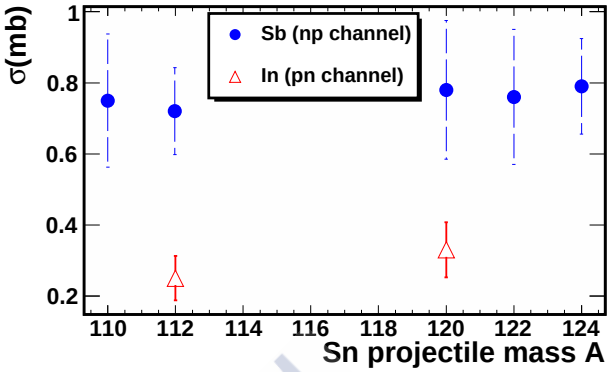

Figure 4.13: *Cross section of the Sb (np channel) and In (pn channel) produced by the Sn beams reaction on carbon target as a function of the target mass.*

Figure 4.13 shows a clear difference between total cross section the Sb and In production in the reaction of the different Sn projectiles on carbon target. The average ratio between this cross sections is around $R_{\frac{np}{pn}} = 2.4$. This fact reveal again the sensibility that the charge exchange reaction to the proton and neutron content in the nucleus. Moreover, a plausible hypothesis is to observe a possible skin effect because the average value of neutron/proton ratio ~ 1.35 does not explain the $R_{\frac{np}{pn}}$ ratio. Theoretical calculations in this way will clarify this effect.

4.4 Excitation of baryon resonances in the nuclear medium

4.4.1 Evidences for the excitation of different resonances

The inelastic charge-exchange channel corresponds to nucleon excitations as Δ-resonance. In this discussion it is clear the Δ resonance peak in the inelastic region as shows the unfolded energy distribution represented in the figure 4.14. Using the unfolding technique it is possible to improve the resolution of the FRS. Additionally of disentangle the two energies regions (the quasielastic and inelastic peak), it is possible reveal additional structures in the inelastic region.

The average mean value and width of each energy components in the inelastic and quasielastic regions are physical observables which provide infor-

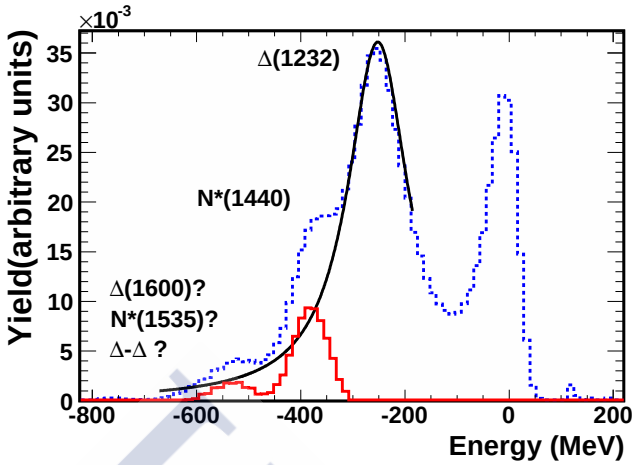

Figure 4.14: *Unfolded energy spectrum in the* $^{112}Sn(Cu,X)^{112}Sb$. *Additional resonant components in the inelastic channel are shown. The* Δ *resonance (solid line) subtraction give us and idea of additional baryon resonant (dashed line) as Roper (*$N(1440)$*) resonant. Using the techniques used in this work is not possible to describe the third peak, but it is possible that this peak correspond could be* $\Delta(1600)$, $N*(1535)$ *or a double* Δ *production (* $\Delta - \Delta$*).*

mation about the interaction and the particles that interact in the reaction. Using the mean value obtained from the fit analysis of the energy spectra it is possible calculate the estimate rest mass of each resonant in the inelastic channel. The width value of each resonant distribution give us an idea of the interaction time in the charge exchange reactions thought the uncertainty principle. Using this physical observables in order to compare the baryon behavior in nucleon-nucleon interaction and in nucleus collision give us a clear outlook of the nucleon interaction at different densities.

Fitting Procedure

The quantification of each energy peak of the reaction is important in order to understand the in-medium properties and isospin dependence of the isobaric charge-exchange reaction with heavy ions. To fulfill this objective, it is necessary to extract the mean and width in each energetic region with high accuracy. It is not easy to extract this information as it requires theoretical calculations.

We choose a method using a generalizated Breit-Wigner functions. A detailed description of this method appears in [77]. This method works with asymmetric Breit Wigner functions and it is possible to extract the fit

parameters with high accuracy. The important advantage of this method is that not *apriori* assumptions are required to understand a resonance shape.

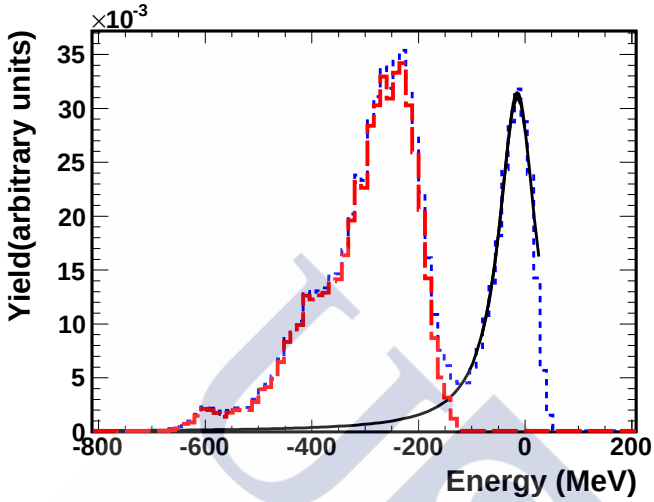

Figure 4.15: *Energy subtraction (dashed line) of the elastic region in the energy recoil nucleus spectrum (dotted line) in the reaction* $^{124}Sn(C,X)^{124}Sb$ *. The solid line indicate the elastic fit and the inelastic energy region (dashed line) is a distribution without elastic component.*

In our case, the function $f(E)$ which is called the fit function,it operates over the unfolding distribution described above. The mathematical form of the generalizated Breit-Wigner formula is written in the following equation:

$$f(E) = Acos^2(\beta + \delta) \tag{4.1}$$

with $\beta = arctan(2(E - E_0)/\Gamma)$ where E_0 and Γ are the energy mean values and width of the Breit-Wigner distribution. The A parameter is the amplitude of the distribution and δ is a parameter that makes the function fit asymmetric. When this parameter has a value $\delta = 0$ the fit distribution is a Lorentz shape function.

The equation 4.1 gives us a powerfull tool in order to investigate the Elastic and Inelastic regions. It is important to note that Elastic channel could affect the inelastic region. To substract this component first we fitted the elastic region and using the resulting fit function we can subtract the elastic component as well. Figure 4.15 represents the method of subtraction of the elastic channel with the objective to obtain the inelastic channel without elastic interference component. Using this fit function we found the results that appear in the figure 4.16 and 4.17.

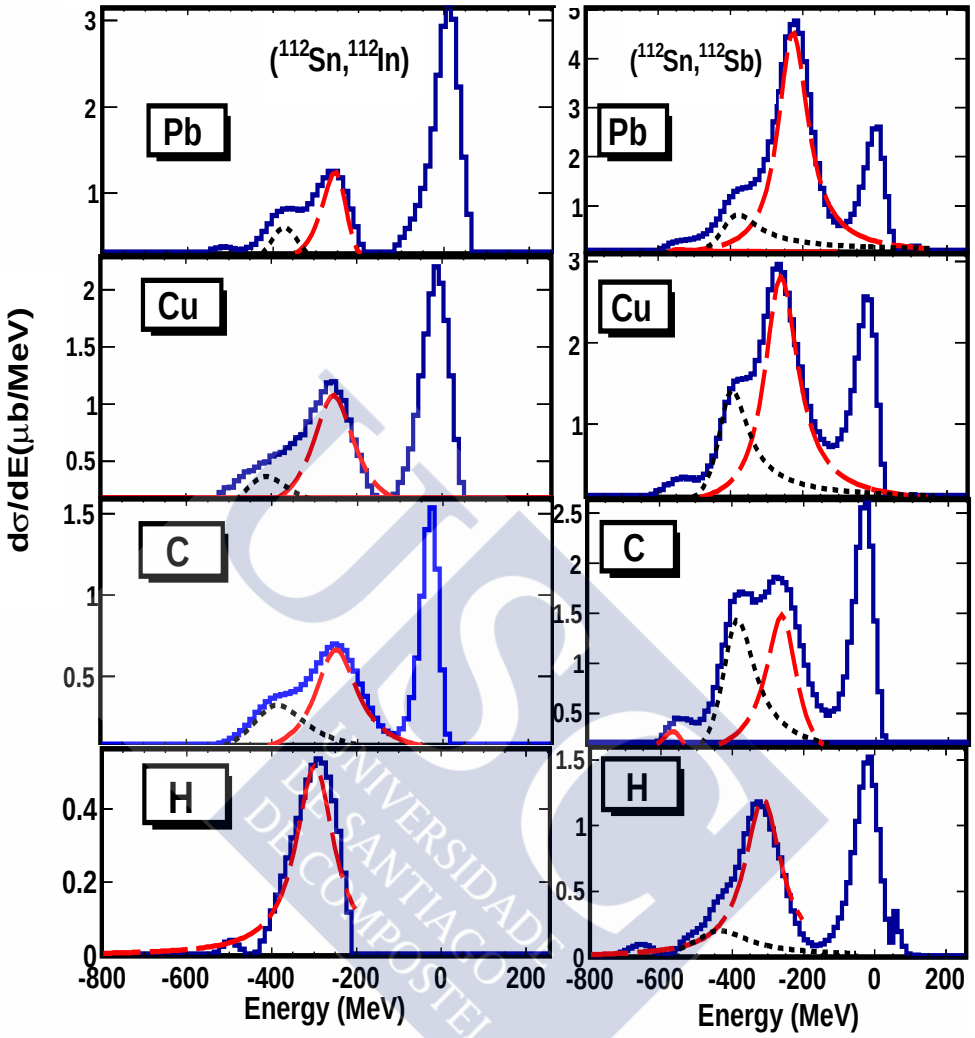

Figure 4.16: *Breit Wigner fits for ^{112}Sn charge exchange reaction products: These plots represent the recoil energy distribution (solid line) of the charge exchange reaction residues in the beam particle frame. In the inelastic above the energy pion production threshold it is possible to excite the Δ and the Roper resonances. In each plot the contribution of each resonant component is shown. The dashed line is the $\Delta-$ resonance component and the dotted line represent the Roper resonant component. The third peak contribution is almost negligible.*

At this step, we can fit the inelastic part using the combination of three generalizated Breit-Wigner functions. Each individual component is interpreted like resonant peaks. The principal component is the Δ resonant peak,

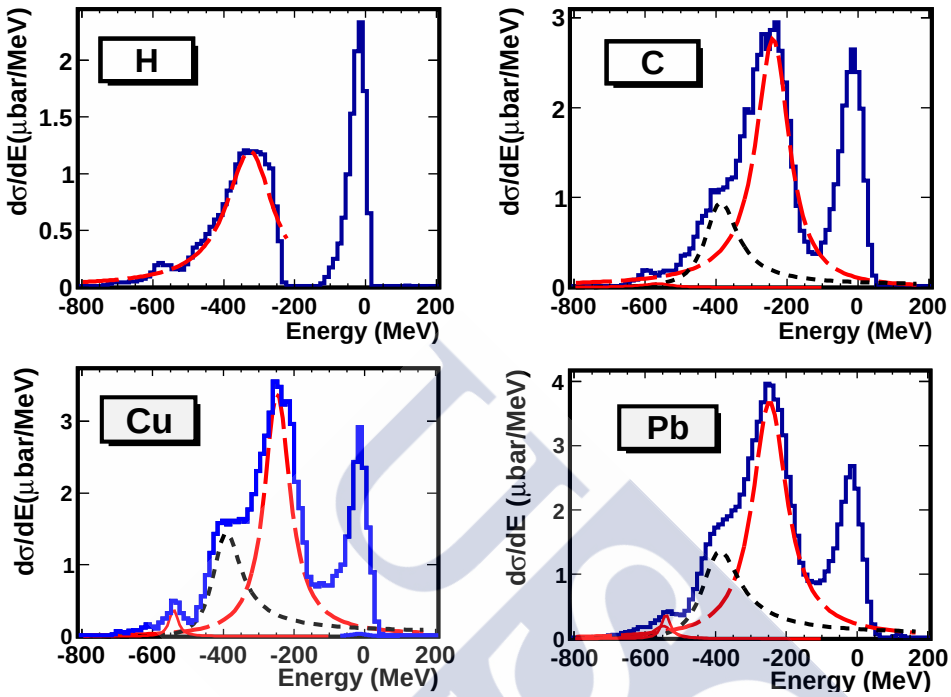

Figure 4.17: *Breit Wigner fits for n–p channel of ^{124}Sn beam : These plots represent the recoil energy distribution (solid line) of the ^{124}Sb in the beam particle frame. The dashed line is the $\Delta-$ resonance component and the dotted line represent the Roper resonant component. The third peak contribution is almost negligible.*

the next component is understood like the Roper resonant and the third component could be a double Δ resonant production or another resonant close to the roper resonant i.g. $\Delta(1600)$. The table 4.3 summarize the fit parameters using the fit function $f(E)$ (equation 4.1) obtained from the energy distributions 4.16 and 4.17.

Resonance	$E_0(MeV)$	$\Gamma(MeV)$	**A**	δ
$^{124}Sn(H,X)^{124}Sb$				
Δ	-320±23	131±26	1.19	0.03
$^{124}Sn(C,X)^{124}Sb$				
Δ	-238±24	112± 25	0.03	0.35
Roper	-393±30	110± 25	0.01	-0.11
The 3rd peak	-599±40	67±18	0.0015	0.087
$^{124}Sn(Cu,X)^{124}Sb$				
Δ	-245±23	110±25	0.041	-0.018
Roper	-407±43	95± 22	0.017	-0.19
The 3rd peak	-538±79	35±10	0.005	-0.094
$^{124}Sn(Pb,X)^{124}Sb$				
Δ	-248±27	92±22	0.045	-0.0014
Roper	-391±38	123± 28	0.0179	-0.1336
The 3rd peak	-548±82	43±10	0.0022	-0.086
$^{112}Sn(H,X)^{112}Sb$				
Δ	-314±26	124± 29	1.200	0.0001
$^{112}Sn(C,X)^{112}Sb$				
Δ	-257± 23	104±22	0.0179	0.083
Roper	-389±58	109± 25	0.0174	-0.172
The 3rd peak	-555 ±83	86±20	0.0038	0.185
$^{112}Sn(Cu,X)^{112}Sb$				
Δ	-247±22	110± 25	0.041	-0.0176
Roper	-407±43	95± 22	0.0164	-0.194
The 3rd peak	-538±81	35 ±10	0.0047	-0.094
$^{112}Sn(Pb,X)^{112}Sb$				
Δ	-239± 21	119± 27	5.05984	1.18e-01
Roper	-389±37	76± 18	0.0094	-0.526
The 3rd peak	-559 ±84	54±12	-0.031	-0.523641
$^{112}Sn(H,X)^{112}In$				
Δ	-298±27	109±25	0.52	0.0002
$^{112}Sn(C,X)^{112}In$				
Δ	-240±22	128± 28	6.97311e-01	1.05032e-01
Roper	-404±36	123± 28	0.202733	-7.36053e-02
The 3rd peak	-567±65	74± 17	0.066	2.36420e-02
$^{112}Sn(Cu,X)^{112}In$				
Δ	256± 23	136± 31	0.0130	-0.0175
Roper	-427 ±40	145± 33	0.00440	-0.1939
The 3rd peak	-580±54	105 ± 16	0.0011	-0.094
$^{112}Sn(Pb,X)^{112}In$				
Δ	-250±23	95±22	0.0152	0.1406
Roper	-386±35	103± 24	0.00729349	-0.0249
The 3rd peak	-535±56	63±16	0.0031	-0.193

Table 4.3: *Breit-Wigner Fit parameters of the charge exchange reactions products*

Energy and target dependences

The inelastic part of the recoiling energy distribution must be more sensitive to the energy changes due to the Δ resonance nature.

The cross section at inelastic region in the energy recoil distribution is dominated by the Δ resonance excitation principally, thus the nucleon-nucleon cross section behavior should explain the evolution of the charge-exchange process at hight energy above $\Delta-$ resonance production. One of the principal effects in the inelastic region is the increase of the inelastic channel with the energy. As the energy grows it is possible to excite the Δ resonance with more probability as it is observed in the figure 4.18. This effect is explained by the nucleon excitation. Figure 4.18 represent the total cross section of the n-p channel in nucleon nucleon collision [31] with the contribution of both channels and, thus with the increase of the energy the inelastic channel grows from 300 MeV. At low energies, below the threshold energy of 300 MeV the unique contribution is the elastic, over the energy of production of the resonance Δ the probability of realizing a charge exchange reaction across the inelastic channel grows when the energy of production of the Δ resonance is above the pion production threshold energy.

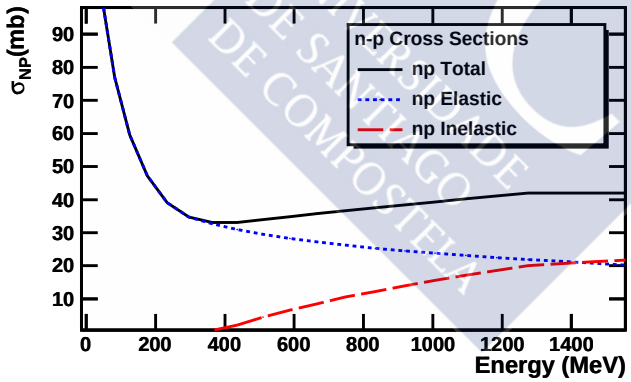

Figure 4.18: *Total Cross section(solid line) as a function of the energy in the n-p scattering. The elastic (dotted line) and inelastic (dashed line) are nucleon-nucleon cross sections according to the Cugnon parameterization [31]*

In the figure B.4 it is clear that besides Δ resonance in the 1 GeV spectrum, there exists another resonances which are at high energies above 300 MeV, this resonance correspond with $N(1440)$, and in some spectra (see for example the figure 4.16).

The contribution of the $\Delta-$resonance change with the energy. At 700

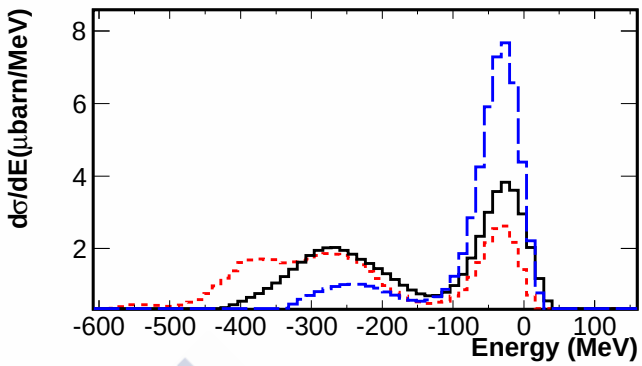

Figure 4.19: *Energy dependence of the inelastic channel in the reaction* $^{112}Sn(C,X)^{112}Sb$*: The charge exchange reactions at 400 MeV (black line), 700 MeV (blue line) and the 1GeV (red line) in the beam particle frame.*

MeV the $\Delta-$cross section probability is almost the same that the 1 GeV case but the contribution of the roper resonance is negligible (see figure 4.20).

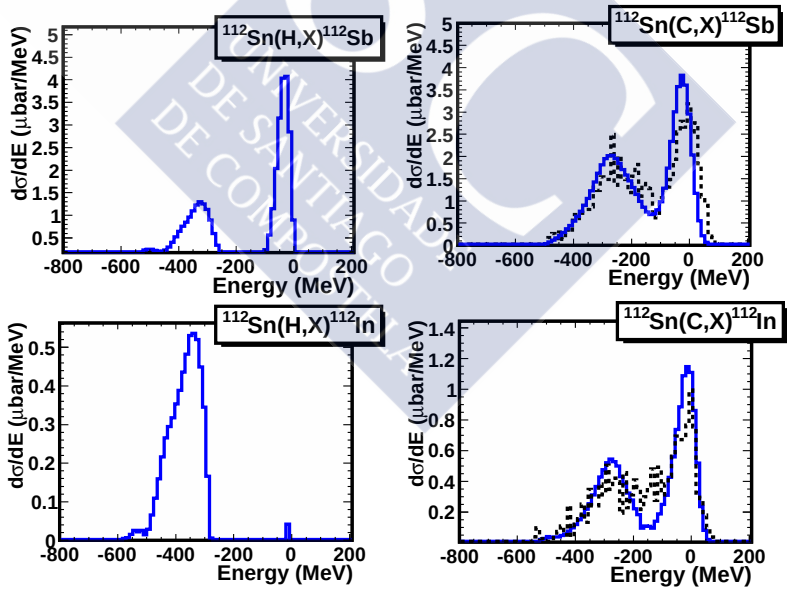

Figure 4.20: *Energy Distributions of* ^{112}Sb *and* ^{112}In *at 700 MeV (dotted line) and its respective deconvolution (blue line). In the case of the proton target only the unfolding subtraction appear.*

At 400 MeV (see figure 4.21) it is only possible to excite the $\Delta-$resonance but the cross section of the $\Delta-$resonant production is lower than other en-

ergies. In this case the quasielastic component is dominant.

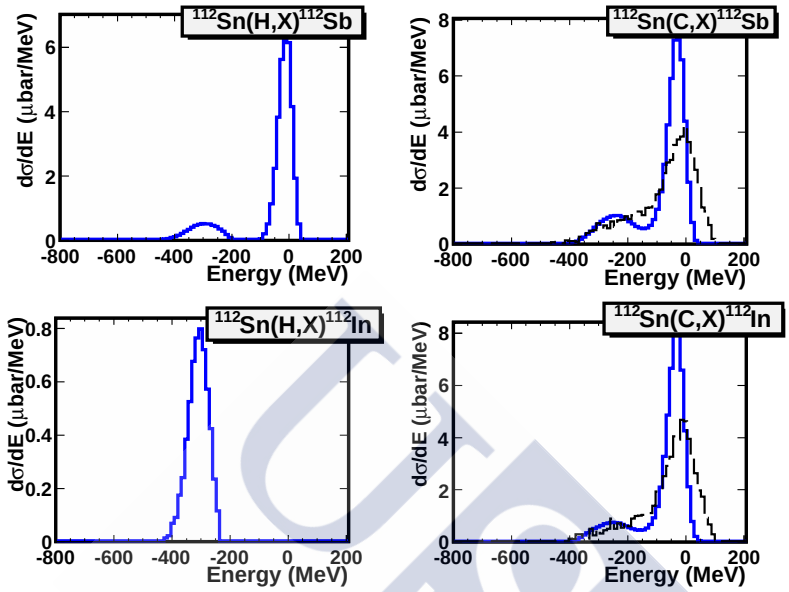

Figure 4.21: *Energy Distributions of ^{112}Sb and ^{112}In at 400 MeV(dashed line) and its respective deconvolution (solid line). In the case of the proton target only the unfolding subtraction appear.*

Dependence with the projectile

In order to evaluate the possible dependence of the Δ resonace formation with the projectile, we used the same target and change the projectile. In this way it is possible to check the possible isospin dependence with the projectile.

Figure 4.22 shows the energy distributions for different Sn projectiles and it is clear that each distributions present Δ and N(1440) resonace peaks contributions. In the case of ^{112}Sb, the relative Roper production is higher than others cases. Futhermore, the third peak present a shift in the mean value of energy.

Energy shift

The investigation of the Δ-resonance excitation in (p,n) and (3He,t) charge-exchange reactions has revealed how this process is affected by nuclear in-medium effects. The main observation is a downward energy shift of

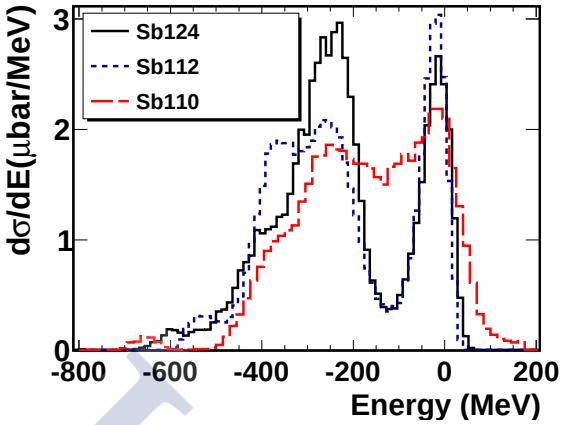

Figure 4.22: *Dependence of the inelastic region with the projectile isospin for the different Sb residues produced in the np reaction of the* $^{124,112,110}Sn$ *beams that impinging on carbon target at 1GeV.*

the Δ-resonance peak position by around 70 MeV when using heavy targets ($A > 10$) as compared to the mean energy of the Δ resonance produced in free nucleon–nucleon collisions. Further experiments investigating the D-resonance excitation in charge-exchange reactions using heavy ion collisions also have shown a clear dependence of the magnitude of the downward energy shift in the Δ resonance with the mass of the target nucleus.

The Δ energy in nuclei as observed in charge exchange reactions is lower than that on proton target as appear for example in the reference [38] and references therein. This effect was observed in previous experiments. The direct comparison with the proton result it is possible to observe the Δ− resonance shift see for example the left panel of the figure 4.6 This energy shift which is a clear example of the in-medium nuclear effects in the Δ−resonance formation. In the figure (see fig. 4.23) shows this effect observed in our experimental data. It is a proof that the hadronic particles are sensible to the isovector nuclear component. In others experiments using different probes ([38]) such as leptonic and electromagnetic probes this shift was not observed with the probes, so this fact shows that the hadron probes are sensible to the isovector component of the nuclear force. For this reason , when we used the hadron projectile we could obtain an excellent tool to understand the nuclear force.

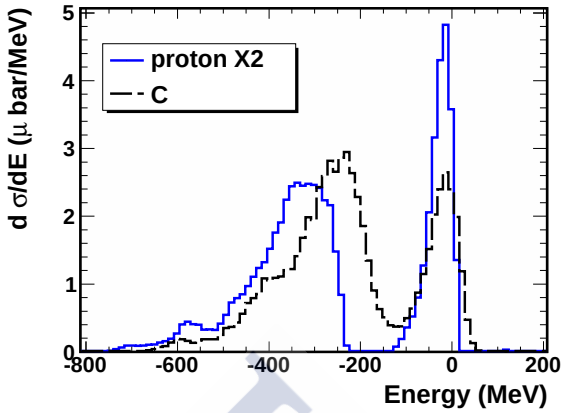

Figure 4.23: *Energy distributions of the ^{124}Sb in the reaction of ^{124}Sn beam impinging on proton and carbon target at 1GeV. We can observe the energy shift of the $\Delta-$resonant peak produced in the carbon target (dashed line) with respect to $\Delta-$resonant production at proton target (solid line). The value of this shift is around $\sim$ 70 MeV.*

4.4.2 Model Calculations

Several models based in isobar-hole assumptions (see *e.g.,* Ref. [39] and references therein) have been used to interpret the charge exchange reactions as well as the production of the Δ and other nucleonic resonances. In this section we briefly present the preliminary calculations made by Vidaña [78] used in this thesis to analyze the experimental results obtained. According to this model, quasi-elastic and inelastic processes are described in terms of a exchange of a virtual pion between the interacting nucleons. The effect of short range correlations is also included in the case of the quasi-elastic processes by means of the well-known Landau-Migdal parameter g'. In the inelastic case the excitation of the Δ and N^* resonances is considered both in the target and in the projectile. The basic ingredients to compute the cross sections of these elementary reactions are the $NN\pi$, $N\Delta\pi$ and $NN^*\pi$ vertices which in the present model.

The cross section for a charge-exchange (^ZA, $^{Z\pm1}A$) reaction is calculated using the following equation:

$$\frac{d^2\sigma}{dE_{ejectile}d\Omega_{ejectile}} = \frac{d^2\sigma}{dE_3 d\Omega_3} \times |F(q)|^2 \times S_P \times P_{abs} \ . \qquad (4.2)$$

The cross section for a charge-exchange (^ZA, $^{Z\pm1}A$) reaction is calculated here in an approximate form as the product of the elementary process cross

section, a projectile-ejectile transition form factor ($|F(q)|^2$) that takes into account the spatial extension of the nucleons in the projectile/ejectile nucleus, and a survival probability S_P that accounts for the fact that when nuclei interpenetrate many, less energetic, collisions will take place between the nucleons and degrade the initial available energy. In the case of the inelastic processes should be included also a factor that takes into account the reduction of the cross section if the pion produced in the reaction is absorbed P_{abs} .

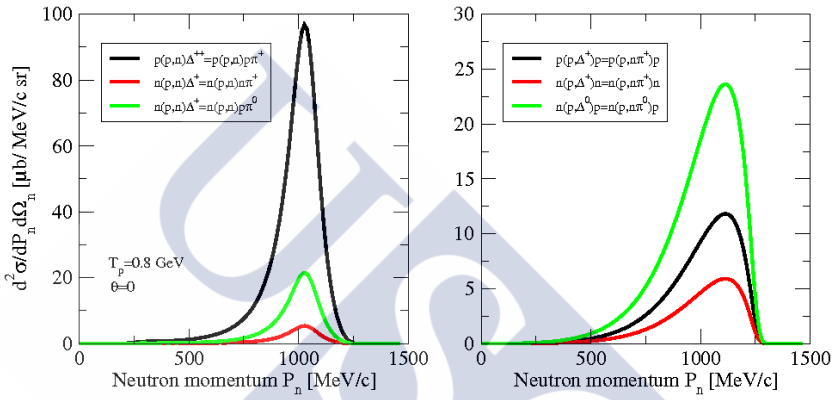

Figure 4.24: *Contributions of the Δ excitation to the total double differential cross section of the elementary charge-exchange (p,n) reaction [78]. Left panel shows the Δ− excitation in the target and right panel Δ− excitation in the projectile*

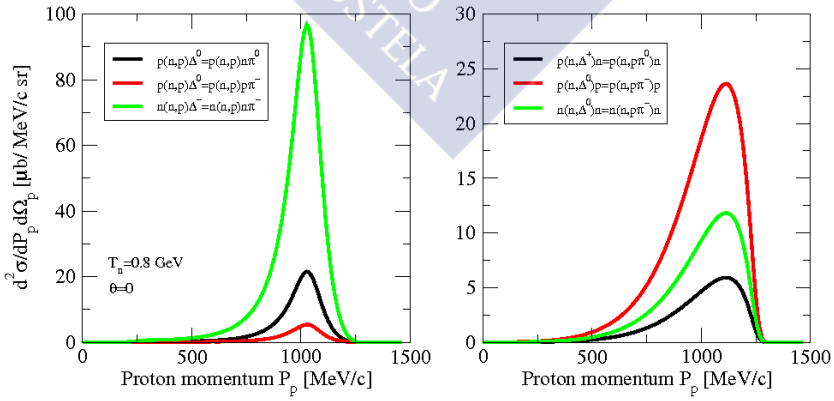

Figure 4.25: *Contributions of the Δ excitation to the total double differential cross section of the elementary charge-exchange (n,p) reaction [78]. Left panel shows the Δ− excitation in the target and right panel Δ− excitation in the projectile*

Excitation in the Target	I.C.	Excitation in the Projectile	I.C.
$\Delta(1232)$			
$p(n,p)\Delta^0 = p(n,p)n\pi^0$	2/3	$p(n,\Delta^0)p = p(n,p\pi^-)p$	$\sqrt{(2)}/3$
$p(n,p)\Delta^0 = p(n,p)p\pi^-$	$\sqrt{(2)}/3$	$p(n,\Delta^+)n = p(n,p\pi^0)n$	-2/3
$n(n,p)\Delta^- = n(n,p)n\pi^-$	$\sqrt{(2)}$	$n(n,\Delta^0)n = n(n,n\pi^-)n$	$-\sqrt{(2)}/3$
Roper $N^*(1440)$			
$p(n,p)P_{11}^0 = p(n,p)n\pi^0$	-2	$p(n,P_{11}^0)p = p(n,p\pi^-)p$	$-\sqrt{(2)}$
$p(n,p)P_{11}^0 = p(n,p)p\pi^-$	$2\sqrt{(2)}$	$p(n,P_{11}^+)n = p(n,p\pi^0)n$	-2
——	—	$n(n,P_{11}^0)n = n(n,p\pi^-)n$	$\sqrt{(2)}$

Table 4.4: *Elementary process for the Δ resonance and Roper produced in (n,p) reaction and its respective isospin coefficients I.C.*

Excitation in the Target	I.C.	Excitation in the Projectile	I.C.
$\Delta(1232)$			
$p(p,n)\Delta^{++} = p(p,n)p\pi^+$	$\sqrt{(2)}$	$p(p,\Delta^+)p = p(p,n\pi^+)p$	$-\sqrt{(2)}/3$
$n(p,n)\Delta^+ = n(p,n)n\pi^+$	$\sqrt{(2)}/3$	$n(p,\Delta^+)n = n(p,n\pi^+)n$	$\sqrt{(2)}/3$
$n(p,n)\Delta^+ = n(p,n)n\pi^0$	-2/3	$n(p,\Delta^0)p = n(p,n\pi^0)p$	2/3
Roper $N^*(1440)$			
$n(p,n)P_{11}^+ = n(p,n)n\pi^+$	$-2\sqrt{(2)}$	$p(p,P_{11}^+)p = p(p,n\pi^+)p$	$-\sqrt{(2)}$
$n(p,n)P_{11}^+ = n(p,n)p\pi^0$	-2	$n(p,P_{11}^+)n = n(p,n\pi^+)n$	$\sqrt{(2)}$
——	—	$n(p,P_{11}^0)p = n(p,n\pi^0)p$	-2

Table 4.5: *Elementary process for the Δ resonance and Roper produced in (p,n) reaction and its respective isospin coefficients I.C.*

We end this section by showing in Figs. 4.24 and 4.25 the contributions of the Δ excitations to the total double differential cross section of the elementary charge-exchange (p,n) and (n,p) reactions. Similar calculation was made for the Roper resonance but is not presented in this discussion. The relative weight of the different processes can be easily understood by looking at their isospin factors of the given in Tables 4.5 and 4.4. It is also interesting to note that the shape and the position of the resonance is more symmetric and close to the value of its rest mass when it is excited by means of the process shown in Fig. 4.5 (left panel). On the other hand when the excitation mechanism is that of Fig. 4.5(right panel) the shape of the resonance becomes asymmetric and its position is shifted. This is a kinematical effect related with the different values of the resonance invariant mass calculated in the target or in the projectile.

4.4.3 In-medium production of the Δ resonance

Using the deconvolution method it is possible to disentangle the Δ resonance contribution clearly . The figure 4.26 shows the behavior of the Δ−resonance production as a function of the target mass (A). It is clear that the Δ−resonance cross section is increased when the number of nucleons, and the difference between the np and pn channel is that each channel is sensitive to the number of nucleons in the nuclear periphery.

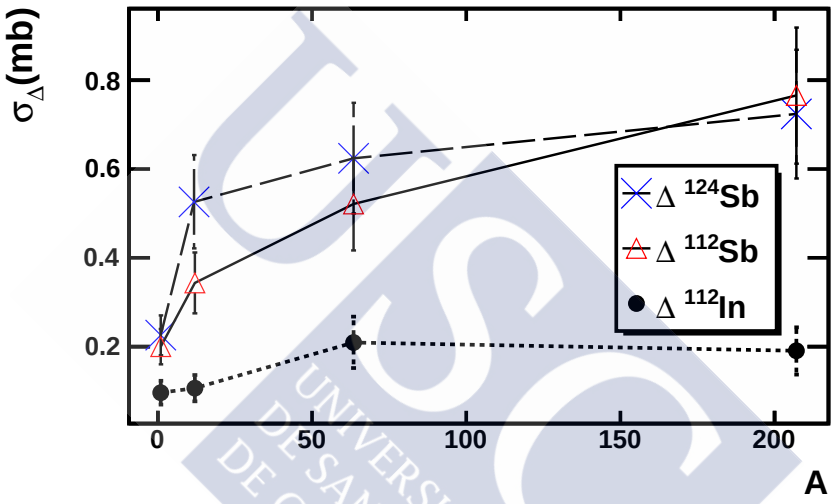

Figure 4.26: *Δ−resonance cross section as a function of the target mass (A). The cross section in the case of the n-p channel is bigger than p-n channel. Each component grows with the nucleon content in the periphery.*

The inelastic peak appears above Δ energy production threshold at 300 MeV. At this energies the production probability of inelastic peak grows with the energy beam. The quantification of each energy peak of the reaction is important in order to understand the in medium properties and isospin dependence of the isobaric charge-exchange reaction with heavy ions.

Comparison with previous results

The Δ resonace parameters is a important tool and the key in order to understand the baryon resonances in the nuclear medium. Table 4.6 shows a comparison with the previous experimental results .

By direct comparison of the 4.7 with the results of the Δ− resonace fit values obtained in this work (table 4.3) it is possible to check that energy

Mass(MeV)	Width(MeV)	Reaction	Data Reference
1231 to 1233 ($\approx$ 1232)	116 to 120 ($\approx$ 118)	N-N (free case)	PDG. [47]
1229 $\pm$6	87$\pm$7	C-C at 4.2 GeV/c	D. Krpić *et al.* [79]

Table 4.6: *Experimental values for the mass and width values for the Δ resonance.*

shift in the mean value. In the free case the Δ resonance mass have a value of (1232 MeV) that is equivalent to -300 MeV in the missing energy spectrum. In Our case we observed a the clear Δ resonance mass shift around $\sim$ 70 MeV. In the case of the Δ width value results it is possible to observe that this value it is more or less the same that the free case around $\sim$ 115 MeV (within the error limits).

4.4.4 In-medium production of the Roper resonance

Figure 4.27 shows the Δ resonant peak as a prominent component in the missing energy, but it is possible to observe a additional component: the Roper (N(1440)) resonant. This component is independent of the binning variation that proves that is not a mathematical artefact.

Figure 4.29 shows the $N(1440)$ resonance cross section as a function of the target mass (A). The cross section in the case of the n-p channel is bigger than p-n channel. Each component grows with the nucleon content in the periphery. Using the results in the figures 4.27 and 4.28 it is possible to assure that the other resonances are sensible at target mass and consequently the nucleon content is described in the nucleus. A theoretical description of this behavior require a detailed study of the fundamental interaction in order to understand the meson interaction and the probability of excitation of each resonant.

Figure 4.30 represents the deconvolution of ^{110}Sb and ^{120}In spectra, in each case it is possible to separate the inelastic and quasielastic peaks but it is more complicated to disentangle the roper resonant.

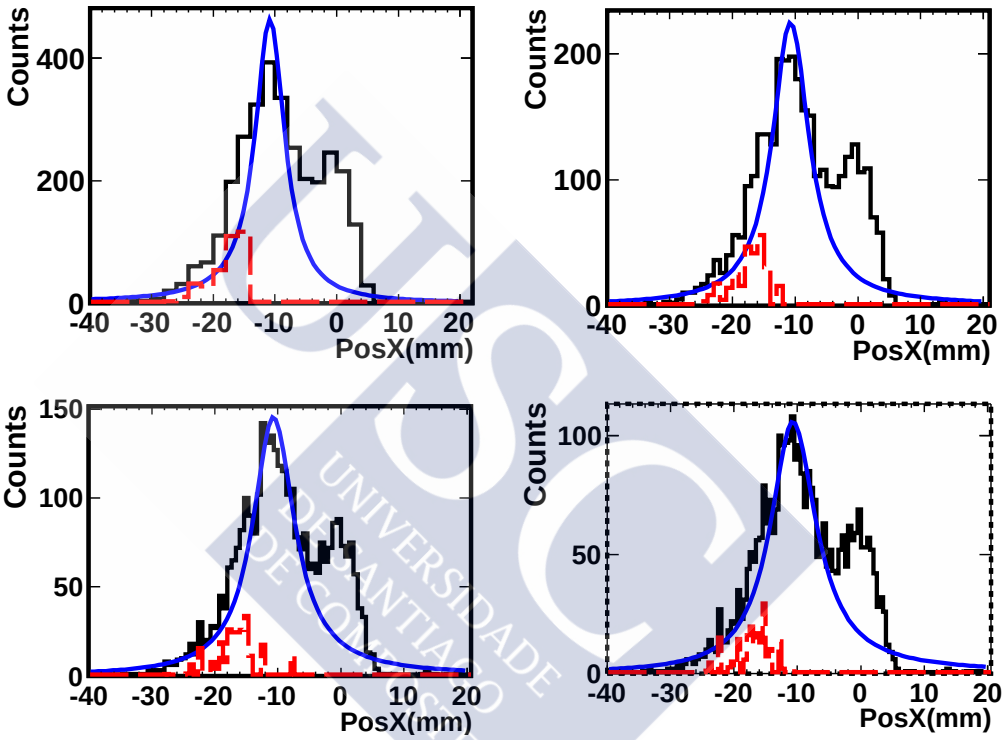

Figure 4.27: *Binning dependence of the charge exchange reaction energy distribution in the position picture. In the inelastic peak it is possible disentangle the Roper resonance (dashed line) subtracted the Δ resonance (solid line) contribution with a Breit-Wigner fit. The result is independent from the binning (Nb). In this case the left top plot is the energy spectra at Nb=100, the right-top plot Nb=200 and the following plots are Nb=300 and Nb=400 respectively.*

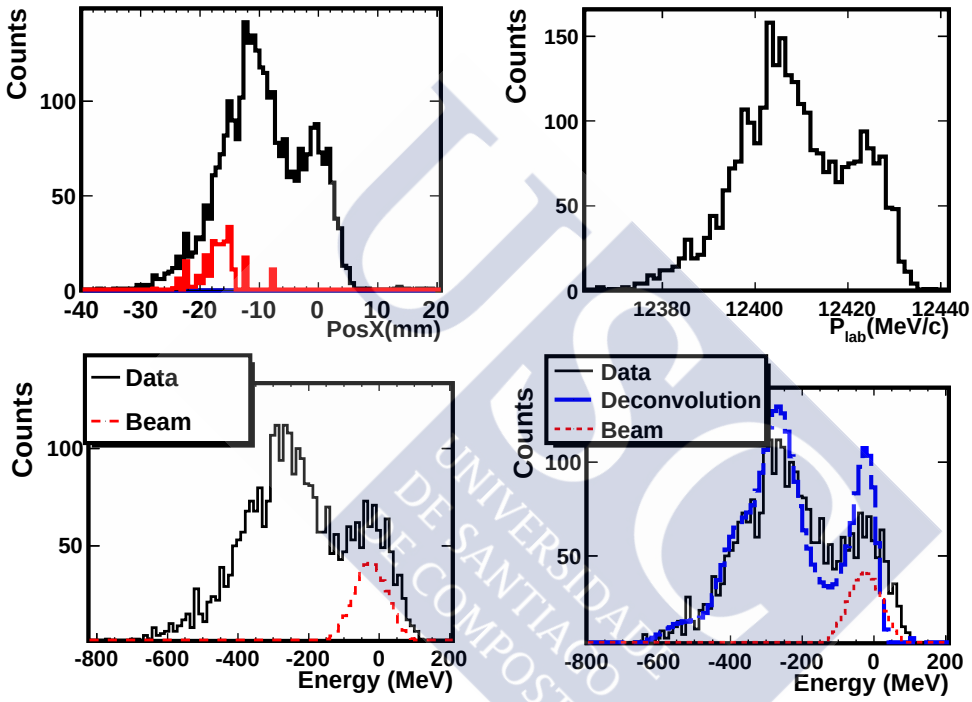

Figure 4.28: *Spectrum of ^{112}Sb using different physical pictures in the reaction $^{112}Sn(Cu,X)^{112}Sb$ at 1GeV. At left top represent the elastic and quasielastic peaks and the the roper (N(1440)) resonant in position (red line), the right-top figure the $112Sb$ spectrum in momentum representation. At left-low plot shows the beam and the energy distribution in the beam particle frame. The right-low plot shows the unfolding procedure (dashed line) in the beam particle frame.*

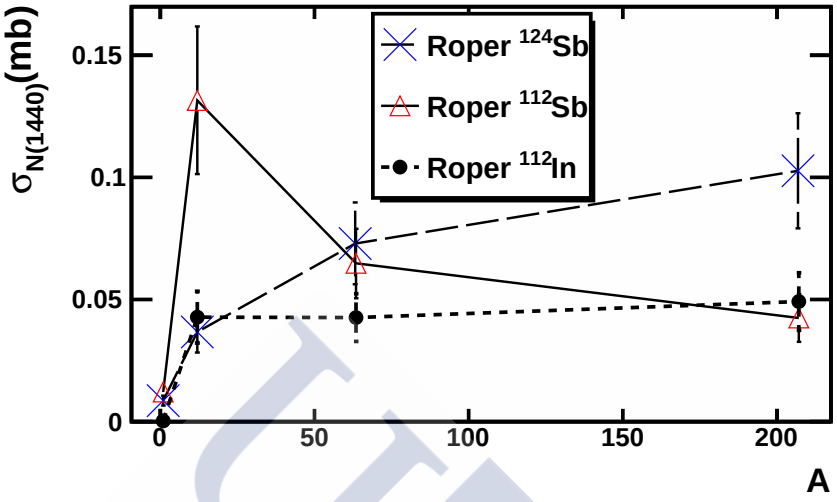

Figure 4.29: *Roper resonance cross section as a function of the target mass (A). The cross section in the case of the n-p channel is bigger than p-n channel. Each component grows with the nucleon content in the periphery.*

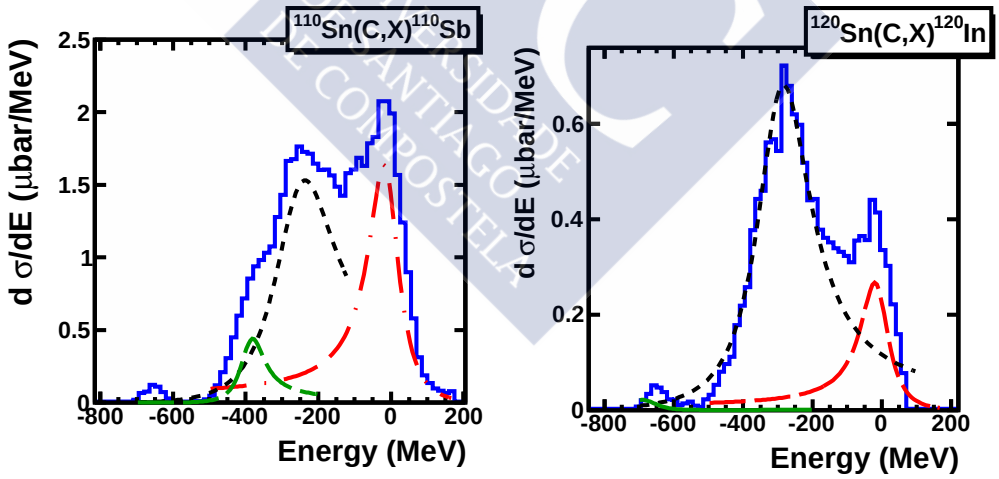

Figure 4.30: *Fit of Unfolding distributions in the two step part . Left panel correspond to the ^{110}Sb production , in this case it is possible identify the quasi elastic channel (dash-dotted line), the Δ resonant (dotted line) and the Roper resonant (dashed line) and the total unfolding (solid line). In the case of ^{120}In the Roper is not appear, and the Δ resonance. The ^{120}Sb and ^{122}Sb do not appear because low statistics counts*

Comparison with previous results

The systematical study of the Roper resonant is complemented by the heavy ion data. The experimental data using heavy ions is scare and for this reason the data that privides this work shed light on the Roper resonant production in heavy ions. Figure 4.31 shows the N(1440) contribution in the inleastic reaction $\alpha(p,X)\alpha'$ at 4.2 GeV. The results obtained by $\alpha + p$ reaction [80] and its comparison with the C+C colissions at 4.2 GeV/c [81] per nucleon demostrate that witdth of N(1440) decrease in presence of the nuclear medium.

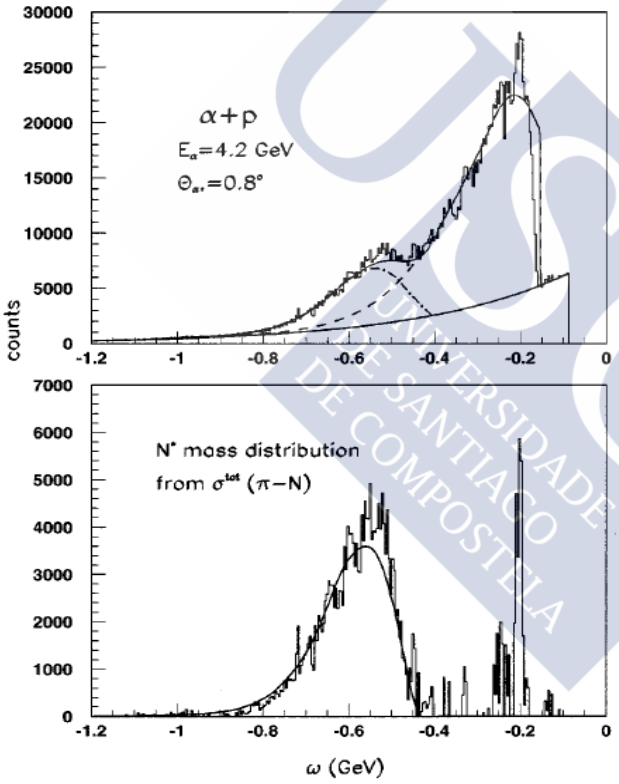

Figure 4.31: *Missing energy spectra of the reaction $\alpha(p,X)\alpha'$ at 4.2 GeV. It is clear the Roper P_{11} contribution in this inelastic reaction [80].*

Table 4.7 summarize the width and mean value of the N(1440) resonance for diferent experimental results. In the reference [80] present a possible ex-

Mass(MeV)	Width(MeV)	Reaction	Data Reference
1420 to 1470	200 to 450	N-N (free case)	PDG. [47]
1390 ± 20	190 ± 20	$\alpha + p$ at 4.2 GeV	Morsh and P. Zurpranski [80]
1480 ± 30	380 ± 50	$\alpha + p$ at 4.2 GeV	Morsh and P. Zurpranski [80]
1380 ± 10	130 ± 20	C+C at 4.2 GeV/c^2	D. Krpić *et al.* [81]
1420 ± 10	105 ± 15	C+C at 4.2 GeV/c^2	D. Krpić *et al.* [81]
1374 ± 30	110± 25	$^{124}Sn(C,X)^{124}Sb$	This work
1409± 43	95± 22	$^{124}Sn(Cu,X)^{124}Sb$	This work
1393± 38	123± 28	$^{124}Sn(Pb,X)^{124}Sb$	This work
1391±58	109± 25	$^{112}Sn(C,X)^{112}Sb$	This work
1409± 43	95± 22	$^{112}Sn(Cu,X)^{112}Sb$	This work
1390±37	76± 18	$^{112}Sn(Pb,X)^{112}Sb$	This work
1405± 36	123±28	$^{112}Sn(C,X)^{112}In$	This work
1426± 40	145± 33	$^{112}Sn(Cu,X)^{112}In$	This work
1387± 35	103± 24	$^{112}Sn(Pb,X)^{112}In$	This work

Table 4.7: *Experimental values for the mass and width values for the Roper resonance.*

planation of the difference between Roper widths this fact is not understood in the simple valence quark mode. Futhermore, it is clear that the results obtained in this work shows Roper widths in the same magnitude order the C+C colissions, that shows the appreciable difference wiyh respect to the free case. The mena value is similar to the non free collisions

Third resonance

The third peak that appear in the unfolding results might be correspond with two options the $N(1530)$ or $\Delta(1600)$. Unfortunately we can not distinguish between these resonances only with the average value of the energy, moreover other possibility is a double $\Delta-$resonance production. Unfortunately we cannot distinguish between these two resonances only with the average value of the energy.

With the FRS is possible to disentangle the two components of the energy recoil spectrum. In the figures 4.16 and 4.17 shows a complete set of results and it is clear the charge exchange reaction in two energy regions.

Moreover its is possible to improve the spectrometer resolution using the unfolding method. With this technique was feasible to find other resonant for example the N(1440), that is complicated to observed without deconvolution method. Moreover, using fit techniques is possible estimate the the mean value and width of each resonant. By direct comparison with the nucleon-nucleon scattering is possible observe a appreciable change in the rest mass

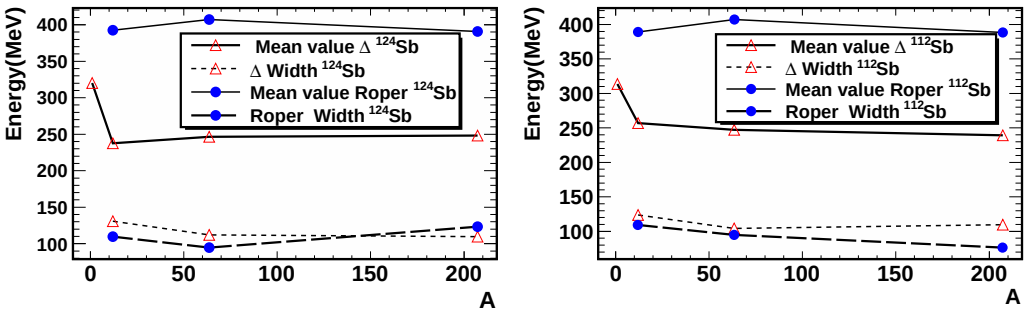

Figure 4.32: *Energy dependence of a mean value of the* $\Delta(1232)$, $N(1440)$ *and* $\Delta(1600)$ *resonances as a function of target mass. The left panel represents the results of* $^{124}Sb(target, X)^{124}Sb$ *and right panel* $^{112}Sb(target, X)^{112}Sb$. *The width of the* $\Delta-$*resonance is represented with a black solid line. The mean value and width of the* $\Delta-$*resonance is almost constant and it is clear the energy shift with respect to proton target*

formation and width of each resonant. For example the energy shift in the $\Delta-$resonance formation is almost constant around ~ 70 MeV, this fact reveal that the baryons can feel the strong force and these particles are sensible to the nuclear medium. It is important to note that this effect saturate and high atomic number (A) is independent of the target mass. The systematic analysis of the width of each it is more complicated. In the case of the Δ resonance

Figure 4.32 shows the energy dependence of a mean value of the $\Delta(1232)$, $N(1440)$ resonances and the third peak as a function of target mass. In this plot it is clear that the energy shifts with respect to proton target, and we can observe that it is almost constant in the carbon, cooper and lead targets. This fact shows a possible effect of saturation of the in-medium effect and it becomes clear that the $\Delta-$resonance width is almost constant too.

CHAPTER 5

Knockout reactions induced by Sn isotopes

In the present chapter we explore another peripheral reaction channel in relativistic heavy-ion collisions which are the projectile knockout processes. These are reactions where projectile nuclei lose few nucleons while the residual nucleus remains bound.

Knockout reactions have been largely used to investigate the structure of nuclei far from stability and their spatial distributions. The main observables used to investigate these reactions are the cross sections of this reaction channel and the longitudinal momentum distributions of the reaction residues.

In this work we take advantage of the several tin isotopes used as projectiles to systematically investigate these reactions. On top of the scan in isotopic composition of the projectiles we will investigate proton and neutron knockout and in some cases we will measure the knockout of several nucleons. With these measurements we will address several interesting issues such as the energy dissipated in peripheral fragmentation reactions, the role of nuclear excitations in nucleon knockout and the evolution of this process with the neutron excess.

5.1 Measurements

In order to cover a large range in projectile neutron excess we combined stable tin projectiles (^{112}Sn and ^{124}Sn) with secondary beams of non stable tin isotopes (^{120}Sn and ^{110}Sn) produced by fragmenting the stable ones. Therefore, the measurement of the cross-sections of neutron and proton re-

moval channels was performed by using the one and two step experimental setup explained in section 2.3.

The identification procedure follows the method presented in section 3.1. Table 5.1 summarizes the measurements done in this work.

Target Place	Beam	Target(mg/cm^2)	Fragment
S0	^{112}Sn	C(978)	$^{110}Ag, ^{109}Ag, ^{108}Ag$ ^{107}Pd , ^{106}Pd $^{106}Rh, ^{105}Rh, ^{104}Rh$
	^{112}Sn	C(100)	^{110}Cd ^{108}Ag, ^{105}Pd ^{103}Rh, ^{102}Rh
S2	^{110}Sn	C(910)	$^{109}In, ^{109}Sn$
	^{112}Sn		$^{111}In, ^{111}Sn, ^{108}Cd$
	^{120}Sn	C(1400)	$^{119}In, ^{119}Sn, ^{118}Cd$
	^{124}Sn		$^{123}In, ^{123}Sn$

Table 5.1: *List of fragments obtained by the reaction of Sn beams at C targets at 1GeV. It is important that the complete data set is a mix of the one and two steps set-up*

As can be seen in table 5.1 we could measure for all the tin isotopes used as projectiles in this work the one proton and neutron knockout channels. Moreover, for the ^{110}Sn beam we measured the two-proton removal channel and for ^{112}Sn projectiles up to the four-proton removal channel.

Other important effects that affect the identification is the charge state contribution in each MUSIC. In order to clean the identification plot it is necessary to remove the charge states using a suitable cut selected the events in the energy loss as a function of position as shown in the figure 5.1. This correction is only applied to the reactions induced at S0 . The result of this corrections is shown in the figure 5.2

In the case of identification at S4 using the two step set-up, it is necessary to identify the beam at the middle focal plane in order to select the correspondent event reactions at S4.

Table 5.2 shows the corrections factors applied to each isotope production in order to correct the production and use this value with the objective of determine the cross section. The same technique described in the chapter2 is used in order to determined the cross section of the fragmentation residues. Corrections factors such as the dead time f_d, secondary reactions f_s and $f_{ch.st}$ charge states were explained in the sections 3.5.1. Nevertheless, it

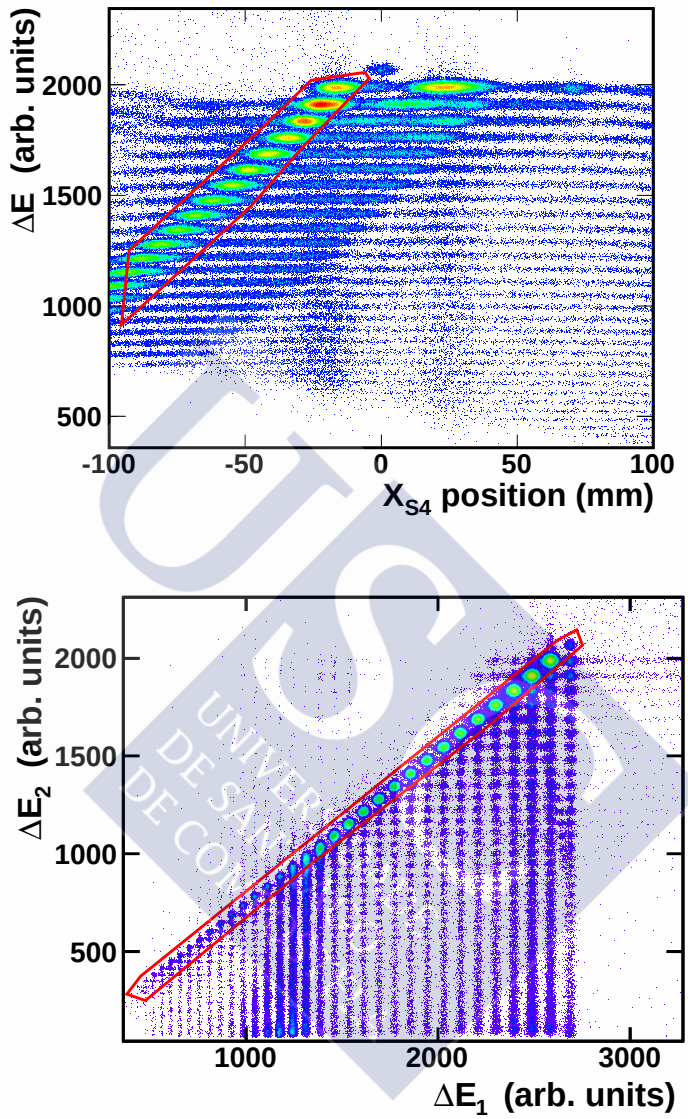

Figure 5.1: *Top Panel: Energy loss as a function of position in the final focal plane of the spectrometer. The solid line represent a charge states cut.Bottom Panel: Energy loss in each MUSIC's. In the energy loss detector at S2 (ΔE_1) it is possible to observe a blurred area, this effect due to very hight counting rate. Identification plot at the final focal plane in a setting centered in ^{112}In.*

is important to note that the selection of a specific non-centered fragment require additional correction factor depending of its *transmission*. As was

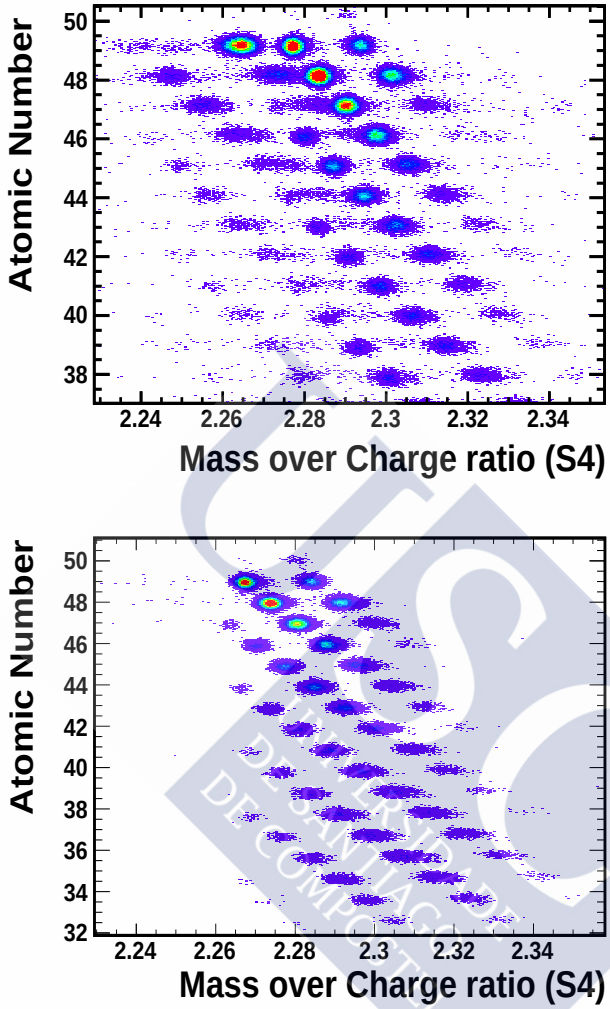

Figure 5.2: *Identification plot at the final focal plane in a setting centered in* ^{112}In *without charge states correction (top panel) and the identification plot corrected by charge states (bottom panel).*

explained in the section 2.2, the FRS have a limited momentum acceptance for this reason the complete momentum distributions, and consequently the number of total events for masses far from the centered fragment in each setting did not fully transmitted in a determined magnetic setting. The table 5.2 shows the transmition value estimation for the different settings that appear in the table 5.1. By comparison with the Mocadi and LISE codes we can associate to the transmission calculation which is 10%

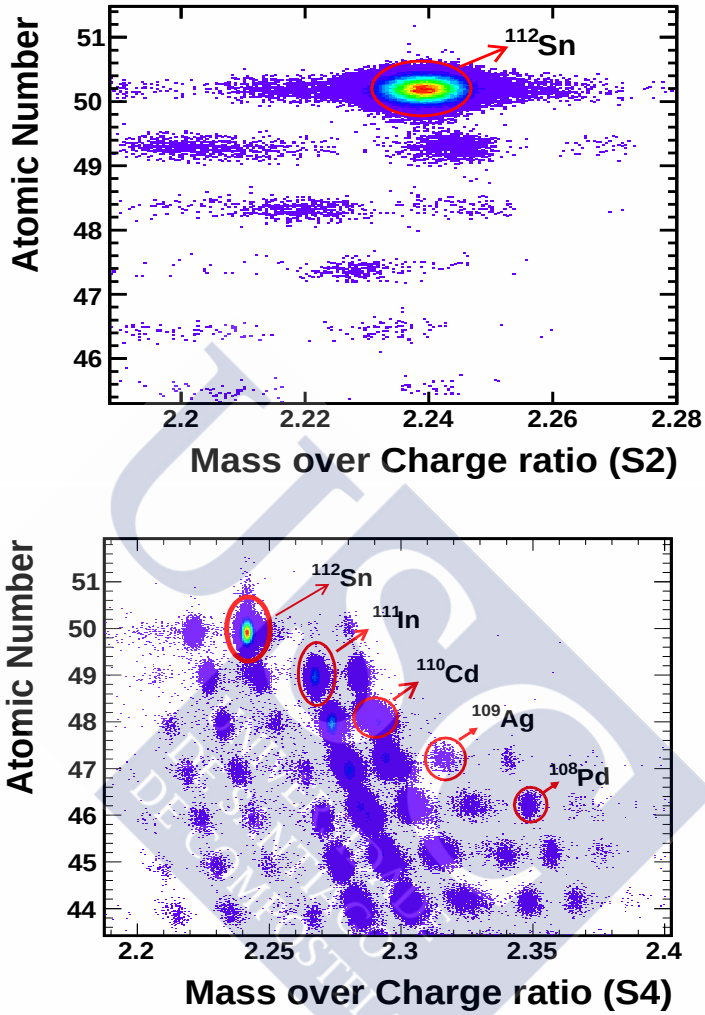

Figure 5.3: *Identification plot of a setting centered in ^{112}Sn at the middle focal plane (S2) (left panel). The right panel shows the identification matrix at the final focal plane (S4) produced in the reaction of ^{112}Sn impinging on the carbon target (right panel). The figure is a overlapping of several magnetic settings of the FRS*

5.2 Nucleon removal cross sections

In a knock out reaction it is possible to remove one or more nucleons in the nucleus peripheral collissions. The identification of this fragment process, as was explained above, it is a first step in the determination of cross section. In the case of the fragmentation using direct beams, we have two

Fragment	f_T	f_d	f_s	Fragment	f_t	f_d	f_s
^{123}Sn	1.00	1.30	1.17	^{123}In	1.68	1.20	1.17
^{119}Sn	1.00	1.30	1.17	^{119}In	1.68	1.20	1.17
^{118}Cd	1.00	1.30	1.17	^{107}Pd	1.68	1.20	1.17
^{111}In	1.3	1.22	1.09	^{106}Pd	1.83	1.25	1.17
^{111}Cd	1.45	1.20	1.17	^{105}Pd	1.27	1.30	1.17
^{110}Cd	2.70	1.25	1.17	^{104}Pd	20.0	1.30	1.17
^{109}Cd	4.35	1.25	1.17	^{107}Rh	1.63	1.25	1.17
^{110}Ag	1.85	1.03	1.17	^{106}Rh	4.34	1.25	1.17
^{109}Ag	1.00	1.03	1.17	^{105}Rh	1.00	1.20	1.17
^{108}Ag	2.58	1.20	1.17	^{104}Rh	66.6	1.20	1.17
^{107}Ag	1.43	1.25	1.17	^{103}Rh	1.39	1.20	1.17
^{108}Pd	1.00	1.25	1.17	^{102}Rh	4.81	1.30	1.17

Table 5.2: *Correction factors for each nucleus The transmission correction factor $f_{T.}$ estimation for each fragment for each set-up that appear in the table 5.1 calculated using the LISE code. f_d, f_s are the dead time and secondary reactions correction factors respectively. The charge states correction factor $f_{ch.st}$ is around $\sim$ 1 % and this value do not appear in the table*

focal planes where it is possible to identify the residues produced in a nuclear reaction. In the case of the fragmentation using unstable beams, the two step configuration must be used. The secondary beam, separated using the first stage of the FRS, impinging on a reaction target placed at the middle focal plane. Figure 5.2 shows an example of selection of ^{112}Sn beam that produce by fragmentation a the identification plot in in the final focal plane S4.

The procedure presented in the section 3.5.1 allows us determinate the cross section of each produced fragment. A important input in order to determine the cross section it is the number of projectiles N_b. In the case of the direct reactions this quantity is determined using the SEETRAM detector, on other hand, the number of unstable projectiles is obtained by the direct selection in the interest fragment and corrected by its respective dead time. Other important input is the number of count corrected by the factors that appear in the table 5.2.

In the table 5.3 are summarized the cross section results. In this table it is possible to observe the results obtained for the proton an neutron removal induced by the Sn projectiles at 1GeV.

Beam	Product	Cross section (mb)
^{110}Sn	^{109}In	69.20 ± 15.87
	^{109}Sn	141.33 ± 29.68
	^{108}Cd	5.38 ± 1.24
^{112}Sn	^{111}In	56.6 ± 13.02
	^{111}Sn	142.02 ± 29.82
	^{110}Cd	3.01 ± 0.69
	^{109}Ag	0.61 ± 0.15
	^{108}Pd	0.03 ± 0.01
^{120}Sn	^{119}In	24.47 ± 5.14
	^{119}Sn	125.57 ± 26.37
	^{118}Cd	1.03 ± 0.24
^{124}Sn	^{123}In	25.62 ± 5.89
	^{123}Sn	138.03 ± 28.99

Table 5.3: *Measured cross sections produced by nucleon removal in the reaction of different Sn beams on carbon target.*

5.2.1 Model calculations

Statistical-abrasion model

As was mentioned in the chapter 1, fragmentation in peripheral heavy-ion collisions at relativistic energies has been studied theoretically by use of microscopic models [2] and macroscopic model descriptions [3, 11, 12, 13] principally.

In the fragmentation process is is divided in two stages. At this point its is important to distinguish the geometrical abrasion model.

In the geometrical description the nucleon removed are proportional to the overlap zone in the abrasion process. But different measures suggest that this assumption is incomplete and for this reason the excitation energy must take into account the orbital wave function of the removal nucleon as suggests the reference [82]. The energy excitation is given by the sum of energies of holes in the single particle level picture with respect to the Fermi surface.

The statistical model of the thermalization or de-excitation is an approximation of the events occurred in the second stage of the fragmentation. The basis of this model is the compound hypothesis [83] which explain the statistical equilibrium in terms of the excitation energy and angular momentum of the prefragment. In this assumption, the second stage of the fragmentation is described by decay in some channels that in a statistical average

have the same probability. Then these energy dissipation or de-excitation process involve the emission of particles, light clusters, γ-rays or the fission fragments.

The probability of a certain de-excitation channel it is proportional to the decays widths are obtained using the Weisskopf-Ewing [84, 85] statistical model In order to evaluate the absolute decays values it is necessary applied the principle of detailed balance that a two system a and b in statistical equilibrium This systems are described by the level densities ρ_a and ρ_b and time reversal invariance is imposed. Then the relation between these states is given by the following equation:

$$\rho_a \Gamma_{ab} = \rho_b \Gamma_{ba} \tag{5.1}$$

here Γ_{ab} is the decay width for the transition a→b , Γ_{ba} is its time reversed process. The Weisskopf-Ewing model depend on the nuclear level density. In order to complement this model, Hauser and Feshbach [86] consider the conservation of angular momentum including a formation of a compound nucleus in J and parity (π) states. In this model the decay width for this process can be calculated using the following equation:

$$\Gamma(U_i, J_i; U_f, J_f, s_\nu) = \frac{(2s_\nu + 1)k_f^2}{2\pi^2}\sigma_f(U_i, J_i)\frac{(2J_f + 1)\rho(U_i, J_i)}{(2J_i + 1)\rho(U_i, J_i)} \tag{5.2}$$

where U_i and J_i are the initial nucleus excitation and total angular momentum, respectively. This initial stage reaches the final state (U_f, J_f) emitting a nucleon or light nucleus ν with a kinetic energy ϵ_ν, spin s_ν, separation energy S_ν and B_ν the Coulomb. Using this information it is possible relate the initial and final energy excitations using the energy conservation as follows:

$$U_i = U_f + \epsilon_\nu + S_\nu + B_\nu$$

Using this expression it is possible to calculate the cross section of the emitting particles and its time reversed process , the fusion as is explained in the references [87, 88, 86]. An alternative statistical model to describe the fission decay channel was proposed by the Bohr and Wheeler [89] but for the purpose this dissetaton we do not explain this model here.

Figure 5.4 represent the energy excitation for different nucleon removed in the abrasion process. For example, in the case of one nucleon removal in is possible to obtain that the energy excitation distribution have a linear behavior with a generated energy that varies between 0 and 40 MeV. The energy distribution of the prefragments with more nucleons removed is given by the convolution of these linear distribution as shown the Fig.5.4 till 7

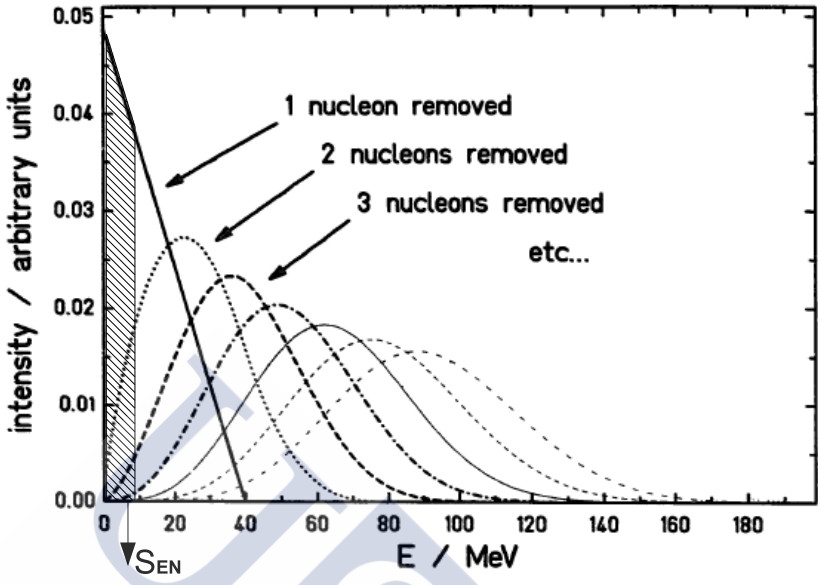

Figure 5.4: *Excitation-energy distributions as calculated with the diabatic model [13] for different prefragments, after the abrasion of 7 nucleons form the projectile nucleus. Neutron evaporation threshold (S_{EN}) is shown.*

nucleons in this case. It is clear to note that the survival probability of a fragment is proportional to the shaded area below of the nucleon evaporation threshold (S_{EN}). When the number of nucleon removal is increased, the survival probability decrease dramatically. For this reason the one nucleon removal probability is higher than the other cases of nucleon removal.

However, in some cases the single particle level assumption does not reproduce the experimental results as show for example the reference [82] present the platinum and iridium produced by the fragmentation of ^{197}Au at 1 GeV. In this work the statistical abrasion model present a best agreement with the data if the excitation energy is doubled, corresponding to an average excitation value about $27MeV$ per abraded nucleon.

Figure 5.5 illustrates this fact. When the single particle level is increased, the probability of remove a nucleon descrease as shown the shaded area. In this way, the statistical abrasion model made a best forecast of the experimental cross section. In this chapter we denote the geometrical abrasion model by Abrabla0, Abrabla $1x$ and $2x$ correspond to the statistical abrasion model using the single particle level a the double energy value respectively.

As was explained Glauber model offers an alternative explanation at the

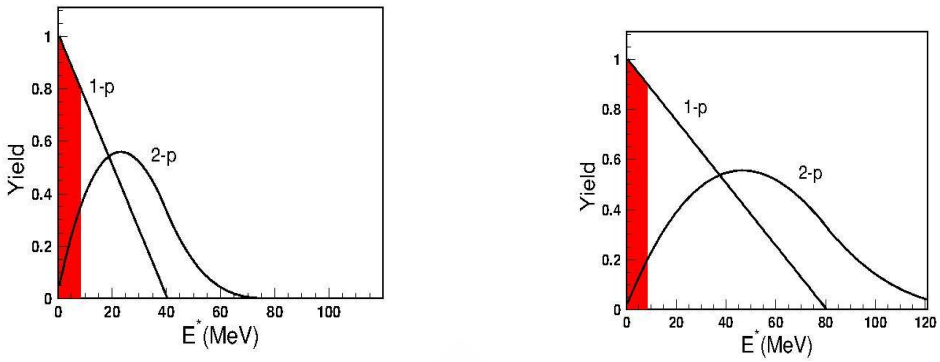

Figure 5.5: *Comparison between the energy excitation distribution in the single particle level calculation. The left panel represent calculations made with an average excitation value about* $13.5MeV$ *per abraded nucleon, the right panel represent calculation made with a double average excitation. The shaded area represent the nucleon evaporation threshold*

problem of the fragmentation by a different point of view. The interaction process is described in terms of nucleon-nucleon collissions . The probability of the occurrence of n nucleon-nucleon collisions with an impact parameter $\mathbf{b}$ is given in the following equation:

$$P(n,\mathbf{b}) = \binom{AB}{n}[T(\mathbf{b})\sigma_{NN}]^n[1-T(\mathbf{b})\sigma_{NN}]^{AB-n} \tag{5.3}$$

The fist term is the number of combinations for finding n collisions out of AB possible nucleon-nucleon encounters where A or B is the number of nucleons in the nucleus A or B. The second term of this equation is the probability of having exactly n collisions, while the last term is the probability of having $AB-n$ misses. T($\mathbf{b}$) is the thickness function for the collisions defined as the probability of have a nucleus-nucleus collision within the transverse element area d$\mathbf{b}$. This thickness function is normalized and it is possible to relate it with the corresponding thickness function for the nucleon-nucleon collision using the following equation:

$$T(\mathbf{b}) = \int \rho(\mathbf{b}_b, z_b)d\mathbf{b}_b\mathbf{z}_b\rho(\mathbf{b}_a, z_a)d\mathbf{b}_a d\mathbf{z}_a t(\mathbf{b}-\mathbf{b}_a-\mathbf{b}_b) \tag{5.4}$$

where $\rho(\mathbf{b}_a, z_a)$ is the probability of finding a nucleon in the transverse area $d\mathbf{b}_a\mathbf{z}_a$ and the $t(\mathbf{b})$ function is defined by the normalization condition:

$$\int t(\mathbf{b})d\mathbf{b} = 1$$

The total probability is the sum of the all possibles probabilities of the occurrence of n nucleon-nucleon collisions and is given by the following equation:

$$\frac{d\sigma}{d\mathbf{b}} = \sum_{n=1}^{AB} P(n,\mathbf{b}) = 1 - [1 - T(\mathbf{b})\sigma_{NN}]^{AB} \tag{5.5}$$

The total cross section σ^{AB} of the interaction nucleus-nucleus is given by the following equation:

$$\sigma^{AB} = \int d\mathbf{b}\left\{1 - [1 - T(\mathbf{b})\sigma_{NN}]^{AB}\right\} = 2\pi \int bdb\left\{1 - [1 - T(b)\sigma_{NN}]^{AB}\right\} \tag{5.6}$$

In its basic form in the quantum mechanical description using eikonal wave functions in order to describe the scattering at high energies. Moreover, in some cases the results can be interpreted in terms of the mechanic of nucleon-like rigid balls in a semiclassical approach.

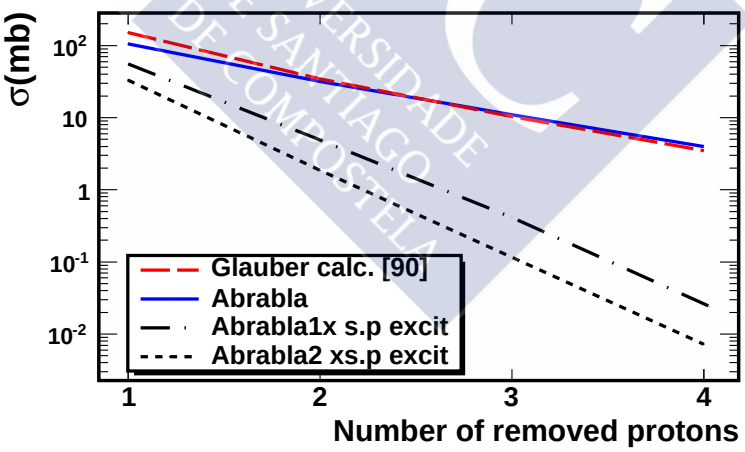

Figure 5.6: *Different codes calculations of the proton removal induced by ^{112}Sn projectiles on carbon target.*

Calculations made by Bertulani [90] using the Glauber model applied to the proton removal induced by ^{112}Sn projectiles on carbon target suggest that the Glauber model is equivalent to the abrasion model as appear in the figure 5.6.

5.2.2 Results and discussion

In this section present a comparative analysis of the cross section presented in the section 5.1 with the code calculations. Figure 5.7 (top panel) shows the cross section of the one proton removal channel as a function of Sn projectile impinging on carbon target. It is clear that in this reaction the cross section decrease when the atomic mass number A increase. Moreover, the different versions of abrabla codes do not reproduce the total experimental tendency of the one-proton removal channel.

In the case of ^{132}Sn [91] , ^{120}Sn and ^{120}Sn present a good agreement with the ABRABLA code with 2x energy excitation. On the other hand, the ABRABLA code with 1x reproduced the ^{112}Sn proton removal channels in the experimental data reported in this work and the cross sections calculated in the Audirac work [92]. However in the case of ^{104}Sn experimental is near to the calculation of the abrasion model without excitation energy consideration.

In a knock out reaction it is possible to remove a neutron in the periphery on a nucleus. Figure 5.7 (bottom panel) shows the comparison with the experimental data of neutron removal channel with the different abrasion calculations.

The cross sections shows in a neutron rich nuclei that probability of remove a nucleon has increased with respect to the proton removal channel is higher. In this case the experimental data shows a good agreement with the abrasion model without energy excitation. This is an evidence that in a neutron rich nuclei the probability of remove a nucleon has increased with respect to the proton removal channel. Furthermore, the proton removal is very sensible to the energy excitation whereas the neutron removal channel is not almost sensible to this effect. It is important to note the dramatic effect of the case of the ^{104}Sn, where in the proton removal calculation its cross section is well reproduced by the abra0 calculation whereas its neutron removal cross section present a good agreement with the calculation using abra2.

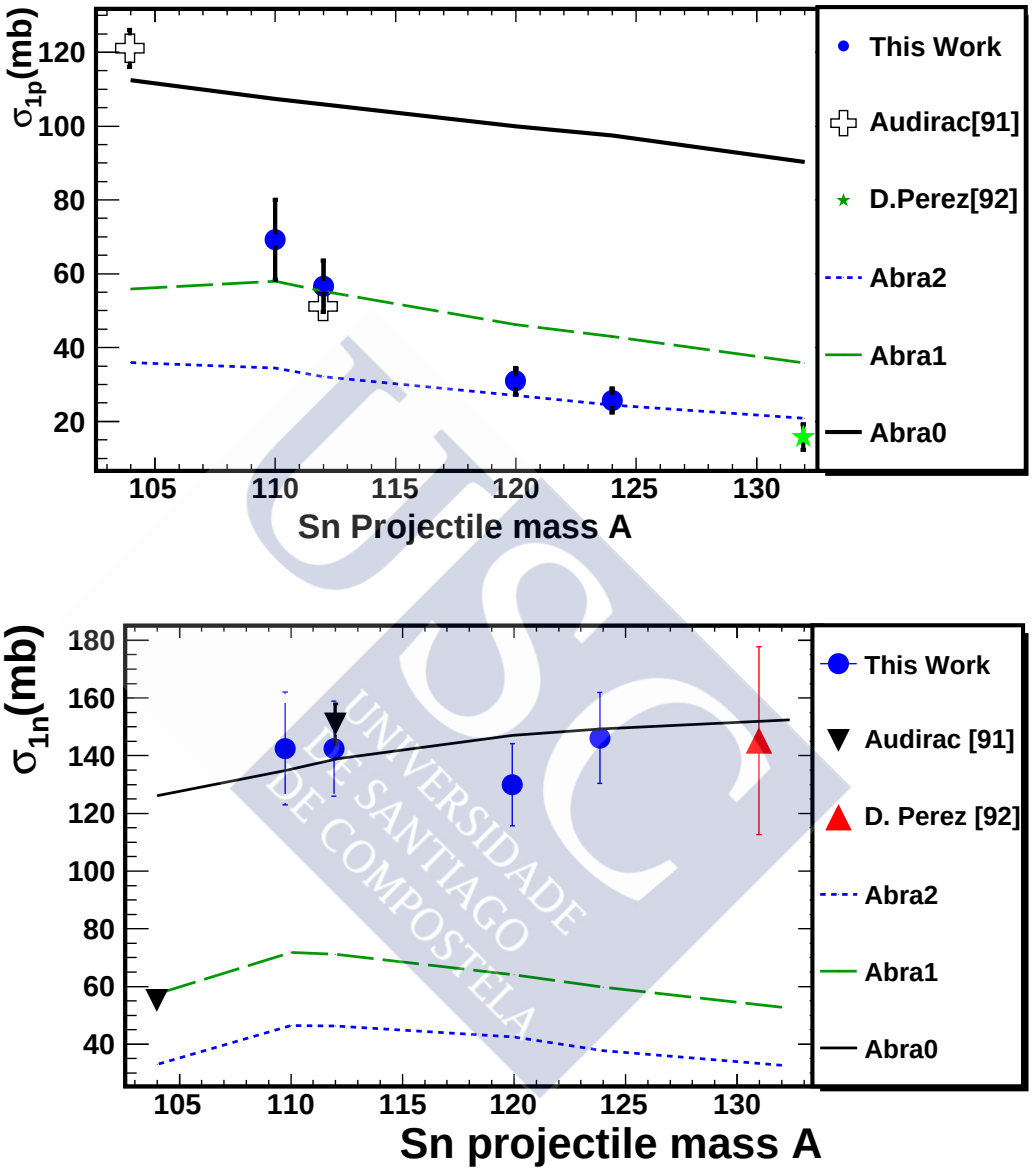

Figure 5.7: *Top panel:One-Proton removal channel cross section as a function of Sn projectile mass. The general behavior of the experimental cross sections do not fit with the different Abra calculations. The Abra2 (dotted line), Abra1 (dashed line) are the Abra code using $2x$,$1x$ factors in the energy excitation. Abra0 (solid line) correspond to geometrical model without include energy excitation. Bottom panel:Comparison between Abla calculations (solid line) and the experimental cross section measures of the one neutron removal channel in the reaction of ^{112}Sn on carbon target*

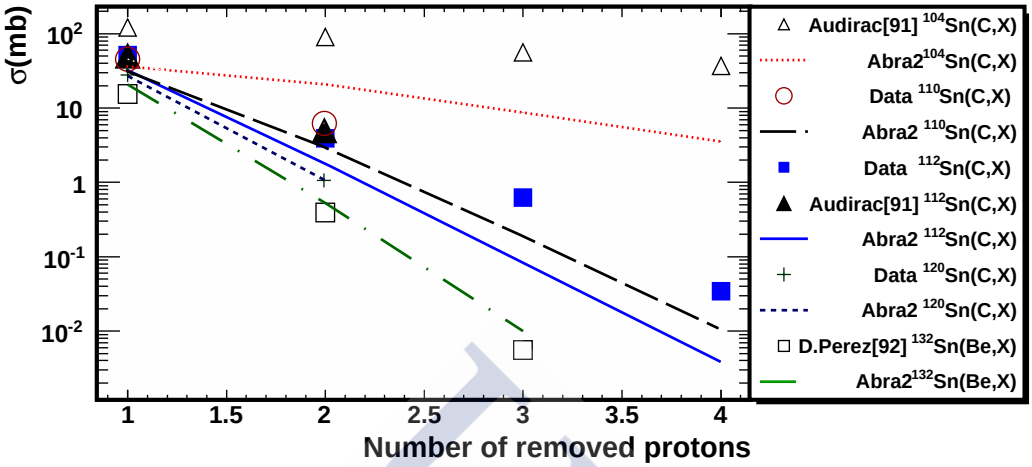

Figure 5.8: *Cross sections of the proton removal channels produced by the fragmentation of Sn beams into carbon target. The experimental data are compared with the calculations of the Abrabla code with* $2x$ *modification in the energy excitation.*

Figure 5.8 shows the proton removal channels in the reaction of ^{112}Sn beam impinging on carbon target. It is clear that the cross section decrease as a number of removed protons of the nucleus. This behavior show us that the remove cross section depends on the removed protons, and the probability to remove the quantity of different proton decreases about a factor 10. This fact was explained using the statistical abrasion model with a single particle approximation illustrate in the figure 5.4.

A complete systematic study of the proton removal channel for different Sn beams is shown in figure 5.9. It is possible to observe that the neutron rich nucleus as ^{132}Sn,^{120}Sn and ^{112}Sn have a good agreement with the abra2 calculations whereas the ^{104}Sn data only is reproduced by a single value using abra0. This important result shows as the influence of the excitation energy and its relation with the isospin quantity.

In addition it is possible to obtain the cross section of the isotopic chain of different nucleus. Figure 5.10 shows isotopic distributions of the production cross section of residual nuclei measured in the fragmentation of ^{112}Sn on carbon target. The abrasion calculation are shown in the same figure.

In the case of Cd and Ag isotopes the abrasion code do not reproduce the cross section, it is clear that the codes overestimate the cross section. Nevertheless, the calculations of cross section Pd and Rh isotopes using abrabla with double excitation energy correction shows a good agreement with the

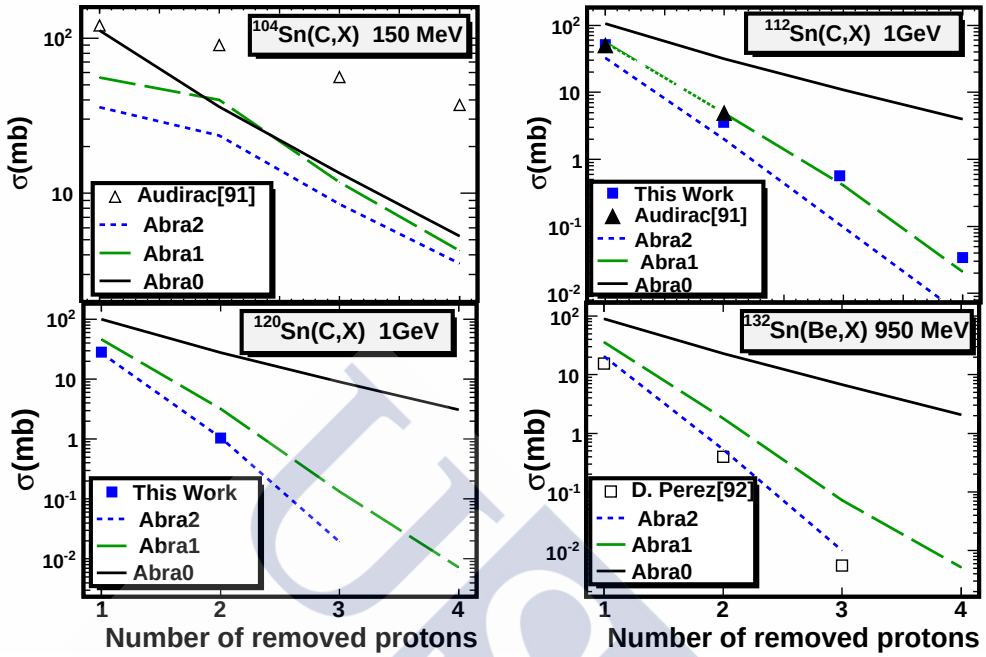

Figure 5.9: *Measured cross sections in the reaction of Sn beams in different proton removal channels. The experimental data are compared with the forecast of ABRABLA code for different versions of excitation energy. The solid line correspond with the abrasion model without energy excitation (geometrical model). The dashed and dotted lines correspond to ABRABLA with 2x and 1x energy excitation respectively*

experimental data.

The results explained above are a signature that the proton and neutron removal channel are sensible to the boundary energy of each nucleon. It is important to remark that each channel can feel differently in the energy excitation.

In the case of the proton removal it is possible to observe a strong dependence between the mass over charge ratio as a function of the energy excitation in the abrasion model. It is clear that the correct prediction of the cross section require a better description of the energy excitation. In the case of the neutron removal, the abrasion without energy excitation forecast is a good description. In this case, the geometrical model is sufficient to describe the behavior of this cross section. Because in our case we have neutron rich nucleus. For this reason, a neutron has less boundary energy and it is more probable to pick up a neutron than a proton. In the description of the proton

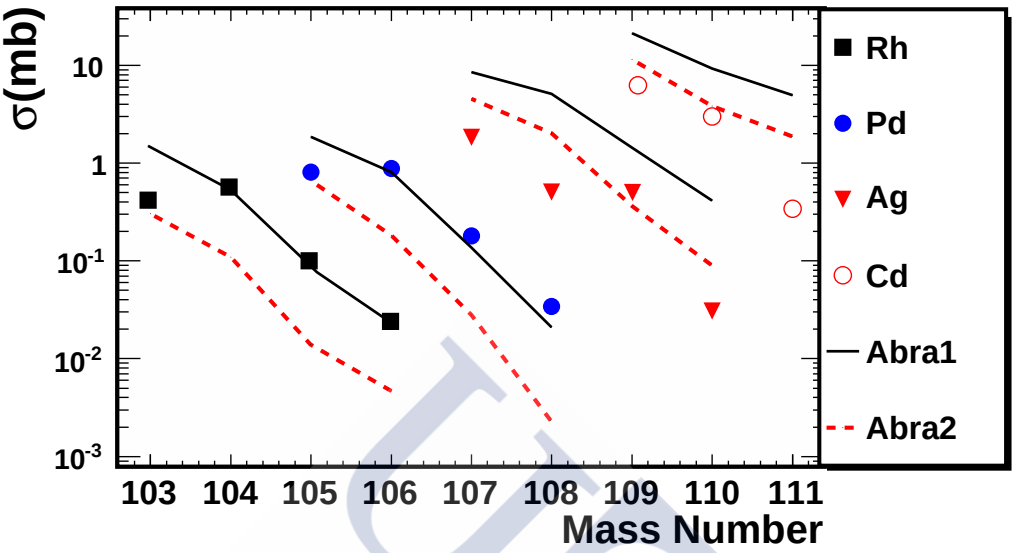

Figure 5.10: *Isotopic distributions of the production cross section of residual nuclei measured in the fragmentation of ^{112}Sn on carbon target at 1 GeV. The lines correspond to different Abla calculations using excitation energy*

removal the abrasion codes can take into account the dependence of the cross section with the energy excitation.

One-nucleon removal reactions from unstable nuclei are expected to be particularly sensitive to the relative densities of neutrons and protons at the surface of the nucleus.

5.3 Energy Distribution

The longitudinal momentum distribution in the nucleon removal was obtained using the same technique described in the chapter 1.

Figure 5.11 shows the comparison between the energy loss distribution of the proton removal channel.

This distribution is much broader than the beam energy distribution. The origin of this effect is related with the proton removal from the nuclear medium. In this case, by energy conservation, the residue feels the recoil momentum due to extract the bound nucleon of the nucleus.

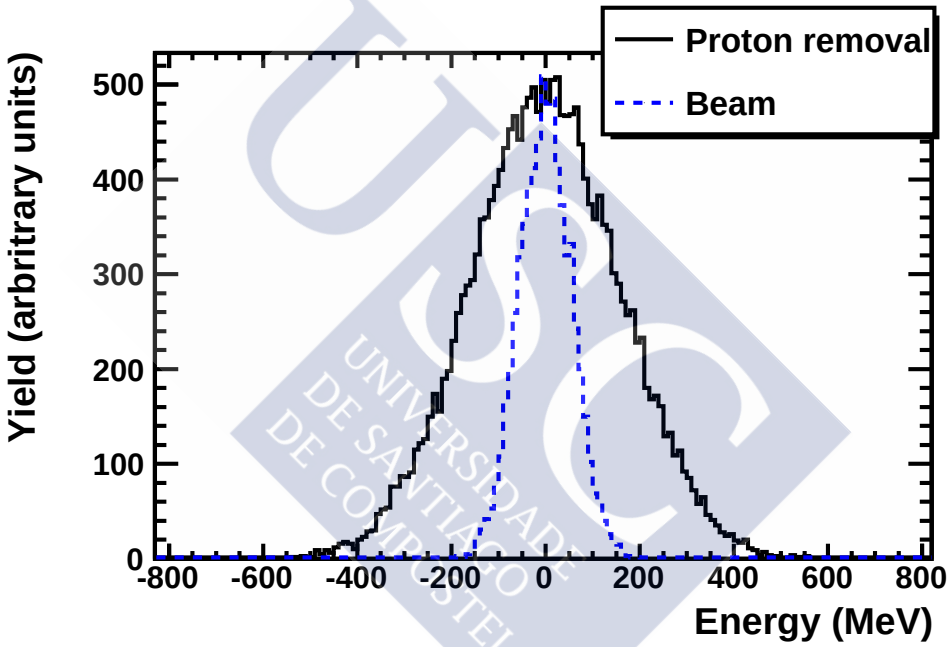

Figure 5.11: *Missing energy distributions of ^{119}In (solid line) produced inthe reaction of the ^{120}Sn (dotted line) at 1GeV impinging on carbon target.*

Conclusions

In this doctoral work we have investigated nuclear and sub nuclear excitations by means of peripheral heavy-ion reactions at relativistic energies. In particular we have used isobaric charge-exchange and knockout reactions. The experimental technique is based on the inverse kinematics approach to induce these reactions. This technique allows the unambiguous identification of the projectile residues and the accurate determination of its longitudinal momentum by using a zero-degree high-resolving power magnetic spectrometer. Using this technique we proposed to use as observables for our investigations the production cross sections and the missing-energy spectra of the projectile residues issued in the reaction channels we propose for these investigations.

The experiment was performed in the GSI facilities in Darmstadt (Germany). The residues obtained in each reaction were analyzed using a magnetic spectrometer FRS (FRagment separator). The high resolution of the spectrometer combined with a detection system allowed us to unambiguously identify the progectile residues is the cornerstone for the determination of our physical observables : the cross section and the energy recoil spectrum of each fragment. In this experiment ^{112}Sn and ^{124}Sn beams induced reactions in different targets such as carbon, cooper, lead and hydrogen at 1GeV energy. Moreover, a systematic of the energy dependence of charge exchange reaction was made with using the ^{112}Sn beams at 1000, 700 and 400 MeV. Using fragmentation reaction was possible to produce ^{110}Sn, ^{120}Sn and ^{120}Sn secondary beams from the stables beams at 1GeV. This secondary beams induced reactions in a carbon target placed at the middle focal plane of the FRS.

In the case of the charge exchange reactions a complete systematic study

was performed. The resolution of the FRS and the targets thickness was optimized in order to disentangle the two components (elastic and inelastic) of the energy recoil distribution. The energy recoil spectra were improved using a unfolding. This unfolding was improved with a regularization in order to fulfill the requirements demanded in this work [65]. The charge exchange reaction spectra shows clearly the two components: quasielastic and inelastic peaks. Moreover, important results obtained using the analysis of complete systematic are shown as follows:

- The unfolding procedure applied to the experimental results show us the Δ resonance in the inelastic peak. This result verifies previous experiments observations [39, 73], but in our case it is possible to observe a additional resonance: the Roper $N^*(1440)$. This result was unexpected and it is a clear example that in peripheral collisions it is possible to excite baryonic resonances. In our measures, it is impossible to dissentangle the contribution of each elementary resonance as its respective multiplet and its respective origin in the target or projectile. In order to solve this drawback it is necessary that future experiments, focus in research of baryonic excitations production in heavy-ions collisions, take into account the pion detection in the target or projectile.

- The systematic analysis of reactions induced by unstable beams show us the limitation of the unfolding method. In order to optimize the unfolding method in these cases, require improve the statistical production of reaction residues in each and reduce the straggling effects by the using of thinner targets.

- The systematic study using different targets and its respective comparison with the proton target showed a clear shift of the inelastic peak toward the quasielastic region. This observation confirm previous results obtained in Saturne . The explanation of this effect could be interpreted in terms of in-medium effects [39, 38, 73] or kinematical effects as suggest the theoretical calculation of [78].

- A energy dependence of the inelastic peak was observed in the reactions induced by the ^{112}Sn beam on carbon and proton targets. The inelastic peak cross section decrease when the energy decrease. This result is explained because the nucleon resonance production required a formation energy as is explained by the quark model picture.

- The peripheral feature of charge exchange reactions guarantees the interaction with the nucleons at low nuclear densities. The comparison

between the total cross section of the np and pn channels produced using different tin projectiles shows us clear differences in this physical observable. This effect is explained because the charge exchange reaction is sensible to the nucleon content. Using the same comparative analysis it is possible to observe a difference between cross section in the np channel when the projectile was changed . This effect is due to the differences in the neutron content of the ^{124}Sn and ^{112}Sn projectiles, this fact demonstrated again the sensibility of the charge exchange reaction to the nucleon content.

A complete understanding of this reaction will reach when the theoretical calculation give us information about the proton and neutron spatial density functions. This information it is an important input in the equation of nuclear state and in addition the r.m.s nuclear radii of our investigated nucleus.

On other hand, the knock out reactions and its respective comparison with the codes give us an idea of the physical processes involved in this reaction. In the case of the neutron knockout the excitation energy is lower than the proton knockout reaction in the case of the neutron rich projectiles. The predictive power of different codes applied in knock out reaction are tested. The systematic study of the different nucleon removal channels shows us that the excitation energy in the calculations of neutron rich nucleus is underestimated. A double value of this excitation energy makes that the experimental results fits with the ABRABLA prediction. This work provides a general framework in order to understand the knock out reactions at different isospin values.

APPENDIX A

List of layers in the experiment

Place	Layer	Material	Thickness(mg/cm^2)
S0	SIS window	Ti	4.5
	SEETRAM	Ti	13.5
Target	PE		95
	C		103,197
	Cu		373
	Pb		954
	Scintillator	C	370.44
	Scintillator	H	34.54
S2			
	TPC1 wind.	C	2.59
	TPC1 wind.	O	0.78
	TPC1	Ar	18.29
	MUSIC1	Ar	107
	Scintillator	C	475.45
	Scintillator	H	44.02
S2 Targets	C		978,1400
	TPC2 wind.	C	2.59
	TPC2 wind.	O	0.78
	TPC2	Ar	18.29
	Air gap	N	60.55
	TPC3 wind.	C	2.59
	TPC3 wind.	O	0.78
	TPC3	Ar	18.29
S4			
	TPC4 wind.	C	2.59
	TPC4 wind.	O	0.78
	TPC4	Ar	18.29
	MUSIC2	Ar	107
	TPC5 wind.	C	2.59
	TPC5 wind.	O	0.78
	TPC5	Ar	18.29

Table A.1: *List of layers of matters used in the FRS beam line*

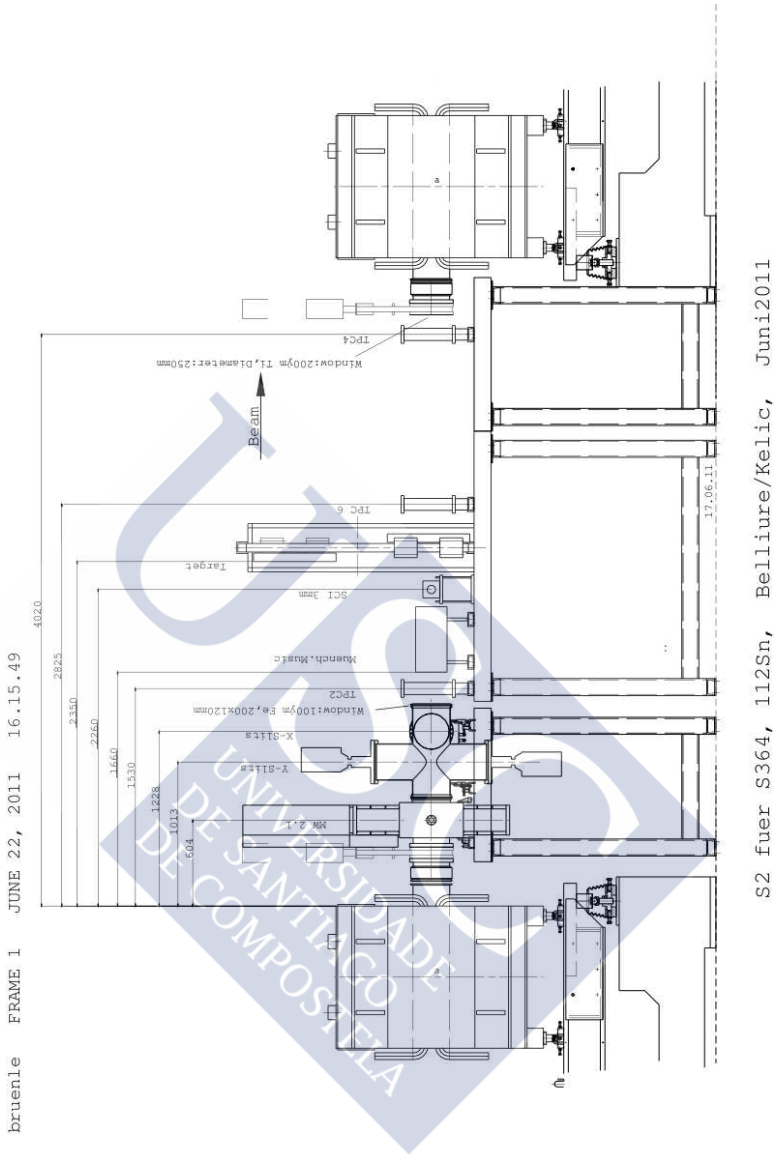

Figure A.1: *Schematic view of experimental set up at S2*

For more technical details see [58, 93] [52]

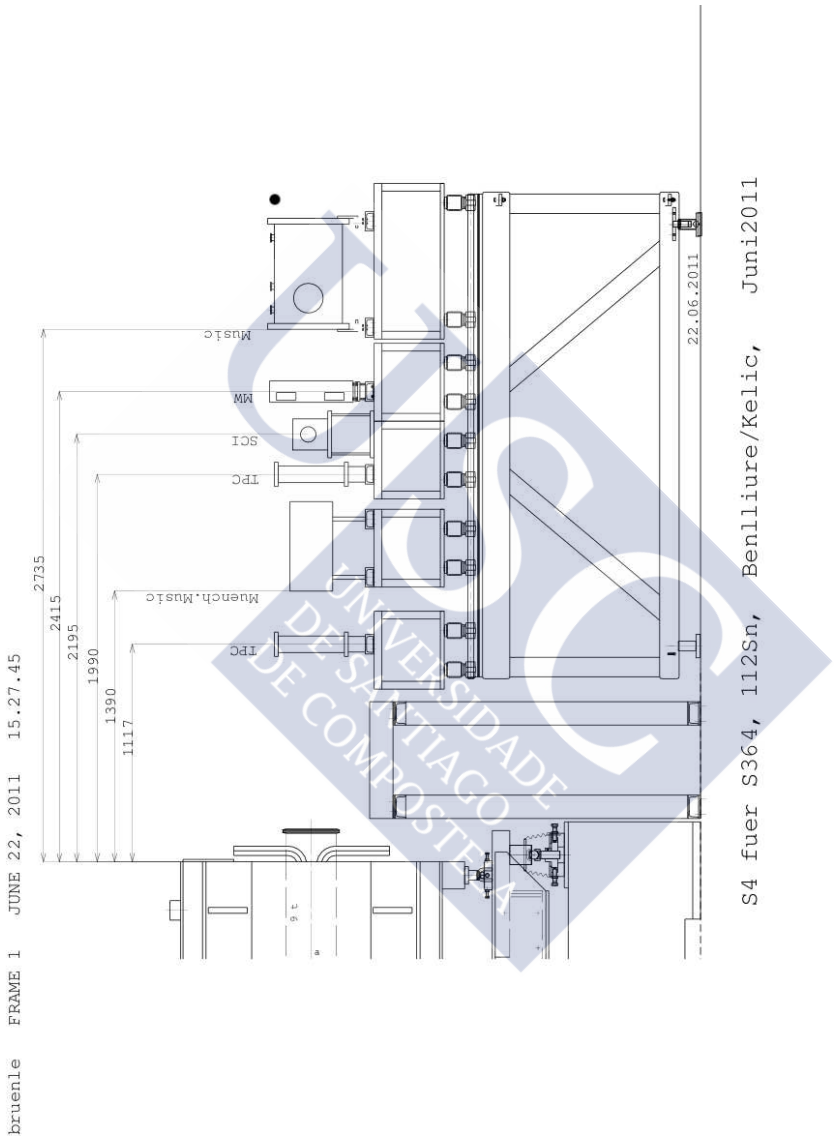

Figure A.2: *Schematic view of experimental set up at S4*

APPENDIX B

Deconvolution Method applied to the Energy Distributions

The magnetic spectrometer FRagment Separator at GSI has been used to investigate the in-medium $\Delta-$resonance excitation in peripheral heavy-ion reactions. The resolving power of this spectrometer makes it possible to disentangle the longitudinal-momentum loss induced by the excitation of the Δ resonance in the projectile residues produced in isobaric charge-exchange collisions. However, beam emittance, electromagnetic interactions of projectile and residual nuclei in the target, and the accuracy of the tracking detectors limit the final resolution. The characterization of the Δ resonance requires then to unfold the measured longitudinal-momentum distribution from the response of the spectrometer.In this work, we use an unfolding procedure based on the Richardson-Lucy method with a regularization technique to optimize the stability of the solution against statistical fluctuations. In present appendix we included a publication wherein this unfolding method and its regularization method is explained in detail.

Nuclear Instruments and Methods in Physics Research A 707 (2013) 16–25

Contents lists available at SciVerse ScienceDirect

Nuclear Instruments and Methods in Physics Research A

journal homepage: www.elsevier.com/locate/nima

Unfolding the response of a zero-degree magnetic spectrometer from measurements of the Δ resonance

J. Vargas, J. Benlliure *, M. Caamaño

Universidade de Santiago de Compostela, 15782 Santiago de Compostela, Spain

ARTICLE INFO

Article history:
Received 2 June 2012
Received in revised form
12 December 2012
Accepted 14 December 2012
Available online 26 December 2012

Keywords:
Unfolding
Regularization
Magnetic spectrometer
Delta resonance

ABSTRACT

The magnetic spectrometer FRagment Separator at GSI has been used to investigate the in-medium Δ-resonance excitation in peripheral heavy-ion reactions. The resolving power of this spectrometer makes it possible to disentangle the longitudinal-momentum loss induced by the excitation of the Δ resonance in the projectile residues produced in isobaric charge-exchange collisions. However, beam emittance, electromagnetic interactions of projectile and residual nuclei in the target, and the accuracy of the tracking detectors limit the final resolution. The characterization of the Δ resonance requires then to unfold the measured longitudinal-momentum distribution from the response of the spectrometer. In this work, we use an unfolding procedure based on the Richardson–Lucy method with a regularization technique to optimize the stability of the solution against statistical fluctuations. The method is validated using measurements of isobaric charge-changing collisions with a ^{136}Xe beam at 500 A MeV.

1. Introduction

The investigation of the Δ-resonance excitation in (p,n) and (^{3}He,t) charge-exchange reactions has revealed how this process is affected by nuclear in-medium effects. The main observation is a downward energy shift of the Δ-resonance peak position by around 70 MeV when using heavy targets ($A>10$) as compared to the mean energy of the Δ resonance produced in free nucleon–nucleon collisions [1,2].

Further experiments investigating the Δ-resonance excitation in charge-exchange reactions using heavy ion collisions also have shown a clear dependence of the magnitude of the downward energy shift in the Δ resonance with the mass of the target nucleus [3]. In these experiments, performed at the Laboratoire National Saturne in France, the longitudinal-momentum of projectile residues produced in isobar charge-exchange reactions was measured with the spectrometer SPES IV [4] with a typical resolution $\Delta p/p = \pm 7\times10^{-4}$.

More recently, it was demonstrated that the magnetic spectrometer FRagment Separator (FRS) [5] at GSI (Darmstadt) can also be used for this purpose [6]. In this case, a ^{208}Pb beam at 1 A GeV was used to induce isobaric charge-exchange reactions in proton, deuterium, and titanium targets, leading to the production of ^{208}Bi. The recoiling nuclei were isotopically identified with the FRS. The corresponding longitudinal-momentum distributions showed two components that were associated to quasi-elastic and inelastic charge-exchange reaction channels. The quasi-elastic channel peak corresponds to Gamow–Teller transitions. The inelastic channel in isobar charge-exchange reactions is understood to be due to the excitation of a Δ resonance in a nucleon–nucleon collision, where the subsequently emitted pion escapes from the nuclear medium. Because of the large pion absorption cross-section, these processes correspond most likely to extremely peripheral collisions. Under such conditions, one can expect that the properties of the excited Δ resonance could provide not only information on the in-medium modifications of the hadron masses, but also on the nucleon–nucleon cross-section at low densities. Moreover, at GSI one can produce beams of nuclei far from stability [7]. Measuring the properties of the excited Δ resonance in isobaric charge-exchange reactions induced via projectiles with a different neutron excess, one could expect to deduce information on the iso-vector component of the nuclear force.

These possibilities depend, however, on the accuracy obtained for the measurement of the Δ-resonance properties, in particular, its average mass and width. The measurements not only depend on the resolving power of the magnetic spectrometer but also on the beam emittance, the position resolution of the tracking detectors, and the electromagnetic interactions of projectile and residual nuclei in the target material and other layers of matter in the beam line. These effects can be corrected via deconvolution of the measured longitudinal-momentum distribution from the response function of the experimental device.

The main advantage of the use of deconvolution methods (rather than, for example parametric models) is the fact that no assumptions on the features of the physical distribution and the response function are needed, avoiding any bias on the final result. In our particular case, the shape of the response function is

* Corresponding author.
E-mail address: j.benlliure@usc.es (J. Benlliure).

0168-9002/$ - see front matter © 2012 Elsevier B.V. All rights reserved.
http://dx.doi.org/10.1016/j.nima.2012.12.087

measured, and the number of peaks in the momentum distributions and their characteristics are obtained as a result of the deconvolution method. In this work, we adapt a well-known deconvolution technique to unfold the response of a magnetic spectrometer from measured longitudinal-momentum distributions. This procedure is based on Richardson–Lucy's technique [8,9] with an additional method to optimize the stability of the result against statistical fluctuations. In the first section of the paper, we discuss the intrinsic resolving power of a magnetic spectrometer and how it can be degraded by the experimental conditions. Then, we describe the unfolding procedure we use. In the final section, we validate the method using measurements of the longitudinal-momentum of residual nuclei produced in isobaric charge-exchange reactions induced by ^{136}Xe projectiles at 500 A MeV in a liquid hydrogen target, obtained with the FRS at GSI.

2. Measuring the longitudinal-momentum of recoiling projectile-like residues in relativistic heavy-ion collisions

The accurate determination of the longitudinal-momentum of nuclei traversing a zero-degree magnetic spectrometer, such as the FRS, depends on the measurement of the corresponding magnetic rigidities. The FRS is an achromatic spectrometer with two symmetric stages and a dispersive intermediate image plane. Under such conditions, the dispersion in magnetic rigidity ($B\rho$) of the trajectories around the central one can be obtained according to the following equation:

$$\frac{\Delta B\rho}{B\rho} = \frac{(x|x)_{24}\Delta x_4 - \Delta x_2}{(x|\delta p)_{24}} \quad (1)$$

where Δx_2 and Δx_4 represent the positions along the dispersive coordinate of the trajectories at the intermediate and final image planes with respect to the central one, $(x|\delta p)_{24}$ represents the dispersion, and $(x|x)_{24}$ the magnification between the intermediate and final image planes.

If one considers incident particles with the same magnetic rigidity, the same expression will provide us the accuracy in the magnetic rigidity determination according to the dispersion in the measurement of the positions of the trajectories at the intermediate and final image planes. The dispersion in the measurement of the positions can be due to the resolution of the tracking detectors, the initial emittance of the beam, or the energy, angular and reaction location straggling of the transmitted particles in the different layers of matter located along the spectrometer, in particular, the target and the detectors placed at the intermediate image plane.

Fig. 1 represents the estimated contributions to the final resolution in the measurement of the magnetic rigidity of ^{136}Cs, produced in the reaction ^{136}Xe+Al at 500 A MeV, due to the resolution of the tracking detectors, the beam emittance, and the electromagnetic interactions of the nuclei with an aluminium target as a function of its thickness. In these calculations, we have taken as reference the nominal values of the dispersion and magnification of the Fragment Separator ($(x|\delta p)_{24} = 6.8$ cm/% and $(x|x)_{24} = 1.16$) and we assume that no matter is located at the intermediate image plane.

In this figure, the thin horizontal lines stand for the contribution to the resolution due to the beam energy dispersion $\Delta E/E = \pm 5\times10^{-4}$ (dotted line) and the tracking detector resolution considering $\Delta x_2 = \Delta x_4 = 2$ mm (dashed line). The thick lines evolving with the target thickness represent the contribution to the magnetic rigidity resolution due to the electromagnetic interactions of the incoming nuclei with the target material, the energy straggling (dashed-dotted line), the angular straggling (dotted line) and the reaction location straggling (dashed line). The solid line corresponds to the final resolution considering all the above mentioned effects.

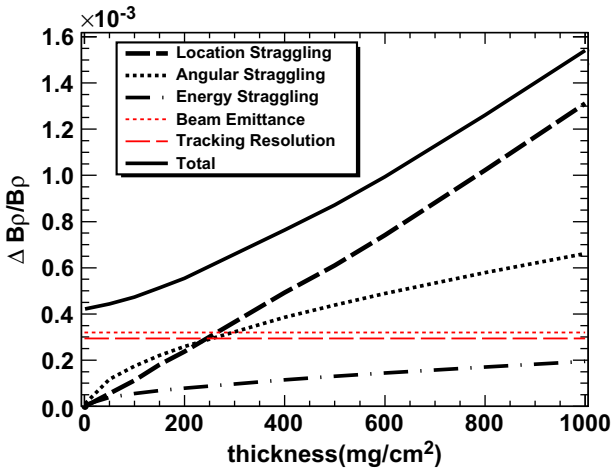

Fig. 1. Simulated contributions to the resolution in magnetic rigidity measurement of ^{136}Cs, produced in the reaction ^{136}Xe+Al at 500 A MeV, with a magnetic spectrometer as a function of the target thickness. The thin horizontal lines represent the energy spread of the beam (dotted line) and the effect due the position resolution of the tracking detector (dashed line). The thick lines represent the effect due to the electromagnetic interactions of the projectile and residual nuclei with the target: energy straggling (dashed-dotted) line, angular straggling (dotted line), the reaction location straggling (dashed line). The thick solid line represents the final resolution considering all the contributions.

As can be seen in the figure, the position resolution of the tracking detectors and the beam emittance limit the magnetic rigidity resolution for aluminium targets thinner than 250 mg/cm^2. For thicker targets, the resolution is limited by the electromagnetic interactions of the transmitted nuclei with the target material.

Unfortunately, the target thickness is very often defined by statistical considerations. In the particular case of measurements with secondary beams of nuclei far from stability, having low intensities, the feasibility of the measurements requires the use of thick targets. In those cases, the possibility of unfolding the contribution of those effects degrading the magnetic rigidity resolution could be an option for accurate measurements. Moreover, the measurement of the momentum dispersion of non-interacting beam nuclei provide an optimal definition of the experimental response function required by the unfolding procedure. Indeed, beam nuclei experience electromagnetic interactions in the target and the layers of matter placed along the spectrometer in a similar manner to the isobar charge-exchange residual nuclei.

3. Unfolding method and numerical calculations

From a mathematical point of view, the measured distribution in the spectrometer **Y** can be described as the convolution of the true distribution of the observable of interest **X** and the response function of the experimental setup **H**

$$\mathbf{Y} \equiv \mathbf{H} \otimes \mathbf{X}. \quad (2)$$

In the case of a histogram representation, a discrete formulation is used

$$Y(i) = \sum_{j=1}^{n_{bins}} H(i-j)\cdot X(j) \quad (3)$$

where $X(j)$ and $H(j)$ are the representations of **X** and **H** as histograms with a n_{bins} number of bins, and $Y(i)$ is the measured

distribution **Y** as a histogram with the same n_{bins}. This holds correct as long as the effect of the response function is a random perturbation of the collection of data within the true distribution [10]. The deconvolution, a special case of unfolding, is then the inverse operation of this process, and it can be used to obtain the true distribution.

Several methods have been developed to calculate the $X(j)$ vector from known $Y(i)$ and $H(j)$ distributions. Unfortunately, no method is free from drawbacks, and the selection of an algorithm depends on the particular conditions of the problem to solve. Some methods, such as the Fast Fourier Transform, produce fast results with a non-iterative procedure but with a poor management of background noise [11]. These spurious effects can be avoided with methods based on the maximum entropy principle [12] but with a fair increase of computing time and a strong dependence on the input parameters. The use of iterative techniques raises the concern about the convergence and/or stability of the solution with the successive iterations. As an example, the Van Cittert method [13] is found to yield oscillating solutions [14]. Other techniques such as Gold [15] or Richardson–Lucy [8,9] produce more stable solutions but they require regularization techniques for selecting the optimal output. A summary of recent unfolding techniques can be found in Ref. [16]. More specifically, different iterative unfolding techniques have been studied in Refs. [8,9,17]. In this work, the Richardson–Lucy deconvolution method is chosen over other techniques. The relatively short computing time it uses to yield a stable solution makes it suitable to repeat several tests with varying conditions in a reasonable time frame. However, the study presented here is not exclusive of this method and it may be applied to other techniques.

3.1. The Richardson–Lucy method and regularization

The Richardson–Lucy deconvolution algorithm is an iterative technique that converges to the maximum likelihood solution for Poisson statistics in the data. This deconvolution algorithm uses the measured distribution and the response function as input to calculate the true distribution. The mathematical formulation of the relationship between a measured value $X(i)$ and the measured distribution in the spectrometer $Y(i)$ is

$$X^{(m)}(i) = X^{(m-1)}(i) \sum_{j=1}^{n_{bins}} H(j-i) \frac{Y(j)}{\sum_{k=1}^{n_{bin}} H(j-k) X^{(m-1)}(k)} \tag{4}$$

where m is the iteration number, n_{bins} is the number of bins of vectors $X(i)$, $Y(j)$, and $H(i)$ is the response distribution; i, j, and k are bin indexes.

As with other deconvolution techniques, the output of this method is iteration-dependent. This issue must be addressed carefully, particularly in those cases where the width of the distribution of a given observable is of interest, as in the case of nucleon resonances. Tests performed with this method revealed that the width of peaks in the true distribution become narrower in successive iterations (see inset in Fig. 2).

In order to minimize the uncertainties associated with the oscillations or degradation of the solution in an iterative deconvolution, a method of regularization is necessary to define the optimal number of iterations. A comparative study of regularization methods and their application to different unfolding techniques can be found in Ref. [18]. As an example, D'Agostini uses a deconvolution algorithm similar to the Richarson–Lucy method, with a regularization technique based on comparison between consecutive iterations [17]. However, as it was mentioned before, such methods relying on the convergence of the solution may yield unreasonable solutions, particularly when determining the widths of the peaks, as it is our case. Techniques, such as the regularization matrix [19], compare small variations in the measured distribution **Y** with the calculated **H** ⊗**X** to assure no loss of information. A drawback of this method is the long computing time required; particularly for a systematic study of various distributions in different conditions.

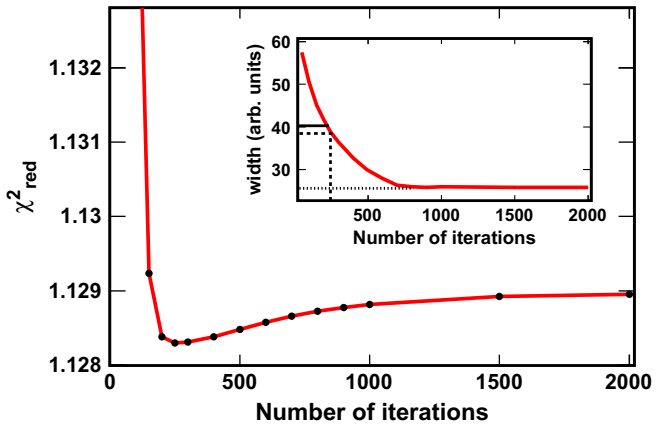

Fig. 2. Typical dependence of χ^2_{red} calculated between the measured distribution and the result of the Richardson–Lucy method with the number of iterations. The minimum χ^2_{red} and the corresponding iteration number N_{min} are indicated with a dotted line. The inset shows the behaviour of the resulting width of a peak contained in a measured distribution with the number of iterations. The true value of the width is indicated with a triangle mark. The deconvolution result converges to a minimal width (dotted line). The result from the application of the χ^2_{red} regularization method is indicated with a dashed line.

In order to optimize the computing time, a relatively simple regularization method based on the χ^2 is proposed in this work. Regularization methods and stopping criteria based on the standard χ^2 are well-known in other applications such as image reconstruction techniques [20]. In some of these methods, the feasibility of the solution is measured with the χ^2, and the process is stopped when this reaches a certain limit, preventing the solution to degrade. In the present case, we look for a minimum of the χ^2 in order to halt the deconvolution process. In addition, the collection of minima resulting from different measurements of the same observable should be centred at $\chi^2_{red} = 1$, where χ^2_{red} is the standard χ^2 normalized to the number of degrees of freedom, and correlated with the true value of the measured observable.

For each iteration of the Richardson–Lucy deconvolution, a χ^2_{red} likeness test between the measured distribution **Y** and the convolution of both the solution **X** and the response function **H** is performed. Due to the histogram-nature of the three distributions, this test is done on a bin-by-bin basis

$$\chi^2_{red} = \frac{1}{(n'-1)} \sum_{i=1}^{n_{bins}} \left(\frac{Y(i) - Y^{Conv}(i)}{\varepsilon(i)} \right)^2 \tag{5}$$

where $\varepsilon(i)$ is the error associated to the measured value of $Y(i)$, and n' is the number of bins with $\varepsilon(i) > 0$. In this case, Y^{Conv} is the histogram resulting from the convolution of H and the calculated X^{Calc}

$$Y^{Conv}(i) = \sum_{j=1}^{n_{bins}} H(i-j) \cdot X^{Calc}(j). \tag{6}$$

As a side note, the method requires that the three histograms $Y(i)$, $H(i)$, and $X^{Calc}(i)$ possess identical binning.

The resulting χ^2_{red} values are evaluated as a function of the number of iterations until a minimum is found at N_{min}. The corresponding $X^{Calc}(i)$ calculated after N_{min} iterations is chosen as the optimal solution. Fig. 2 shows a typical behaviour of χ^2_{red} as a function of the number of iterations, for a numerical case with two Gaussian peaks (see Section 3.3). Right after the minimum at

N_{min}, the value of χ^2_{red} converges around a constant value. However, the effect in the features of the resulting $X^{Calc}(i)$ can be important. The inset of the same Fig. 2 reveals the evolution of the width of a peak, with a true width of 39.7 MeV, contained in the **X** distribution. Its value descends and converges around 26.8, which is an underestimation of some 30%. On the other hand, the value corresponding to the minimum χ^2_{red} is close to 39, which results in a difference of less than 2%.

In our particular unfolding problem, the nature of the experimental observables measured in the FRS spectrometer determine the conditions under which the measured distributions are to be treated: the number of detected events rules the overall statistics of the distributions, and the systematic uncertainties restrict the smallest binning to build the relevant histograms. In order to use the χ^2_{red} as a regularization criteria, the goodness of this method must be explored against different conditions of statistics and histogram binning. In the next sections, two numerical cases are used to perform this study. These cases are chosen to resemble expected measurements in the production of Δ resonances.

3.2. First numerical test: one Gaussian-peak case

In the first case, we simulated a single peak describing the Δ resonance with a Gaussian distribution. In order to reproduce a realistic peak, the resonance distribution is centred at $E_o = -326.6$ MeV with a width of $\sigma_o = 29.9$ MeV, distributed in a histogram with limits -5860 MeV and 2428 MeV. The response function is also a Gaussian of $\sigma_{Resp} = 106.3$ MeV width. The measured distribution is the discrete convolution of both Gaussian functions.

A collection of simulated measured distributions **Y** is produced by varying the statistics and the binning of the histogram. Statistical fluctuations are taken into account applying Gaussian fluctuations in the contents of each bin with a variance equal to the square root of the bin content. These fluctuations are simulated with normal distributions in order to mimic the nature of the experimental measurements, where a collection of systematic uncertainties add to the statistical fluctuations, resulting in an overall Gaussian behaviour. It is important to note that, although the Richardson–Lucy method is based on Poisson distributed statistics, we assume that for a reasonable number of counts the differences between the Poisson and measured distributions reduce and therefore have a small impact on the result. On the other hand, variations on the histogram binning change the number of points available to calculate the true distribution. This effect is equivalent to changing the width of the distribution for a fixed bin size. The Richardson–Lucy deconvolution and the χ^2_{red}-based regularization method are applied to this collection of distributions. For each distribution, the difference between the mean value of the original peak E_o and the one obtained with the deconvolution method E_o^{Calc} is defined as

$$\delta E_o = E_o - E_o^{Calc}. \tag{7}$$

The error in the estimation of the width of the peak is calculated as a percentage

$$\delta\sigma_o = 100\left(\frac{\sigma_o - \sigma_o^{Calc}}{\sigma_o} - 1\right). \tag{8}$$

The panels in Fig. 3 show the behaviour of δE_o and $\delta\sigma_o$ as functions of the number of bins in the histograms for samples with different statistics. The evolution of δE_o with the histogram binning suggests a fairly constant dispersion for each set of statistics. This can be interpreted as the result of the balance between the reduction of the statistics contained in each bin as its size decreases. On the other hand, the dispersion, as expected, depends on the statistics: the figure shows this behaviour. In the case of $\delta\sigma_o$, the situation is similar: the dispersion for each set of statistics is found to be quite independent on the bin size. In both, δE_o and $\delta\sigma_o$, the overall statistics play a more important role than the bin size.

The precision and accuracy of both E_o^{Calc} and σ_o^{Calc} improve with statistics, except for low number of bins. In these cases, Fig. 3 shows that the overall better precision and accuracy of the set with largest statistics is spoiled by the behaviour of the method with larger bin sizes or, equivalently, fewer bins contained in the distribution. Table 1 summarizes the average values and dispersions of δE_o and $\delta\sigma_o$ are listed for the different sets of statistics.

3.3. Second numerical test: two Gaussian-peaks case

The measurement of distributions with more than one peak, and particularly a distribution with two peaks, is among the expected experimental cases (see Section 4). This situation can be simulated with two Gaussian distributions: one placed close to 0 MeV, and another one shifted toward negative values.

Table 1
Average deviations in the mean value (δE_o) and width ($\delta\sigma_o$) obtained unfolding a single Gaussian distribution for samples with different statistics.

Counts	$\langle \delta E_o \rangle$ (MeV)	$\langle \delta\sigma_o \rangle$ (%)
10^3	-1.8 ± 3.6	3.7 ± 8.6
10^4	0.0 ± 1.7	3.9 ± 8.8
10^5	-0.4 ± 2.3	1.7 ± 2.5
10^6	-1.4 ± 2.4	3.3 ± 6.1

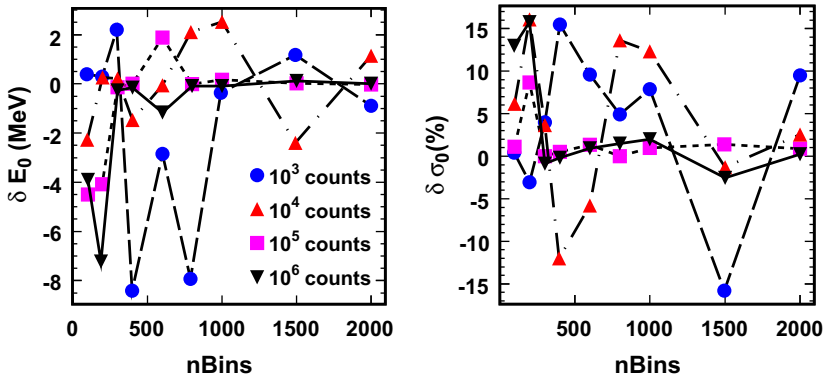

Fig. 3. Deviations in the mean value (δE_o) and width ($\delta\sigma_o$) obtained unfolding a single peak distribution as a function of the bin size and for samples with different statistics.

The response function is again a Gaussian distribution with $\sigma_{Resp} = 106.3$ MeV, and the limits of the histograms are the same as in the case of the single-peak distribution. The positions and widths of both peaks are summarized in Table 2.

As in the previous one-peak case, a collection of experimental **Y** distributions were created by changing the statistics and the histogram binning. Again, random variations of the contents of each bin were applied according to the $Y(i)$ values in order to simulate statistical fluctuations. The statistics were equally shared by the two peaks. The Richardson–Lucy method was then applied to each **Y** distribution to calculate the corresponding $\mathbf{X}^{Calc}$ with the χ^2_{red} regularization test.

Fig. 4 shows the evolution of the previously defined δE_i and $\delta\sigma_i$ of each peak as a function of the bin size and for samples with different statistics. The deviations in mean energy for both peaks are similar to that of the single-peak case: the behaviour shows again a stronger dependence on the statistics than on the bin size. Since the $\mathbf{H}^{Calc}$ distribution contains two peaks, a useful information is the uncertainty on the distance between the two peaks. This deviation can be studied independently of the units of distance by making the ratio to the original distance as

$$\delta\Delta E = 100\left(\frac{E_1^{Calc}-E_2^{Calc}}{E_1-E_2}-1\right). \quad (9)$$

Table 3 shows the average deviations δE_i in the mean energy of the peaks and in the relative distance between both peaks $\delta\Delta E$, while Table 4 summarizes the average deviations $\delta\sigma_i$ in the calculated widths. In general, the accuracy and precision of the results increase with the statistics contained in the histogram **Y**. The range of the overall variations in the width determination is within a window of $\pm 6\%$. In the case of the mean energy E_i, the least favourable test gives a result within a range of ± 8 MeV, which improves for larger statistics. The same applies to the relative distance ΔE, which is calculated within a window of less than $\pm 3\%$ in the worst case, and it reduces down to ± 0.3 for the set with 10^6 counts.

Table 2
Input parameters of the test with two Gaussian distributions.

E_1 (MeV)	E_2 (MeV)	σ_1 (MeV)	σ_2 (MeV)
−4.8	−326.6	25.1	39.7

Table 3
Average deviation in the mean values (δE_i) obtained by unfolding a two-peak distribution and average distance between the mean values of both peaks ($\delta\Delta E_i$) for samples with different statistics.

Counts	$\langle\delta E_1\rangle$ (MeV)	$\langle\delta E_2\rangle$ (MeV)	$\langle\delta\Delta E\rangle$ (%)
10^3	-0.2 ± 1.8	-0.2 ± 8.2	0.0 ± 2.6
10^4	-0.2 ± 1.1	-2.0 ± 1.9	-0.6 ± 0.7
10^5	0.1 ± 1.1	-1.3 ± 1.9	-0.4 ± 0.7
10^6	-0.1 ± 0.6	0.2 ± 0.8	0.2 ± 0.3

Table 4
Average deviation in the widths ($\delta\sigma_i$) obtained by unfolding a two-peak distribution for samples with different statistics.

Counts	$\langle\delta\sigma_1\rangle$ (%)	$\langle\delta\sigma_2\rangle$ (%)
10^3	-4.6 ± 7.5	-1.3 ± 15.4
10^4	-3.4 ± 6.3	-1.4 ± 5.9
10^5	2.8 ± 9.5	-1.0 ± 6.7
10^6	1.1 ± 2.1	0.6 ± 4.0

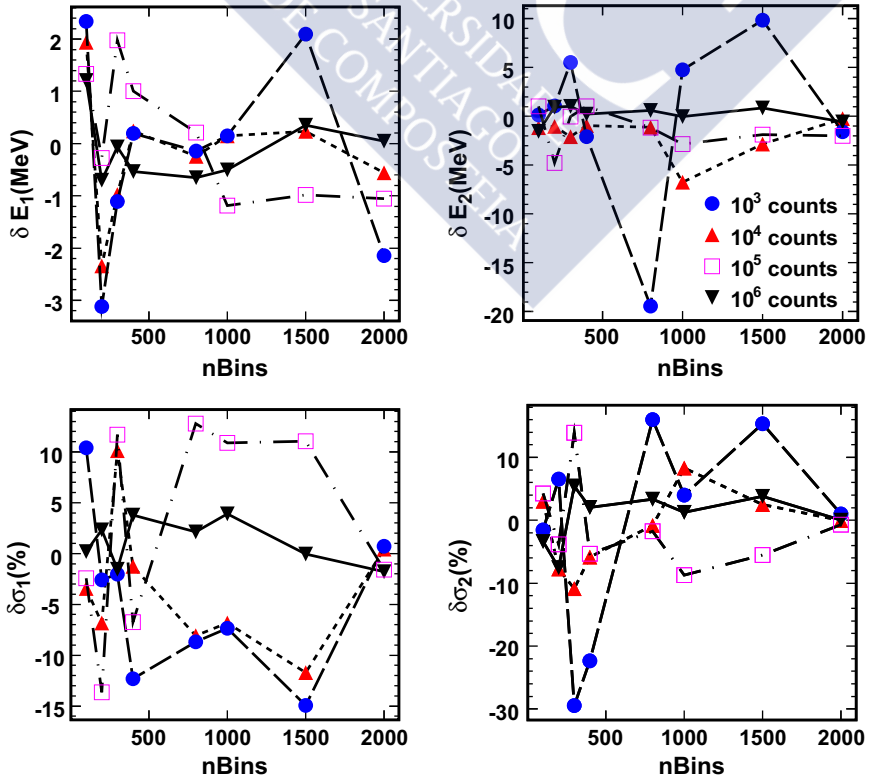

Fig. 4. Deviations in the mean value (δE_i) and width ($\delta\sigma_i$) obtained unfolding a two Gaussian-peaks distribution as a function of the bin size of the distributions and for samples with different statistics. The subscripts 1 and 2 correspond to centred and shifted Gaussian, respectively.

Fig. 5 shows a typical result of the unfolding procedure with a statistical sample of 10^6 counts at 800 bins. The true distribution (solid line) is folded with the response function used in this section, producing the folded distribution (dotted line). Using the deconvolution and the regularization methods it is possible to disentangle the original two peaks from the folded distribution. The resulting function of the deconvolution (dashed-dotted line) presents a good agreement with the true distribution.

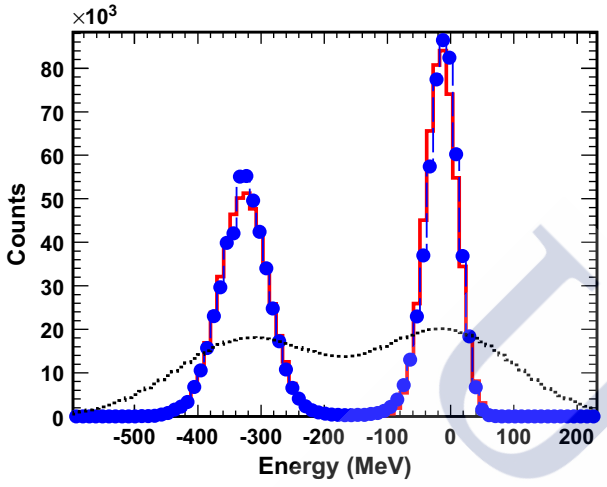

Fig. 5. Comparison between a true distribution and the result of the Richardson–Lucy and χ^2_{red} regularization procedure. The true distribution (solid line) is produced as the sum of two Gaussian-shaped peaks with a total of 10^6 counts. Then convoluted with a response function (not shown) to obtain a simulated experimental energy distribution (dotted line). The Richardson–Lucy and χ^2_{red} regularization methods are applied to this experimental distribution in order to extract the result (dotted-dashed line).

3.3.1. Correlations of calculated parameters

In general, the χ^2 value should be an indicator of the goodness of the result. In order to test this, we represent in Fig. 6 the correlation between the value of the χ^2_{red} from the deconvolution method and the deviation of the result of each parameter in the case of two Gaussian peaks (mean values and widths) respect to their corresponding true values. The panels show that the resulting values concentrate in the vicinity of the true distribution and χ^2_{red} around 1. Interestingly, there seems to be no particular correlation between the value of χ^2_{red} and the accuracy of the results at this stage.

Based on the results shown in Fig. 6, a simple mean value of each parameter would be a good approximation to the results of the deconvolution process. However, a further stage can be applied in order to improve the quality of the results: it is not unusual for deconvolution methods to yield mathematical artifacts within the set of solutions. In order to separate these anomalies, we perform a robust average of the parameters describing the peaks found in the distribution. This procedure, based on the algorithm proposed by Rousseeuw and Van Driessen [21], searches within the set of solutions the subset that minimizes the sum of the standard deviations of the parameters. The minimum size of the subset is fixed at *number of points*+*number of parameters*+1/2.

3.3.2. Application on a simulated case

In the case of actual data, the true distribution **X** is unknown. In the particular case of isobaric charge-exchange reactions, the method extracts the widths and mean energies of the peaks associated with different reaction channels. The procedure for actual data follows a systematic application of the deconvolution and regularization methods on variations of the same set of data. The variations are performed in two ways: (a) the bin size of the $H(i)$ and $Y(i)$ histograms is changed, and (b) the content of each

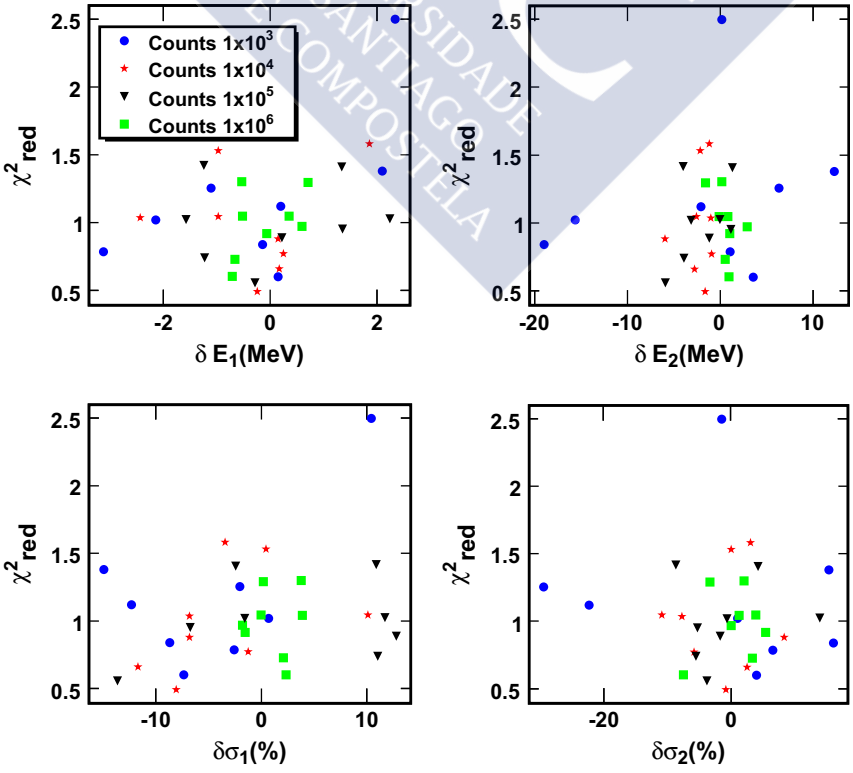

Fig. 6. Correlation between the value of the χ^2_{red} resulting from the deconvolution and regularization methods and the deviations in the mean value (δE_i) and widths ($\delta\sigma_i$) in the case of the two Gaussian-peaks distributions. Each point corresponds to the correlation for a particular binning and number of counts in the histogram.

bin is randomly modified with a variance equal to the square root of its contents, simulating statistical fluctuations. For each of these versions of the histograms, the method is applied and a set of parameters (widths and mean energies in this case) is extracted with the corresponding χ^2_{red}.

In order to test the full procedure, this method is applied to a simulated experimental distribution. As in previous examples, two Gaussian peaks, representing the elastic and inelastic peaks are produced. To simulate a realistic situation, the inelastic peak has four times lower statistics than the elastic one. The histogram contains a total of 2000 counts (400 and 1600 counts each peak). In this practical case, the variations in the histogram binning were 100, 300, 600, and 800 bins; and for each case, a set of 12 versions of the histogram following random statistical fluctuations were performed. Fig. 7 shows the correlations between the widths of the two peaks and the resulting χ^2_{red} for the ensemble of trials. The result after applying the preceding method is represented by the cross-point, while the dot marks the true value of the widths. Both, the result and true value are contained in a region with $\chi^2_{red} \sim 1$, indicated by the dashed area. The final ensemble of trials converge to $\chi^2_{red} = 1.02$, reflecting a connection between the goodness of the result and the χ^2_{red} value. The obtained values for each parameter are summarized in Table 5.

As it can be observed in Table 5, the parameters of the first peak, E_1 and σ_1, profit from the larger statistics, compared to the second peak. However, the true values are all within 2σ of the calculated results.

As a benchmark, the ensemble of trial histograms were also fitted to the sum of two Gaussian functions by standard χ^2 minimization. The effect of the response function was extracted from the resulting $\sigma_{Fit,i}$ by a simple subtraction of the widths squared: $\sigma_i^2 = \sigma_{Fit,i}^2 - \sigma_{resp}^2$. The comparison is also summarized in Table 5. The performance of both approaches are similar. However, the main advantage of the method presented here is that no assumptions on the shape of the peaks or their relative weight are needed. On the other hand, the effect of the response function is not removed based on assumptions on its shape (as in the case of a standard fit), but by using the deconvolution method with whatever shape the response function may have (see Section 2).

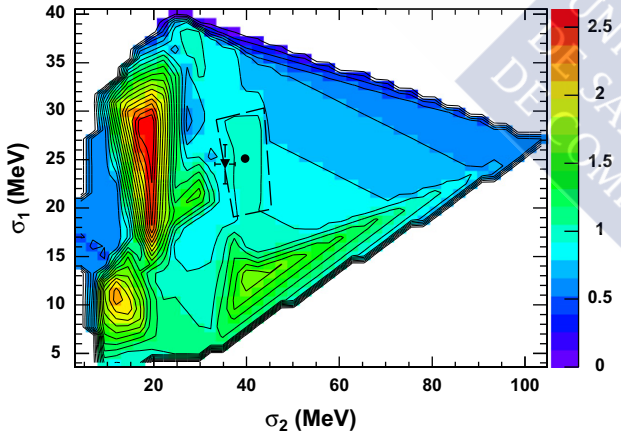

Fig. 7. Distribution of χ^2_{red} obtained by the deconvolution and regularization methods of a two Gaussian distribution changing the binning and statistical fluctuation in the histogram as a function of the resulting widths of the two peaks σ_2 and σ_1. The area enclosed with the dashed-line indicates the region where $\chi^2_{red} \approx 1$. The dot inside of the dashed-line area marks the true value and the triangle correspond to the deconvolution result.

Table 5
Comparison between the final results of the deconvolution method, the results from a standard fit, and the input values (true values) in the case of two Gaussian peaks. See text for details.

Parameter	Deconvolution	Fit	True value
E_1 (MeV)	-13.8 ± 1.9	-21.2 ± 3.0	-14.6
E_2 (MeV)	-330.9 ± 4.1	-333.4 ± 3.0	-326.6
σ_1 (MeV)	25.6 ± 2.4	23.9 ± 5.7	25.1
σ_2 (MeV)	35.2 ± 3.3	39.2 ± 6.1	39.7

4. Characterization of the Δ resonance excited in isobar charge-exchange reactions induced by ^{136}Xe projectiles at 500 A MeV

The excitation of the Δ resonance in isobar charge-exchange collisions between protons and ^{136}Xe nuclei at relativistic energies was investigated as a validation case. This particular reaction has the interest that the production of ^{136}I is only possible via the excitation of the Δ resonance, while the production of ^{136}Cs may occur via the quasi-elastic or the resonant charge-exchange channels. Therefore, the unfolding of the single-peak momentum or energy distribution of ^{136}I could be done using an analytical method that will serve to benchmark the numerical procedure proposed in this work.

4.1. Experiment

This reaction was investigated at the GSI facilities in Darmstadt taking advantage of the inverse-kinematic technique. The SIS100 synchrotron was used to accelerate a beam of ^{136}Xe up to an energy of 500 A MeV. These projectiles impinged on a liquid hydrogen target encapsulated by a container with 36.3 mg/cm^2 titanium windows. The thickness of liquid hydrogen was 87.3 mg/cm^2. Thanks to the kinematics, projectile residues flying forward were identified in atomic and mass number, but also analyzed in momentum using the magnetic spectrometer FRS described in Section 2.

The identification of the projectile residues was obtained from the combined measurement of their magnetic rigidity, time of flight, and energy loss. In the particular case of the FRS, two plastic scintillators [22], located at the intermediate and final image planes, and covering the full acceptance window of the spectrometer, provided not only the time-of-flight of the nuclei but also their positions along the dispersive coordinate. These two measurements were then used to determine the velocities and the magnetic rigidities of the transmitted nuclei. Moreover, an ionization chamber [23], placed at the exit of the separator, provided the energy loss measurement of the nuclei and, from there, its atomic number. From the magnetic rigidity, velocity and atomic number, one could directly deduce the mass number. A detailed description of the experimental technique and data sorting can be found in Ref. [24].

The resolving power of the spectrometer, together with the resolution in position ($\sim$2 mm) and time of flight ($\sim$150 ps FWHM) provided by the plastic scintillators, yielded an excellent separation of the different projectile fragments, as shown in Fig. 8. In this figure, we display in a cluster plot the atomic number versus the mass-over-charge ratio for the nuclei transmitted in two magnetic tunings of the FRS centred on ^{122}Cd and ^{119}Cd. In this figure, each spot corresponds to a different nucleus or an atomic charge state. Using the primary beam as reference one could then identify the transmitted nuclei. In particular, we can clearly observe in this identification plot the primary beam, ^{136}Xe, but also the production of ^{136}Cs and ^{136}I, the two isobar charge-exchange channels produced by the projectile nuclei impinging on the hydrogen target.

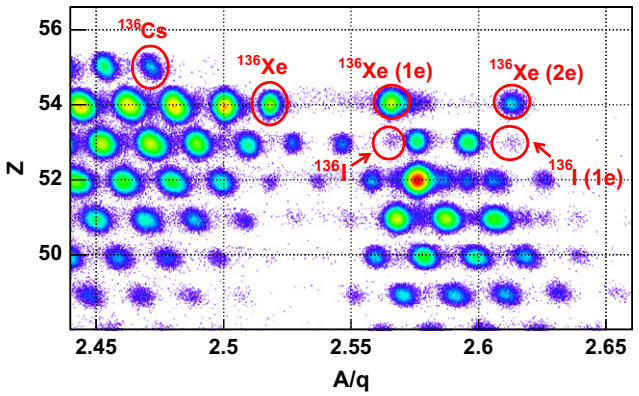

Fig. 8. Cluster plot of atomic number (Z) versus the ratio mass-over-charge (A/q) of the projectile residues transmitted by FRS in two magnetic tunings centred in ^{122}Cd and ^{119}Cd.

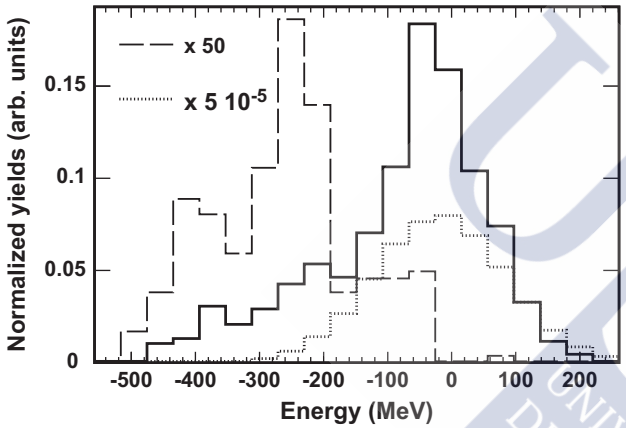

Fig. 9. Energy distribution in the frame of incoming projectiles in the middle of the target for the two residual nuclei produced in the isobar charge-exchange reactions investigated in this work: ^{136}Cs (solid line) and ^{136}I (dashed line). The energy distribution of beam of particles ^{136}Xe (dotted line) is also shown.

4.2. Energy distributions

In order to investigate the excitation of the Δ resonance, we reconstructed the recoiling energy of the projectile residues produced in the two isobar charge-exchange channels investigated in this work, ^{136}Cs and ^{136}I. Energies were obtained from the magnetic rigidities of the events corresponding to these reaction channels. As already mentioned in Section 2, the intrinsic resolution in magnetic rigidity obtained with the FRS is of the order of 6×10^{-4} and, when considering the electromagnetic interactions in the hydrogen target, the final resolution achieved is of the order of 3×10^{-3}. In any case, this resolution is better than the one obtained from time-of-flight measurements.

To correct from reactions in the titanium windows of the hydrogen container, measurements with empty target were also performed and the corresponding energy spectra were subtracted bin per bin from the measurements with the full target (windows plus hydrogen). Fig. 9 shows these energy spectra transformed into the reference frame defined by the energy of the incoming projectile in the middle of the hydrogen target.

The energy distribution of ^{136}Cs shown in Fig. 9 (solid line) presents a dominant contribution around energy zero, compatible with a quasi-elastic (n,p) charge-exchange, and a long tail of events with negative energy. This tail corresponds to collisions where the produced ^{136}Cs nuclei have lost a significant amount of kinetic energy when compared to the one of the incoming projectiles. In the case of ^{136}I (dashed line) the main features are the small amount of events around energy zero and a bump at energies between -200 and -400 MeV. This last spectrum is fully compatible with the (p,n) charge-exchange in reactions between ^{136}Xe and protons, where the quasi-elastic channel is forbidden by charge conservation, and the only possibility would be the charge-exchange via the excitation of the Δ resonance. In order to be more quantitative, the resolution in energy obtained in these measurements could be improved by unfolding the measured spectra from the response function of our experimental device. In this experiment, the measured energy distribution of the primary beam (dotted line in Fig. 9) provide us with the response function of the FRS and its associated detection setup. Indeed the ^{136}Xe projectiles traverse the spectrometer in identical conditions as the charge-exchange residues. The difference by one unit in atomic or mass number represents a negligible effect.

4.3. Characterization of the Δ resonance

The measured energy distributions of ^{136}Cs and ^{136}I were unfolded from the response function of the spectrometer, represented by the energy distribution of ^{136}Xe. We followed the procedure described in Section 3 to unfold the two humped energy distribution of ^{136}Cs, using the regularization technique based on a χ^2-likeness test between the measured energy distribution and the convolution of both the solution and the response function, as a function of the number of bins in the three histograms. The result of this test is shown in Fig. 10, which is an analogue to Fig. 7. The number of bins used for the test were 100, 300, and 600. The statistics per bin was changed as random fluctuations of a Gaussian distribution with a variance equal to the sum of statistical and systematic uncertainties. In the figure, the dashed line delimits the region with $\chi^2_{red}\approx1$, representing the set of solutions that best describe the measured distributions. Moreover, in the same figure, the point inside of the dashed area is the result extracted from the correlation between the four parameters, i.e. the mean values and widths of each peak. After applying the correlation between the parameters, the χ^2_{red} of the final ensemble of trials converge to $\chi^2_{red}=1.13$.

The single humped energy distribution from ^{136}I was unfolded using a similar procedure and regularization technique. In this particular case, and assuming Gaussian distributions for the measured energy distribution for ^{136}I and for the response function of the experimental device, one can also perform an analytical unfolding via the simple quadratic subtraction of the widths of both distributions.

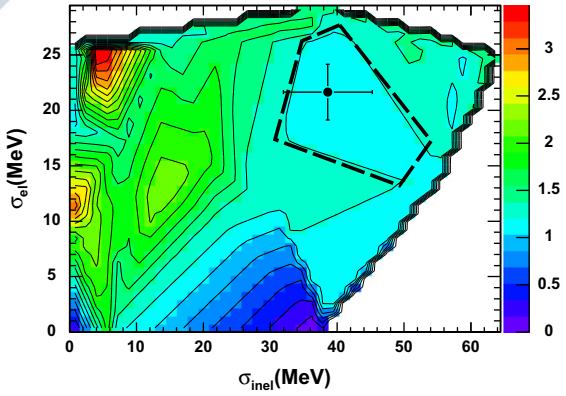

Fig. 10. Distribution of χ^2_{red} obtained by the deconvolution and regularization methods of a experimental distribution changing the binning and statistical fluctuation in the histogram as a function of the resulting widths of the two peaks σ_2 and σ_1. The area enclosed with the dashed-line indicates the region where $\chi^2_{red}\approx1$. The point inside of the dashed-line area marks the result extracted from the correlation between the four parameters.

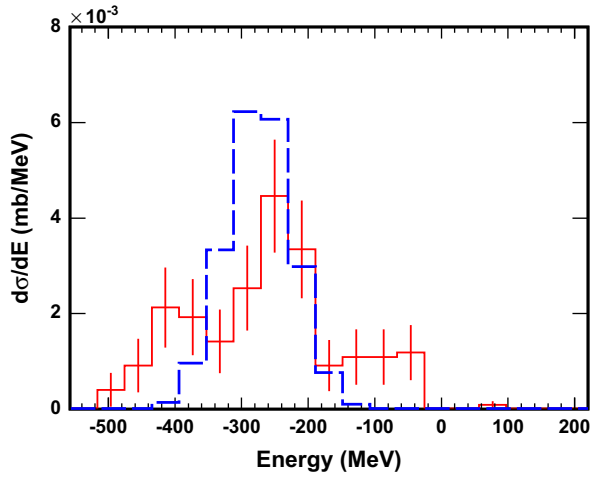

Fig. 11. Measured (solid line) and unfolded (dashed line) energy distribution in the reference frame defined by the energy of the projectiles in the middle of the target for ^{136}I nuclei produced in isobar (p,n) charge exchange reactions induced by ^{136}Xe at 500 A MeV. Error bars represent statistical and systematic uncertainties.

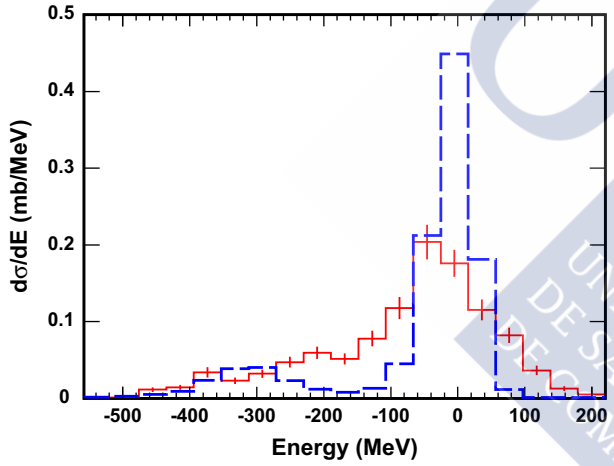

Fig. 12. Measured (solid line) and unfolded (dashed line) energy distribution in the reference frame defined by the energy of the projectiles in the middle of the target for ^{136}Cs nuclei produced in isobar (n,p) charge exchange reactions induced by ^{136}Xe at 500 A MeV. Error bars represent statistical and systematic uncertainties.

Table 6
Mean energy and full widths at half-maximum for the quasi-elastic and inelastic peaks of the recoiling energy distribution for ^{136}Cs and the single humped distribution for ^{136}I as obtained using the unfolding technique but also analytical Gaussian fits in the case of the ^{136}I$_G$.

Channel	E_{el} (MeV)	E_{inel} (MeV)	Γ_{el}	Γ_{inel}
^{136}I$_G$	–	-274.3 ± 17.5	–	95.3 ± 18.4
^{136}I	–	-276.2 ± 23.8	–	127.1 ± 30.7
^{136}Cs	-24.1 ± 1.1	-343.7 ± 12.7	50.9 ± 13.8	90.7 ± 30.9

In Figs. 11 and 12 are displayed the measured and unfolded energy distributions for ^{136}I and ^{136}Cs, respectively. In the case of ^{136}Cs, the unfolded distribution shows two well separated components: one around zero and the second one around -300 MeV. In Fig. 11, the unfolding of the ^{136}I energy distribution yields a single peak centred also around -300 MeV. We can then conclude that both peaks at negative energies in the two distributions should be produced by the same reaction mechanism. Moreover, the fact that the quasi-elastic component around energy zero is not present in the ^{136}I distribution clearly indicates that the peaks we observe at negative energies are due to the excitation of the Δ resonance. In order to be more quantitative, in Table 6 we present the parameters characterizing the energy distributions of ^{136}Cs and ^{136}I, corrected by the resolution of the experimental device used in this experiment. The uncertainty in the determination of the mean value and width of the distributions was around 5% and 30%, respectively. It is worthy to note that these uncertainties are also a consequence of the relatively low-statistics. In this table we also present the results obtained for the energy distribution of ^{136}I using two different unfolding techniques: the one proposed in this work and the result (^{136}I$_G$) of the analytical unfolding of two Gaussian functions representing the Δ peak and the spectrometer response function. The good agreement between the two results can be used as validation of the unfolding technique we are proposing. On the other hand, the mean energy and width of the peak located at negative energies agrees with the expected values for the Δ resonance.

We can then conclude that the present results clearly demonstrate the identification of the Δ resonance in relativistic heavy-ion collisions investigated with the magnetic spectrometer FRagment Separator. Moreover, the observation of the Δ resonance in isobar charge-exchange collisions also ensures that pions emitted in the Δ decay escape from the nuclear medium and, consequently, the Δ should be excited at the periphery of the nucleus.

5. Conclusion

In this work, we make use of an unfolding procedure based on the Richardson–Lucy method to investigate the excitation of the Δ resonance in isobaric charge-exchange reactions induced by relativistic heavy-ions. This unfolding method includes a regularization technique based on a χ^2 test between the measured distribution and the one obtained by folding the result with the response function. This χ^2-likeness test provides the optimum number of iterations for the unfolding according to the binning and statistical significance of the measured distributions. The results obtained with two numerical distributions, with one and two peaks, indicate that the relevant parameter determining the final accuracy of the deconvolution is the statistical significance of the measurement.

The unfolding and regularization techniques presented in this work were used to investigate the Δ-resonance excitation in isobar charge-exchange reactions induced by ^{136}Xe projectiles impinging on a liquid hydrogen target at 500 A MeV. The magnetic spectrometer FRS at GSI was used not only to identify the two isobar charge-exchange nuclei, ^{136}Cs and ^{136}I, but also to determine its recoiling momentum (energy) with high accuracy. Unfolding the energy distribution of ^{136}Cs residual nuclei, we obtained a double peak distribution in the reference frame of the energy of the incident projectile in the middle of the target: with a peak around zero energy and a second peak corresponding to collisions where the ^{136}Cs nuclei have lost, on average, 300 MeV. The energy distribution of ^{136}I, nuclei showed a single peak indicating that all events observed in this case correspond to an energy lost around 300 MeV. The two peaks observed in the production of ^{136}Cs were identified as the quasi-elastic and Δ-resonance channels of the (n,p) charge-exchange. In the case of ^{136}I, the proton target prevents the (p,n) quasi-elastic charge-exchange. This reaction is only mediated by the excitation of the Δ resonance. Moreover, the unfolding technique made it possible to determine the mean energy and width of the Δ resonance with resolutions around 5% and 30% respectively in a relatively low-statistics data set.

Acknowledgements

This work was partially funded by the Spanish Ministry for Science and Innovation under grant FPA2010-22174-C02-01, the programme "Ingenio 2010, Consolider CPAN", and the programme "Grupos de referencia competitiva Xunta de Galicia" under Grant 2010/57. M.C. acknowledges the support provided by the Spanish Ministry of Science and Innovation through the programme "Juan de la Cierva". Discussions with Juan Alcántara are acknowledged.

References

[1] B.E. Bonner, et al., Physical Review C 18 (1978) 1418.
[2] D. Contardo, et al., Physics Letters B 168 (1986) 331.
[3] C. Ellegard, et al., Physical Review Letters 50 (1983) 1745.
[4] E. Grorud, et al., Nuclear Instruments and Methods in Physics Research 188 (1981) 549.
[5] H. Geissel, et al., Nuclear Instruments and Methods in Physics Research Section B 70 (1992) 286.
[6] A. Kelic, et al., Physical Review 70C (2004) 064608.
[7] D. Pérez-Loureiro, et al., Physics Letters B 703 (2011) 552.
[8] W.H. Richardson, Journal of the Optical Society of America 62 (1972) 55.
[9] L.B. Lucy, Astrophysics Journal 79 (1974) 745.
[10] V. Panaretos, in: H.B. Prosper, L. Lyons (Eds.) Proceedings of PHYSTAT 2011 Workshop on Statistical Issues Related to Discovery Claims in Search Experiments and Unfolding, CERN, Geneva, Switzerland, 17–20 January 2011, CERN-2011-006, p. 229.
[11] J.P. Schaffer, et al., Nuclear Instruments and Methods in Physics Research Section B 5 (1981) 75.
[12] Y. Kong, K.G. Lynn, Nuclear Instruments and Methods in Physics Research Section A 302 (1991) 145.
[13] P.H. Van Cittert, Zeitschrift fur Physik 69 (1933) 298.
[14] P. Bandžuch, et al., Nuclear Instruments and Methods in Physics Research Section A 384 (1997) 506.
[15] M. Morháč, et al., Nuclear Instruments and Methods in Physics Research Section A 401 (1997) 385.
[16] H.B. Prosper, L. Lyons (Eds.) Proceedings of PHYSTAT 2011 Workshop on Statistical Issues Related to Discovery Claims in Search Experiments and Unfolding, CERN, Geneva, Switzerland, 17–20 January 2011, CERN-2011-006.
[17] G. D'Agostini, Nuclear Instruments and Methods in Physics Research Section A 362 (1995) 48.
[18] V.B. Anykeyev, et al., Nuclear Instruments and Methods in Physics Research Section A 303 (1991) 350.
[19] J. Albert, et al., Nuclear Instruments and Methods in Physics Research Section A 583 (2007) 494.
[20] E. Veklerov, J. Llacer, IEEE Transactions on Medical Imaging 6 (4) (1987) 313.
[21] P. Rousseeuw, K. Van Diessen, Data Mining and Knowledge Discovery 12 (2006) 29.
[22] B. Voss, et al., Nuclear Instruments and Methods in Physics Research Section A 364 (1995) 150.
[23] M. Pfützner, et al., Nuclear Instruments and Methods in Physics Research Section B 86 (1994) 213.
[24] J. Benlliure, et al., Physical Review C 78 (2008) 054605.

USC
UNIVERSIDADE
DE SANTIAGO
DE COMPOSTELA

Bibliography

[1] Aumann. T. *Eur. Phys. J. A.* , 20:441, 2005.

[2] Metropolis N., Bivins R. , Storm M. et al. . *Phys. Rev.*, 110:185, 1958.

[3] Bowman, J.D.,Swiatecki, W.J.,Tsang, C.F. *Lawrence Berkeley Laboratory report* , 2908:1, 1973.

[4] Blättel B., Koch V., Lang A., Weber K. et al. *The Nuclear Equation of State*. Springer US, 1989.

[5] Hartnack Ch. , M. Berenguer, A. Jahns et al. . *Nuclear Physics A*, 538:53, 1992.

[6] J. Cugnon . *Nucl.Phys. A* , 462:751, 1987.

[7] J. Cugnon, C Volant and Vuillier . *Nucl.Phys. A* , 620:475, 1997.

[8] Glauber R J. *Lecture Notes on Theoretical Physics*, 1, 1959.

[9] J. Tostevin, G.Podolyak, B. A. Brown and P.G. Hansen. *Phys. Rev. C*, 70:064602, 2004.

[10] J. Tostevin, B. A. Brown . *Phys. Rev. C*, 74:064604, 2006.

[11] Morrisey D.J., W.R. Marsh, R.J. Otto et al. *Phys. Rev. C*, 18:1267, 1978.

[12] Oliveira L.F., R. Donangelo et al. *Phys. Rev. C*, 19:856, 1979.

[13] Gaimard J.J. and K.-H Schmidt. *Nuclear Physics A*, 531:709, 1991.

[14] Hüfner, Schäfer K. and Schürmann B. . *Phys. Rev. C.*, 12:1888, 1975.

[15] Al-Khalilli J. NunesF. *J. Phys. G.*, 29, 2003.

[16] Johnson R.C. and Soper P.J.R. *Phys. Rev. C.*, 1:976, 1970.

[17] Friedman W.A. and Lynch W.G. *Phys. Rev. C.*, 28:10, 1983.

[18] Friedman W.A. *Phys. Rev. Lett.*, 60:2125, 1988.

[19] Moretto L.G. and Wozniac G.J. *Nucl. Phys. A*, 488:337, 1988.

[20] A. Kelic and K-H. Schmidt. Report indc(nds)-0530,vienna. Technical report, IAEA, 2008.

[21] R. Schmidt, Trzcińska A. et al. *Phys. Lett. B*, 176:327, 1986.

[22] Köhler T., Blüm, et al. *Phys. Lett. B*, 176:327, 1986.

[23] Yoshida S. and Sagawa H. *Phys. Rev. C*, 69:024318, 2004.

[24] M. Centelles et al. *Phys. Rev. Lett.*, 102:122502, 2009.

[25] Blaum K et al. *Nucl. Phys. A*, 799:30, 2008.

[26] L. Ray et al. *Phys. Rev. C*, 19:1855, 1979.

[27] R. Schmidt et al. *Phys. Rev. C*, 67:044308, 2003.

[28] H. Lenske and Kienle. *Phys. Lett. B*, 647:82, 2007.

[29] Krasznahorkay A. et al. *Nucl. Phys. A*, 731:224, 2004.

[30] M. Fernádez. *Peripheral collisions induced by* ^{124}Xe *and* ^{136}Xe *projectiles at relativistic energies.* PhD thesis, Universidad Santiago de Compostela, Spain, 2007.

[31] J. Cugnon, J. Vandermeulen, and D. L'Hote. *Nucl. Instr. Meth. B*, 111:215, 1996.

[32] Hansen P.G. and Tostevin J.A. *Annu. Rev. Nucl. Part. Sci.*, 53:219, 2003.

[33] Tanihata I., Hamagaki H. et al. . *Phys. Rev. Lett.*, 55:2676, 1985.

[34] Hansen P.G., Jonson B. *Europhys. Lett.* , 4:409, 1987.

[35] D. Bazin, B. A. Brown,C. M. Campbell,J. A. Church,D. C. Dinca et al. . *Phys. Rev. Lett* , 91:012501, 2003.

[36] Bertsch G F and Esbensen H. *Rep. Prog. Phys*, 50:607, 1987.

[37] Y. Fujita, B. Rubio, W. Gelletly. *Progress in Particle and Nuclear Physics*, 66:549, 2011.

[38] Gaarde, C. *Annu. Rev. Nucl. Part. Sci*, 41:187, 1991.

[39] Osterfeld,F . *Rev. Mod. Phys.* , 64:491, 1992.

[40] S.J. Lindenbaum and R.M. Sternheimer . *Phys. Rev. 105* , 105:1874, 1957.

[41] Franey, Love. *Phys. Rev. C*, 31:488, 1985.

[42] Gaarde, C., J. Rapaport, T.N. Taddeucci, C.D. Goodman, C.C. Foster et al . *Nucl. Phys. A.*, 369:258, 1981.

[43] Moake,G.L., L.J. Gutay, R.P. Scharenberg, P.T. Debevec, and P.W. Quin. *Phys. Rev. Lett.*, 43:910, 1979.

[44] Anderson,B.D., J.N. Knudson, P.C. Tandy, J.W. Watson, R, Madey, and C.C. Foster . *Phys. Rev. Lett.*, 45:699, 1980.

[45] Ikeda, K.S. Fuijii and J.I.Fujita. *Phys. Lett.*, 3:271, 1963.

[46] Gutierrez, C, De Sanctis, M . *PRAMANA,Journal of Physics*, 72:541, 2009.

[47] C. Amsler et al. . *Phys. Lett. B*, 667:1, 2008.

[48] H.Geissel,et al. *Nucl. Instr. Meth. B*, 70, 1992.

[49] Manley, D.M. . *Phys. Rev. D*, 51:9, 1995.

[50] Roper, L.D. . *Rev. Lett.*, 12:340, 1964.

[51] Wong S.M . *Introductory Nucear Physics.* Prentice Hall,New Jersey, 1990.

[52] `http://www.gsi.de`.

[53] M. Steiner, M. Blasche, HG Clerc , et al. *Nucl. Instrum. and Methods A*, 312:420, 1992.

[54] R. Anne, A. Lefol,G Milleret and R. Perret . *Nucl. Instr and Meth.* , 152:395, 1985.

[55] B. Jurado,K.H.. Schmidt and K.H. Behr . *Nucl. Instr and Meth. A*, 483:603, 2002.

[56] N.Iwasa et al. *Nucl. Instr. Meth. B*, 126:284, 1997.

[57] K.L.Brown. *SLAC-Report*, 91, 1970.

[58] `http://www.usc.es/genp/s364.html`.

[59] B. Voss , T, Brohm, H.G Clerc , et al. *Nucl. Instr. Meth. A.*, 364:150, 1995.

[60] M. Pützner, H. Geissel,G Münzenberg, F. Nickel , et al . *Nucl. Instrum. and Methods B*, 86:213, 1994.

[61] V. Hlinka et al . *Nucl. Instr. Meth. A*, 419:503, 1998.

[62] R. Janik, A. Prochazca, B Sitar, P. Strmen, I. Szarzka, H. Geissel,K.-H Behr, C. Karagiannis . *Nucl. Instr. Meth. A*, 640:54, 2011.

[63] Carey D.C . *The Optics of the Charged Pericles Beams.* Harwood Academic Publishers, 1987.

[64] K-H Schmidt, E. Hanelt, H Gissel, G. Munzenberg, and J.P. . *Nucl. Instr. Meth. A* , 260:150, 1987.

[65] J. Vargas, J. Benlliure, and M. Caamaño. *Nucl. Instr. Meth. A*, 707:16, 2013.

[66] G. D Agostini . *Nuclear Instruments and Methods in Physics Reseach A*, 362:48, 1995.

[67] Veklerov E., J. Lacer . *IEEE Transitions on Medical Imaging 6*, 4:313, 1987.

[68] Albert J. . *Nuclear Instruments and Methods in Physics Reseach A*, 583:350, 2007.

[69] P. Rousseeuw, K. Van Diessen. *Data Mining and Knowledge Discovery*, 12:29, 2006.

[70] P.J Karol. *Phys. Rev. C* , 11:1203, 1975.

[71] C. Scheidenberger,Th. Stöhlker. W.E. Meyerhof, H. Geissel, P.H. Mokler, B.Blank . *Nucl. Instr and Meth. B*, 142:441, 1998.

[72] C.Scheidenberger et al. *Nucl. Instr. Meth. B.* , 142:441, 1998.

[73] E. Grorud, et al. *Nuclear Instruments and Methods in Physics Research*, 188:549, 1981.

[74] Bachelier, D et al. *Phys. Lett. B.*, 172:23, 1986.

[75] Roy-Stephan, M. *Nucl. Phys. A.*, 488:187, 1988.

[76] Kelic, A. et al. *Physical Review C.*, 70:064608, 2004.

[77] H. Seitz. *Nucl. Instr. Meth.*, 86:157, 1970.

[78] Vidaña I. private communication, 2014.

[79] Krpic D., Puzovic J. et al. *Phys. Rev. C*, 46:46, 1992.

[80] Morsh H.P., Zurpranski P. . *Phys. Rev. C*, 61:024002, 1999.

[81] Krpic D., Drndarevich S et al. *Eur. Phys. J. A*, 20:351, 2004.

[82] K.-H Schmidt, T, Brohm, H.G Clerc , et al. *Physics Letters B*, 300:313, 1993.

[83] Bohr N. *Nature* , page 344, 1936.

[84] Weisskopf V. *Phys. Rev.* , 52:295, 1937.

[85] Weisskopf V., Erwing D.H. *Phys. Rev.* , 57:472, 1940.

[86] Hauser W. and Feshbach H. *Phys. Rev.*, 87:366, 1952.

[87] Bertulan C.A. and Danielewicz P. . *Introduction to nuclear reactions.* Institute of Physics Publishing, 2004.

[88] J. Benlliure. *Lect. Notes Phys.* Prentice Hall,New Jersey, 2006.

[89] Bohr N. and Wheeler J.A. *Phys. Rev.*, 56:426, 1939.

[90] Bertulani C.A. private communication, 2013.

[91] D. Pérez et al. . *Phys. Lett. B.* , 703:552, 2011.

[92] L. Audirac, A. Obertelli, P. Doornenbal et al. *Phys. Rev. C.* , 88:041602, 2013.

[93] http://igfae.usc.es/~genp/index.php?option=com_content&view=article&id=88&Itemid=3.

[94] Horowitz C.J and Piekarewicz. *Phys. Rev. Lett.*, 86:5647, 2001.

[95] B. Margolis . *Nucl. Phys. B*, 4:433, 1968.

[96] R. J. Lombard and J.P. Maillet. *Europhys. Lett.*, 6:323, 1988.

[97] B.A. Li,M. Hussein and W. Bauer . *Nucl. Phys. A*, 533:749, 1991.

[98] Barreau P., M. Bernheim, J. Duclos,et al . *Nucl. Phys. A*, 402:515, 1983.

[99] Meziani, Z.E., P.Barreau, D.H.H. Hoffmann, et al . *Phys. Rev. Lett.*, 54:1233, 1985.

[100] Sealock, R.M., Giovanetti, S.T. Thornton et al. *Phys. Rev. Lett.* , 62:1350, 1989.

[101] Chanfray, G and M. Ericson . *Rev. Mod. Phys.* , 141:163, 1984.

[102] K.-Schmidt,K. Sümmerer, H. Geissel et al. *Nucl. Instr and Meth. B*, 142:441, 1998.

[103] V. Highland. Some practical remarks on multiple scattering. *Nucl. Instrum. and Methods A*, 129:497, 1975.

[104] A. Boudard, J. Cugnon, S. Leray, C. Volant. Intranuclear cascade model for a comprehesive description of spallation reaction data. *Phys. Rev. C*, 66:615, 2002.

[105] O.B. Tarasov, D. Bazin. *Nucl. Instr. Meth. B*, 266:4657, 2008.

Resumen en Castellano

El objetivo de esta tesis es brindar un detallado análisis experimental de las reacciones periféricas. Dicho estudio estará focalizado en analizar las reacciones de intercambio de carga carga y de *knock out*. Las actuales técnicas experimentales nos permites tener haces de iones pesados con energías relativistas y de excelente intesidad. Este hecho permite un gran estudio de las reacciones de fragmentación orientadas a crear haces secundarios y de esta forma extraer información de los nucleos ricos en neutrones. En este punto las reacciones de fragmntención se convierten en una importante herramienta ya que a partir de la colisión de un haz de nucleos estables es posible producir a través de reacciones periféricas un gran número de residuos que generalmente son exóticos. Estos fragmentos tienen velocidades cercanas a la del haz. Con estos haces secundarios es posible investigar una amplia gama de nucleos complemnetanto la información sobre posibles dependencias de las reacciones nucleares con el isoespín. Agregado a esto, con las técnicas demominadas *in-flight* que consiste en la identificación isotópica a partir del tiempo de vuelo de los diferentes isótopos a lo largo de de un espectrómetro magnético.

Reacciones periféricas: Intercambio de carga y Knock out

Para poder entender el proceso de fragmentación ocurre en dos partes a escalas de tiempo diferentes. El primer proceso es la súbita reacción entre el proyectil y el eyectil (del orden de $\sim 10^{-23}$s). que puede modificar la composición de los participantes en la reacción e introducir energía de exitación. el proseso subsiguinte es la desexcitación del núcleo por medio de la evaporación. Este es un proceso que puede llevar a la emisión de nu-

cleones, nucleos ligeros, rayos γ o llevar a procesos como la fisión. Bajo esta visión el problema puede ser descrito generalmnte bajo dos puntpos de vista : el miscroscópico y el macroscópico. Ejemplos de estos modelos son el de cascada-intranuclear cuyo fundamento es la explicación microscópica y los modelos de abrasión es claro un ejemplo de los modelos macroscópicos por antonomasia. En los códigos de cascada intra nucleares describen las diferentes interacciones secuenciales nucleon-nucleon llamadas cascadas en un campo medio nuclear. Por otro lado el modelo de abrasion es un modelo geométrico que describe la fragmentación en términos de una zona de solapamiento donde se encuentran los *participantes* de la reacción y otra zona que es considerada sin pertubación haceindo una aproximación adiabática. A esta zona se le denomina *expectador*. Usando métodos numéricos es posible calcular la zona de solapamiento y de esta manera a partir del parámetro de impacto poder determinar la probanilidad de arrancar un nucleon El segundo paso en este modelo es la ablasión. En este punto a partir de un modelo de estadístico de ablasión es posible calcular la energía de excitación despues del proceso se abrasión. En este caso la energía de excitación es dada por el conteo directo de los huecos dejados al arrancar varios nucleones con respecto la superficie de Fermi. El modelo de abrasion-ablasion puede tener algumas desviaciones sistematicas con respecto a los datos experimentales atribuidas a la inadecuada estimación de la energía de excitación de los fragmentos. Los modelos de Glauber y ecuaciones de transporte son también usados para describir este proceso. El modelo de Glauber en su forma más básica consiste en una descripción cuántica usando funciones de onda eikonales para determinar la dispersión de partículas en una colisión.

Descripción del experimento

En esta tesis se presentan resultados experimentales cinématica inversa. Con esta técnica es posible inducir reacciones periféricas y extraer de ellas observables físicos como las secciones eficacez y las distribuciones de energía.

Para extractar estos observables físicos se requiere de un sistema detección excelente resolución así como de un espectrómetro con alto poder de resolución. En nuestro caso, realizamos las medidas experimentales en las instalaciones del GSI en Darmstad Alemania. Estas medidas experimentales se obtuvuieron con el FRS (FRagment Separator) que es un espectÅ•ometro magnético que usa la técnica *in-flight*. El FRS tiene esta dividido en dos partes simétricas: una es el plano focal intermedio o así llamado dispersivo ($S2$), y el otro es el plano focal final $S4$.

Las medidas realizadas en este experimeto se hicieron con haces estables

e inestables de estaño. Los haces secundarios son obtenidos a partir de la reacción de los haces directos con un blanco de producción.

El montaje experimental en el caso de la reccionen con haces estables esta representado en la figura B.1. En esta configuración es posible generar las reacciones de intercambio de carga y knock out se realiza en el blanco ubicado a la entrada del FRS ($S0$). Por otra parte cuando se trabaja con haces secundario es necesario usar otra configuración del FRS. En esta configuracion un haz directo interactua cion un blanco de producción ubicado a la entranda del FRS donde usando la primera parte del FRS es posible seleccionar el haz secundario que a su vez interactua con un segundo blanco presente en el plano focal intermedio. La identificación de las reacciones originadas con el haz secundario se realiza en el plano focal final.

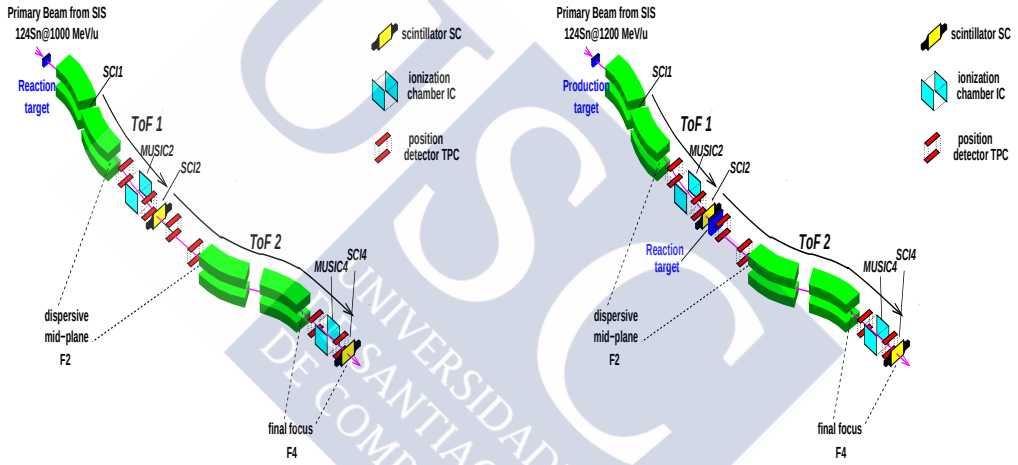

Figure B.1: *Representración de las dos confifuraciones del FRS usadas en este trabajo. La figura de la izquierda corresponde a la configuración cuando para las reacciones usando haces diréctos. La figura de la derecha muestra la configuración experimental para trabajar con haces secundarios.*

Es importante resaltar que los haces directos usados fueron ^{112}Sn y ^{124}Sn a 1GeV, y los haces secundarios producidos fueron ^{110}Sn, ^{120}Sn y ^{122}Sn también a 1GeV. En el caso del haz ^{112}Sn se hicieron medidas para conocer las posibles dependecias de el intercambio de carga con esta variable, estas energías fueron $1GeV$, $700MeV$ y $400MeV$ La identificación usando el comportamiento de las pariculas cargadas se hace usando la rigidez magnética

$$B\rho = \frac{Au}{Qe}\gamma\beta c \tag{B.1}$$

en esta ecuación u es la unidad de masa atómica, e es la carga elementale, c

es la velocidad de la luz. Midiendo la rigidez magética y la velocidad de cada fragmento es posible determinar la relación A/Z. Además se puede hacer una identificación sin ambigüedad usando detectores de perdida de energía (MUSIC).

La resolución intrinseca del FRS puede verse afectada por varios factores dentro de los que se resaltan el la emitancia del haz y el straggling en energía y en posición. Esto hace que las distribuciones de momento se vean afectadas. Por esta razón es necesario reducir el efecto del straggling optimizando la anchura de los blancos. En este punto la elección del blanco es un compromiso entre la producción Además la optica de este experimento fue optimizada con la máxima dispersión con el fin de identficar las contribuciones en espacio de momento en especial de el caso de intercambio de carga.

Los observables físicos obtenidos en este trabajo son principalmente la sección eficaz y las distribuciones de momento obtenidas del análisis de la rigidez magnética. En el caso de las reacciones de intercambio de carga el anáilis de las distribuciones de momento es una poderosa herramienta pra entender los canales que originan esta reacción a diferentes regímenes energéticos.

Reacciones de intercambio de carga isobáricas y de knock out

La base para poder trabajar las reacciones de intercambio de carga y de knock out es la identificación de cada fragmento. Una vez la masa y la carga de cada fragmento es conocida se puede determinar las distribuciones de momento o energía de cada fragmento.

Reacciones de intercambio de carga

En el caso de las reacciones de intercambio de carga el alto poder de resolución nos permite separar dos claras componentes en las distribuciones de energía. Estas comtribuciones pertenecen al canal cuasi-elástico e inélastico. Este análisis e complementado con la aplicación de una técnica de deconvolución usando como función respuesta la distribución de energía del haz, ya que este posee, en primera aproximación, todos los efectos de straggling y de emitacia que pueden afectar la distriución de energía.

La figura B.2 muestra la comparación entre los espectros experimentales y su respectiva deconvoluctión en la reacción del ^{112}Sn con diferentes blancos a una energía de 1GeV. Es importante resaltar la presencia de los dos canales: cuasi-elástico e inalástico. El canal cuasi-elástico coresponde a excitaciones

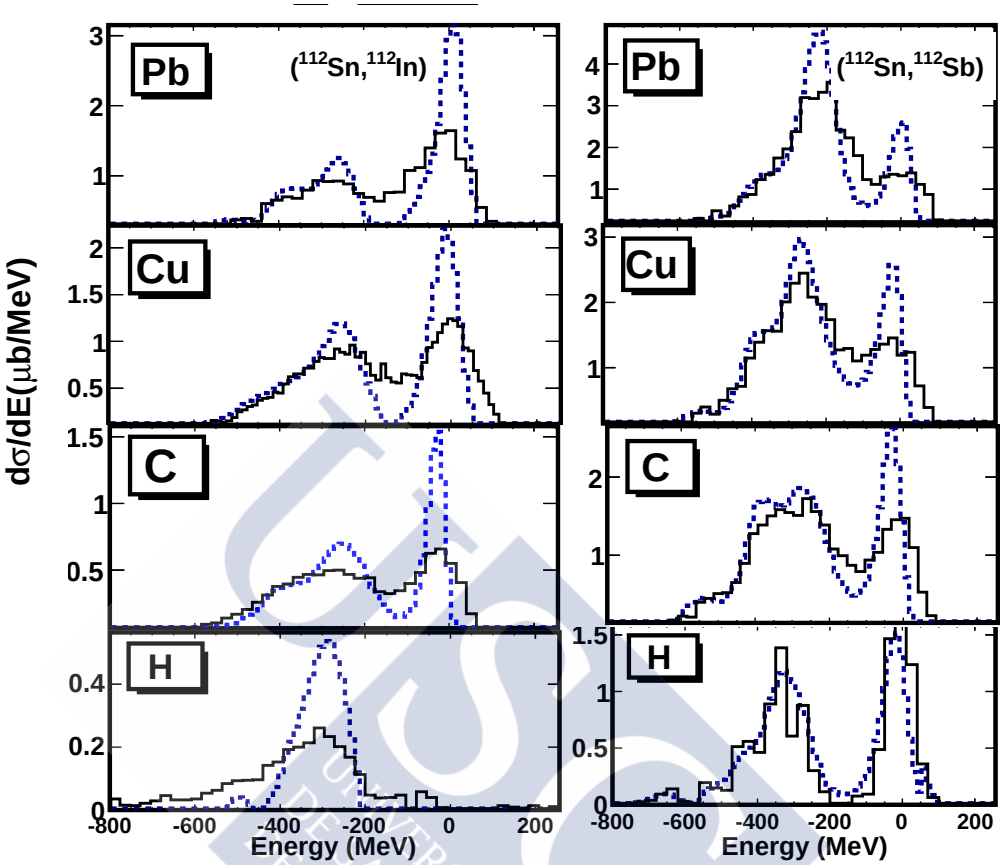

Figure B.2: *Distribuciones de energía para la reacción de intercambio de carga en el sistema de referencia del proyectil en la reacción del* ^{112}Sn *con diferentes blancos. Los dos canales (np y pn) son comparados con su respectiva deconvolución (linea a puntos).*

colectivas y aparecen en el espectro de perdida en el sistema de referencia del proyectil un pico centrado cerca del valor 0. El otro pico corresponde al canal inelástico correspondiente a las excitaciones del nucleon tales como la resonancia Δ y Roper. El correspondiente pión real creado en este caso debe escapar del nucleo para preservar el caracter isobárico de la reacción. Este hecho refuerza que esta reacción es extremadamente periférica. En el caso de la producción de ^{112}In en el proton no se evidencia la presencia del pico cuasi-elástico por conservación de la carga del proceso. Cuando las medidas de los dos canales se comparan con respeto a la posición del pico inelástico se evidencia un claro corrimiento de la energía hacia el canal elástico. Este efecto es asociado a efectos del medio, pero otras posibles explicaciones a este fenómeno esten en la misma producción relativa de las resonancias el el

blanco o en el proyectil.

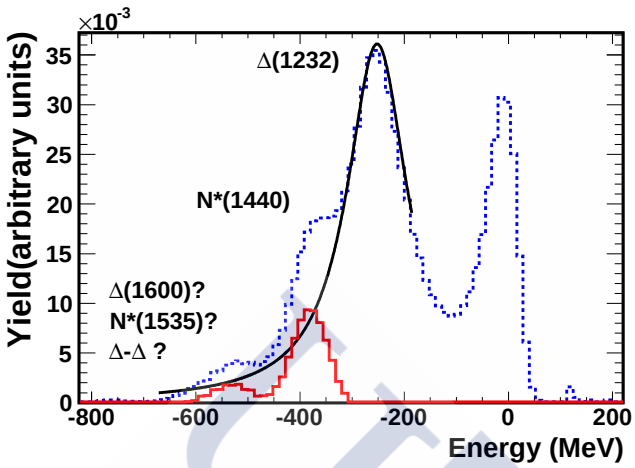

Figure B.3: *Espectro deconvolucionado del ^{112}Sb producido en la reacción $^{112}Sn(Cu,X)^{112}Sb$. En la región del canal cuasielástico se observan resonancias como la Δ y la Resonancia Roper $N^*(1440)$. El tercer pico observado no puede ser identificado con las técnicas experimentales empleadas en este trabajo.*

El análisis detallado de los espectro y si deconvolución muestran contribuciones en el canal inelástico diferentes al al resonancia Δ. La excitación de la resonancia Δ fue muy bien estudiada en núcleos a energías relativistas hacia la década de los 80, sin embargo con la resolución combinada con la deconvolución en este trabajo es posible identificar la resonancia Roper $N*(1440)$ como lo muestra la figura B.3

Se puede comprobar la dependencia de las reacciones de intercambio de carga con la energía. La figura B.4 muestra la cuando se disminuye la energía la producción relativa de resonancias en el canal inelástico disminuye dramáticamente. Este resultado comprueba como es de esperarse la dependencia de la producción de resonancias con la energía.

Otro importante observable medido en este experimento es la sección eficaz de cada reacción.En la figura B.5 se muestra la sección eficaz del intercambio de carga con respecto al número másico de cada blanco (A). Se observa la clara dependencia ya que a medida que se aumenta la la masa del blanco la sección eficaz lo hace también. Esta dependecia es aproximadamente igual al comportamiento proporcional a $A^{1/3}$, que daría cuenta de una reacción periférica pero cabe notar que esta aproxiamción no describe bien toda la linea de tendencia, por lo que hace intuir que los efectos intrinsecos de la reacción estan presentes en estos resultados . Además es clara la difer-

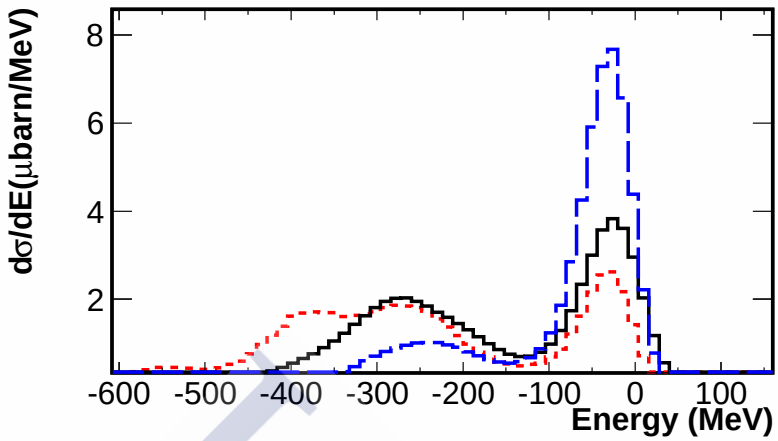

Figure B.4: *Dependencia con la energía de el canal inelástico en la reacción* $^{112}Sn(C,X)^{112}Sb$. *La linea a trazos corresponde al los resultados a* $400MeV$, *la linea solida* $700MeV$ *y la linea a puntos es la reacción a 1 GeV.*

encia en sección eficaz entre los canales np (^{112}Sb) con respecto al canal pn (^{112}In). Además existe una diferencia en sección eficaz con respecto a cada proyectil como lo indica la comparación entre el canal np originados en la reacción del ^{112}Sn y ^{124}Sn.

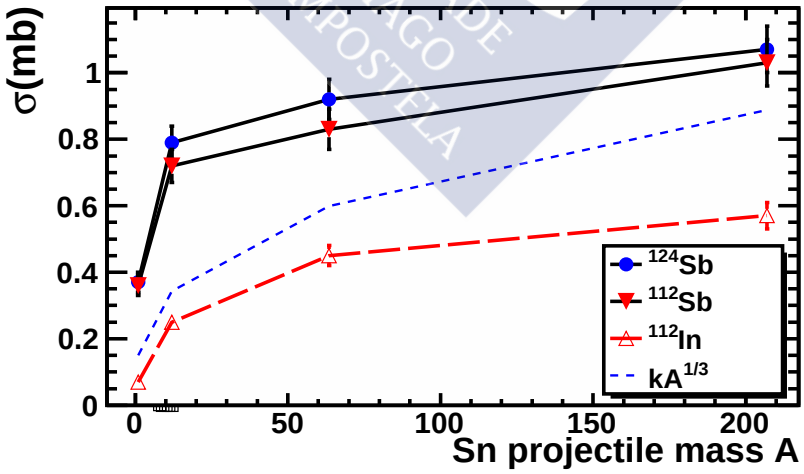

Figure B.5: *Representación de la sección eficaz total para el intercambio de carga con respecto al número másico de cada blanco (A).*

Reacciones de knock out

Otra reacción periférica analizada en este experimento es la reacción de knock out. En esta reacción el proyectil puede perder algunos nucleones. Este tipo de reacciones ha sido utilizada para investigar la estructura nuclear. El principal observable que medimos en esta ocación fue la sección eficaz. El estudio sistemático que da la interacción de diferentes proyectiles de estaño nos da un completo panorama de las secciones eficacez complementando la información sobre estos proyectiles. Como principal medida es al arranque de u proton o un neutron

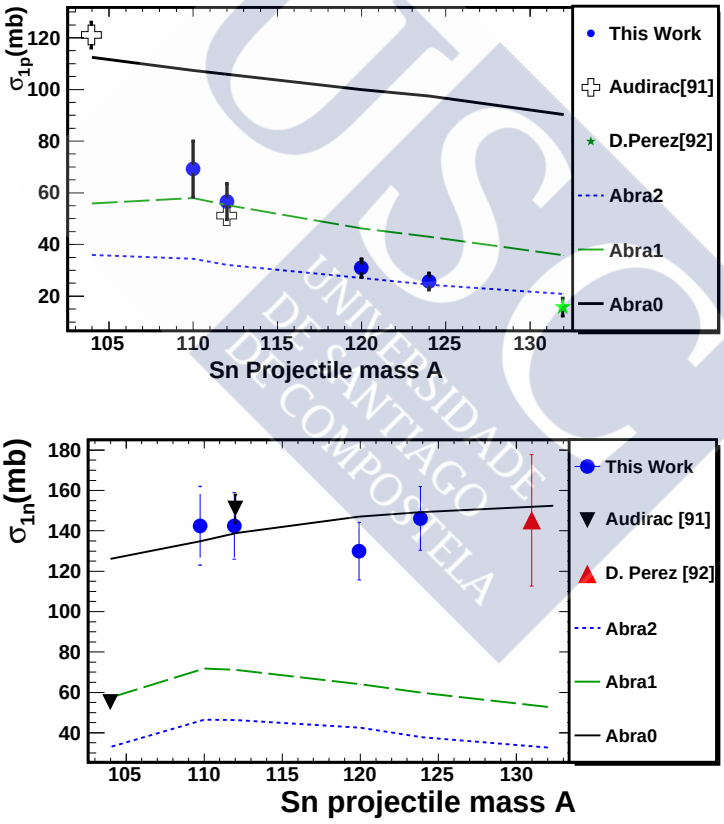

Figure B.6: *Secciones eficacez de el canal de arrancar un protón (σ_p) y un neutrón (σ_n) en función de la masa del proyectil. La figura de arriba muestra el canal de remover un protón junto con datos de optenidos por Audriac y D.perez . La figura de abajo muestra la sección eficaz de arrancar un neutrón. Ambos procesos son comparados con resultados de calculos realizados con el código ABRABLA*

En la figura B.6 se compara las secciones eficacez de arranque de un proton y un neutron y su comparasión con su respectivos cálculos. Los códigos fueron utilizados variando su respectiva energía de excitación. En el caso de Abra0 es el modelo geométrico cuyos resultados son equivalentes al modelo de Glauber, Abra1 incluye la energía de excitación obtenidad en la aproximación de un niveles energeticos de una sola partícula y Abra2 incluye el doble del valor en energía de excitación tomado en Abra1. Es claro que el modelo Abra0 reproduce bien los datos en la sección eficaz de arrancar un neutron mientras para el caso del arranque de un proton este comportamiento es contrario.

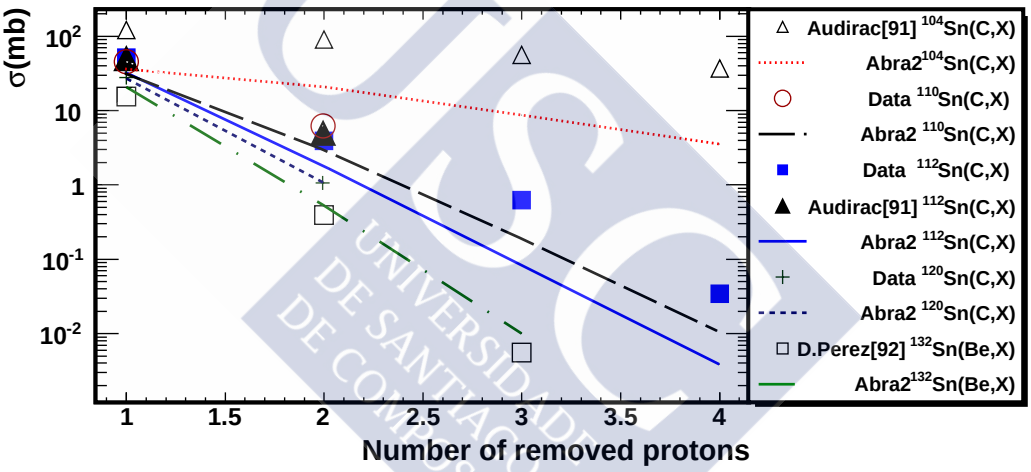

Figure B.7: *Cross sections of the proton removal channels produced by the fragmentation of Sn beams into carbon target. The experimental data are compared with the calculations of the Abrabla code with* $2x$ *modification in the energy excitation.*

Por otra parte tanbién fue posible medir el arranque de mas nucleones. La figura B.7 muestra las secciones eficaces medidas y comparadas con el cálculo del modelo de abrasión.

Es importante notar que Abra2 , el modelo con el doble de energía de escitación reproduce muy bien los datos en núcleos ricos en neutrones como el ^{132}Sn y el^{120}Sn, sin embargo esta tendencia no se mantiene para los otros nucleos más ligeros.

Conclusiones y perspectivas

Los resultados presentados son una muestra de la información que se puede sacar de una reacción periférica. En el caso de las reacciones de intercambio de carga son extremadamente periféricas ya que el caracter isobárico de la reacción se conserva. Si esta reacción no ocurriera en la periferia el pion producido en la reacción se reabsorbería cambiando el producto de la reacción. En este orden de ideas el caracter periférico de esta reacción sirve como una herramienta para distinguir el contenido de protones y neutrones en la periferia nuclear. Como se muestra en la figura B.5, al menos de forma cuantitativa es posible observar la clara dieferencia entre la producción de ^{112}In y ^{112}Sb. Esto sin duda se debe al contenido de nucleones En la misma gráfica la diferencia observada entre los proyectiles de ^{112}Sn y ^{124}Sn es atribuido a la diferencia estavez de neutrones entre uno y otro. La presencia de resonacias en el pico inelástico eran esperadas y son entendidas como excitaciones barionicas. Este trabajo develó la excitencia también de la excitación de la resonacia roper, que complementa la visión e interpretación de medidas hechas anteriormente. Las distribuciones de energía de las resonancias son medidas inclusivas es decir son la suma de muchas contribuciones elementales, de esta manera es imposible a partir de los resultados que tenemos caracterizar individualmente cada multiplete de resonancias producidas en el proyectil y en el blanco. Este hecho deja la oportunidad para en un futuro crear nuevos experimentos donde se mida el pion emitido con el fin de desentrañar la información de cada resonancia. El completo entendimiento de las reacciones de intercambio de carga estará completo cuando se pueda encontrar la ditribución espacial de los neutrones y protones en la periferia, esto será un gran dato de entrada para calcular radios nucleares con una técnica alternativa y esta información podría ser utilizada en trabajos como la ecuación de estado nuclear

Por otra parte las reacciones de knock out y su comparación con los códigos nos dan una idea de los procesos descritos en esta reacción. Es posible comprobar el poder predictivo de los modelos y reevaluar variables físicas como la energía de excitación empleada en estos modelos.